

INFORMATION TO USERS

The most advanced technology has been used to photograph and reproduce this manuscript from the microfilm master. UMI films the original text directly from the copy submitted. Thus, some dissertation copies are in typewriter face, while others may be from a computer printer.

In the unlikely event that the author did not send UMI a complete manuscript and there are missing pages, these will be noted. Also, if unauthorized copyrighted material had to be removed, a note will indicate the deletion.

Oversize materials (e.g., maps, drawings, charts) are reproduced by sectioning the original, beginning at the upper left-hand corner and continuing from left to right in equal sections with small overlaps. Each oversize page is available as one exposure on a standard 35 mm slide or as a 17" x 23" black and white photographic print for an additional charge.

Photographs included in the original manuscript have been reproduced xerographically in this copy. 35 mm slides or 6" x 9" black and white photographic prints are available for any photographs or illustrations appearing in this copy for an additional charge. Contact UMI directly to order.



300 North Zeeb Road, Ann Arbor, MI 48106-1346 USA

Order Number 8828708

**Laser welding of 200-series stainless steels: Solidification
behavior and microstructure characteristics**

Abdulgader, Saleh A., Ph.D.

The Pennsylvania State University, 1988

U·M·I
300 N. Zeeb Rd.
Ann Arbor, MI 48106

PLEASE NOTE:

In all cases this material has been filmed in the best possible way from the available copy. Problems encountered with this document have been identified here with a check mark .

1. Glossy photographs or pages _____
2. Colored illustrations, paper or print _____
3. Photographs with dark background
4. Illustrations are poor copy
5. Pages with black marks, not original copy _____
6. Print shows through as there is text on both sides of page _____
7. Indistinct, broken or small print on several pages
8. Print exceeds margin requirements _____
9. Tightly bound copy with print lost in spine _____
10. Computer printout pages with indistinct print _____
11. Page(s) _____ lacking when material received, and not available from school or author.
12. Page(s) _____ seem to be missing in numbering only as text follows.
13. Two pages numbered _____. Text follows.
14. Curling and wrinkled pages _____
15. Dissertation contains pages with print at a slant, filmed as received _____
16. Other _____

U·M·I

The Pennsylvania State University
The Graduate School
Department of Materials Science and Engineering

**LASER WELDING OF 200-SERIES STAINLESS STEELS:
SOLIDIFICATION BEHAVIOR AND MICROSTRUCTURE CHARACTERISTICS**

A Thesis in
Metallurgy

by
Saleh A. Abdulgader

Submitted in Partial Fulfillment
of the Requirements
for the Degree of

Doctor of Philosophy

August 1988

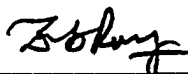
We approve the thesis of Saleh A. Abdulgader.

Date of Signature



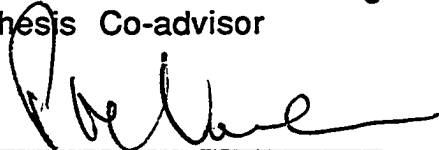
Peter A. Thrower
Professor of Materials Science
Chair of Committee
Thesis Co-advisor

June 30 '88



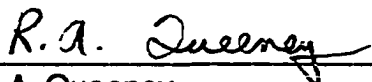
Tarasankar DebRoy
Associate Professor of
Metals Science and Engineering
Thesis Co-advisor

June 8, '88



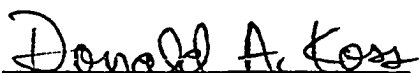
Paul R. Howell
Associate Professor of
Metals Science and Engineering

June 21, 1988



R. A. Queeney
Professor of Engineering Mechanics

June 27, 1988



Donald A. Koss
Professor of Metals Science
and Engineering
In Charge of Graduate Programs in
Metals Science and Engineering

June 24, 1988

ABSTRACT

The welding of metals and alloys with a CO₂ laser differs from the arc welding process in that the solidification and cooling of the melt occurs very rapidly. As a result, the final product microstructure of the laser weld metal will vary from that produced by arc welding processes, and from the slow cooled melt produced by other processes such as casting. Also, the rapidly cooled microstructure produced by the laser welding process can not be predicted by the consistent diagrams as is true in the case of the equilibrium structure produced during slow cooling. Since the welding of some metals and alloys by the CO₂ laser is relatively new, more studies are needed to understand the effect of rapid cooling rates on the microstructural features, morphologies and solidification behavior.

The role of the cooling and solidification rates on the final product microstructure has been investigated through this research. Slow cooling experiments using melting and casting techniques, and rapid cooling experiments using the laser welding process have been conducted on type 201 and type 202 stainless steels and the resultant structure were investigated and related to the cooling rate. An empirical equation relating cooling rate to the secondary dendrite arm spacing was determined and the 201 and 202 stainless

steel laser weld metal cooling rate has been estimated. In the slow cooling experiments, the melt solidified as primary ferrite and the delta-ferrite morphology varied, depending on the cooling rate, from a lacy structure to a skeletal structure. The laser weld metal structure solidified as primary austenite and the structure consists of austenite dendrite columns surrounded by delta-ferrite rims. The change in the solidification mode from primary ferrite to primary austenite was related to the excessive undercooling caused by rapid cooling during laser welding. Moreover, the amounts of austenite and ferrite in the laser weld metal, the primary and secondary dendrite arm spacings, the chemical composition, the size of the heat affected zone, and the depth and width of weld metal, were all related to the solidification rate during laser welding.

TABLE OF CONTENTS

	<u>Page</u>
LIST OF TABLES	xiii
LIST OF FIGURES	x
NOMENCLATURE	xv
ACKNOWLEDGEMENTS	xvii
 <u>Chapter</u>	
1. INTRODUCTION	1
1.1 General Introduction.....	1
1.2 Statement of Objectives.....	4
1.3 Layout of the Thesis.....	6
2 LITERATURE REVIEW	7
2.1 Solidification Processes During Welding.....	7
2.1.1 Solid-Liquid Interface Kinetic Effects on Microstructure.....	7
2.1.2 Microstructure Evolution Under Slow Cooling.....	9
2.1.3 Microstructure Evolution Under Rapid Cooling.....	18
2.1.4 Microstructural Development as a Function of Solidification Rate and Temperature Gradient.....	24
2.2 Solidification Behavior and Microstructural Characteristics of Austenitic Stainless Steel Welds.....	27
2.2.1 Microstructure and Solidification Behavior of the Slow Cooled Weld Metal.....	27
2.2.2 Microstructure and Solidification Behavior of the Rapidly Cooled Weld Metal.....	38
2.2.3 Effect of Ferrite in Austenitic Stainless Steel Welds.....	41
2.2.4 Proposed Mechanisms of Austenitic Stainless Steel Weld Metal.....	44

TABLE OF CONTENTS (Continued)

	<u>Page</u>
2.3 Summary.....	47
3. EXPERIMENTAL PROCEDURE.....	49
3.1 Material and Specimen Preparation.....	49
3.2 Melting and casting.....	53
3.3 Welding.....	55
3.4 Metallographic Procedures.....	57
4. RESULTS AND DISCUSSIONS.....	59
4.1 Cooling Rate, Solidification Growth Rate, and Temperature Gradient of the 200 Steel Laser Weldments.....	59
4.1.1 Cooling Rate.....	59
4.2 Effect of Solidification Growth Rate on Laser Weld Metal Characteristics.....	76
4.2.1 Geometry of the Weld Metal.....	76
4.2.2 Primary and Secondary Dendrite Arm spacings.....	81
4.2.3 Delta-Ferrite Content.....	87
4.2.4 Weld Metal Chemical Composition.....	93
4.3 Solidification Studies.....	97
4.3.1 Microstructure Morphology and Solidification Mode of Slow Cooled Steel 200 Stainless Steel.....	97
4.3.1.1 Primary Delta-Ferrite Solidification.....	97
4.3.1.2 Structure Morphology.....	102
4.3.1.3 Solid-State Transformation of Delta-Ferrite to Austenite	105
4.3.1.4 Diffusion Controlled Mechanism in the Solidification of the Slow Cooled 201 Stainless Steel.....	109
4.3.2 Microstructure and Solidification Mode of 200 Stainless Steel Laser Weld Metal.....	111

TABLE OF CONTENTS (Continued)

4.3.2.1	Fusion Zone and Heat Affected Zones Microstructures and the Mode of Solidification.....	111
4.3.2.2	Critical Cooling Rate.....	121
4.3.2.3	Proposed Mechanism For Primary Austenite Solidification During Laser Welding.....	123
5.	CONCLUSIONS.....	131
	REFERENCES.....	135

LIST OF TABLES

<u>Table</u>	<u>Page</u>
1	Chemical composition of AISI 201 and 202 high-manganese stainless steel 50
2	The cooling rates of the three 201 casts measured at the melting point and the corresponding secondary dendrite arm spacing..... 61
3	The measured secondary dendrite arm spacing (SDAS) of the 202 stainless steel laser weldments and the corresponding cooling rates determined using plot in figure 23..... 66
4	Measured values of (θ) at different welding speed (V) and the corresponding values of the solidification rate (R) of 202 steel..... 70
5	The local cooling rate of the laser weldments as determined by the product of the solidification growth rate and the computed temperature gradient..... 73
6	A comparison of the cooling rates of 202 stainless steel weldments determined by the three methods, the SDAS, the product of R and G , and the 3-D Lasncaster formula..... 75

LIST OF TABLES (Continued)

<u>Table</u>	<u>Page</u>	
7	Depth, width and thickness of heat affected zone (HAZ) of 202 steel laser weld metal as a function of solidification growth rate (R).....	82
8	Primary and secondary dendrite arm spacings of 202 steel laser weld metal as a function of solidification rate (R).....	85
9	Concentration of various elements contents (Wt. %) in the base metal (BM), ferrite (δ) and austenite (γ) phases in the 202 steel laser weld metal.....	101
10	Chromium and other elements contents of the ferrite (δ) and austenite (γ) phases in the center and edge of the 201 stainless steel cast cooled at 45 ^o C/sec.....	106
11	Diffusion rates and diffusion distances (μ m) of the Cr and Ni in the austenitic stainless steel.....	110
12	Degree of undercooling achieved in many alloys with various processes.....	127

LIST OF FIGURES

<u>Figure</u>	<u>page</u>
1 Solid growing at a velocity V with planar interface into a superheated liquid.....	11
2 Solid growing at a velocity V with planar interface into a supercooled liquid.....	12
3 Temperature inversion during freezing.....	13
4 Number of spikes of almost equal spacing formed during first stage of dendritic growth.....	15
5 Within the distance x the liquid lies at a temperature below its freezing point.....	16
6 The instability of the interface may results in the formation of a cellular structure	17
7 Microstructural consequences resulted from increasing in cooling rate	20
8 Eutectic phase diagram showing hypocooling, critical undercooling and hypercooling for solidification of the Alpha-phase.....	21
9 Schematic showing morphological developments as a function of solidification rate, temperature gradiet and cooling rate	25
10 Liquids and solidus surfaces of Fe-Cr-Ni alloy.....	28

LIST OF FIGURES (Continued)

<u>Figure</u>	<u>Page</u>
11 Vertical section of the ternary Fe-Cr-Ni phase diagram.....	30
12 Three types of microstructure and morphology of delta ferrite plotted on Schaeffler diagram.....	32
13 Schematic of the solidification and transformation behavior resulting in range of weld ferrite morphologies	33
14 Three-dimension composite micrographs of various ferrite morphologies in type 308 stainless steel welds.....	35
15 Typical microstructures of pulsed laser weld of stainless steel.....	39
16 Microstructure of 63 mm/sec laser weld metal showing Mn-Si precipitates in austenite phase	42
17 Effect of adding nitrogen on the solidification mode.....	46
18 Optical microstructure of a specimen cooled at 7000 C/sec.....	48
19 Base metal microstructure of 202 stainless steel.....	51
20 A drop casting furnace used in melting and casting experiment.....	54
21 Copper chill mold used in slow cooling experiments.....	56

LIST OF FIGURES (Continued)

<u>Figure</u>	<u>Page</u>
22 SEM micrographs showing secondary dendrite arm spacings for casts cooled at 1, 45, and 100 C/sec.....	62
23 Plot of secondary dendrite arm spacing of 201 and 202 stainless steel welds as a function of cooling rate	64
24 Secondary dendrite arm spacings of 202 steel laser weldments decreases as cooling rate increase.....	65
25 Solidification growth rate as a function of location along the solid-liquid interface.....	68
26 SEM micrographs of the crystal growth direction for 202 samples welded at 10 and 75 mm/sec.....	69
27 Top views of two 202 stainless steel samples welded at 1 mm/sec and 20 mm/sec.....	77
28 Effect of increasing scanning rate on the 201 weld pool width, depth and heat affected zone.....	78
29 Secondary dendrite arm spacings of 202 laser weldments decrease as solidification growth rate increases.....	83
30 Primary and secondary arm spacings of 202 laser weld metal decrease as solidification growth rate, R, increases.....	86

LIST OF FIGURES (Continued)

<u>Figure</u>	<u>Page</u>
31 Secondary dendrite arm spacings of 202 laser weldment as a function of solidification time.....	88
32 The laser weld metal delta-ferrite content of 202 laser weldment decrease as solidification growth rate increases.....	89
33 The laser weld metal delta-ferrite content of 202 laser weldments as a function of solidification growth rate	90
34 Amounts of austenite phase increase and of ferrite phase decrease as degree of undercooling increases.....	92.
35 Chemical composition of 202 laser weld metal as a function of solidification growth rate.....	94
36 Optical micrographs showing the typical slow cooled 201 stainless steel casting microstructure.....	98
37 Skeletal ferrite morphology of the 201 stainless steel cast samples cooled at 45 and 100 ^o C/sec.....	103
38 Lacy ferrite morphology at the center of the cast sample cooled at 1 ^o C/sec.....	104
39 Amount of delta-ferrite of 201 stainless steel casts as a function of cooling rate.....	108

LIST OF FIGURES (Continued)

<u>Figure</u>	<u>Page</u>
40	Typical microstructure of 202 laser weld metal..... 112
41	Columns of austenite dendrites are left on the surface unattacked as three-dimension network..... 114
42	TEM micrograph of 202 laser weldment showing delta-ferrite rims between austenite dendrites..... 115
43	Bright and dark field images taken from the ferrite rims of the 202 weldment..... 116
44	TEM micrograph showing number of dislocations and stacking faults in two austenite dendrites of the 202 weldment..... 118
45	The microstructure differences between the base metal (BM), heat affected zone (HAZ) and fusion zone (FZ) of 202 laser weld metal..... 119
46	A plot indicating a critical cooling rate at which the solidification mode of 201 and 202 stainless steel laser weld metal vary dramatically..... 122
47	The relative thermal stability of the liquid, FCC, and BCC phases..... 128

NOMENCLATURE

C_p	specific heat at constant pressure, cal/gm-K
H	specific enthalpy, cal/gm
G	temperature gradient, K/cm
G_l	temperature gradient in liquid, K/cm
G_s	temperature gradient in solid, K/cm
J_H	power density, cal/sec-cm ²
K	thermal conductivity, cal/sec-cm-K
Q	laser power, cal/sec
R	solidification growth rate, cm/sec
r	radial distance, cm
r_b	radius of the laser beam, cm
S_H	source term, cal/gm-sec
T	temperature, K
T_m	melting temperature, K
t	time, sec
u	radial velocity, cm/sec
V	welding speed, cm/sec
v	axial velocity, cm/sec
x	radial distance, cm
y	axial distance, cm
Y_d	absorption depth, cm

NOMENCLATURE (Continued)

γ	austenite
ρ	density, gm/cm ³
δ	ferrite
θ	solidification growth direction angle
ϵ	absorptivity of the laser beam by the material

ACKNOWLEDGMENTS

Praise be to allah, lord of the universe. I would like to thank the members of my dissertation committee, each of whom gave generously of his time, expertise and guidance: Dr. Tarasankar DebRoy, Dr. Peter Thrower, Dr. Paul Howell and Dr. Richard Queeney.

I am deeply grateful to the Libyan people for the financial support throughout my graduate school studies.

Special and affectionate thanks are due to my wife and my family who had faith in me and gave me tremendous support. Most of all, I thank my heavenly father and mother whom provided all of the strength and wisdom through their holy spirit, it is my prayer that this research project will bring mercy to their souls

Chapter 1

INTRODUCTION

1.1 General Introduction

Continuous wave CO₂ laser welding provides a number of advantages over the arc welding process. Among these advantages are high power density (of the order of 10⁶ watts /cm), deep penetration welds, high speed, high precision and the possibility of automation, less distortion due to the low heat input per unit length, and welds which are free of porosity.

Fusion joining with the CO₂ laser differs from the more familiar arc process in that the melting and solidification of the substrate occurs very rapidly with high cooling and solidification rates. This results from the focused high power density on a very small substrate area. The absorbed power in this area produces a melt layer in which most of the absorbed energy is concentrated, resulting in very steep temperature gradients. This in turn causes rapid cooling of the melt layer and a high solidification rate as the melt interface moves towards the surface of the material.

The rapid solidification encountered during laser welding presents a means by which the normal solidification structure can be significantly altered. The transformation of high temperature structures can be suppressed due to the high cooling rates. This leads to refinement of the microstructure, with fine dendrite phases and other microconstituents. With still higher cooling rates, however, nucleation can be depressed to temperatures well below the liquidus temperature, in which case microcrystalline structures, metastable crystalline phases and amorphous solids come into existence (1).

Recently, attention has been devoted to the rapid solidification laser processing of some metals and alloys. Austenitic stainless steels have received special attention due to the fact that the various austenitic stainless steels are important materials used widely where corrosion resistance and good mechanical properties are required. Also these types of steel are sensitive to the degree of cooling, thus, exhibiting a variation in microstructure and in the shape, content, size and distribution of the phases present.

The variation in the microstructural behavior of the weld metal depends on many factors, especially cooling rate, solidification growth rate and temperature gradient. Previous work (2-4) in the area of solidification behavior has shown that these factors affect the size and shape of the phases as well as the distribution of the solute within the weld metal. However, the majority of these studies have concentrated on the weld microstructure which was

produced at relatively low solidification and cooling rates such as in most casting and conventional welding processes. Although recently a few papers (5,6) have discussed the rapid solidification microstructure of stainless steels produced by either electron beam or CO₂ laser welding processes, the complex and varied nature of the ferrite morphologies has resulted in much confusion both in their description and in the understanding of their solidification behavior. Most of these studies have neglected the effect of solidification growth rate and temperature gradient. These two factors are very important in determining the microstructural behavior of the welds. The study of the influence of solidification rate and temperature gradient on microstructure will be very helpful in understanding and predicting the final weld metal microstructure.

Besides these two factors, solidification rate and temperature gradient, the initial solidification product of the weld also depends on another important factor which is the nominal composition of the melt at the liquidus temperature. However, segregation of alloying elements during non-equilibrium solidification changes the composition of the remaining liquid and alters the final solidification product. Several investigators (7,8,9) have demonstrated that the solute redistribution accompanying welding is a major factor controlling the solidification mode. Therefore, it will be necessary to undertake a solute analysis through the weld metal zones. This will be helpful to understand the laser weld metal solidification mode.

The majority of the previous studies on austenitic stainless steels have been on high nickel stainless steels (such as the 300-series), and none on high manganese stainless steels (such as the 200-series), even though the latter are very important materials for many applications where corrosion resistance and high strength properties are required.

Recently, a number of studies (10-13) has been conducted on 200-series stainless steels in order to study the alloying element vaporization, fluid flow, effect of minor amounts of surface active impurities, and plasma and welding parameters on the laser weld metal shape and size. The information from these studies is very important and conducive to the understanding of the weldability of these types of stainless steel by laser processing. The study of solidification behavior and characterization of 200-series steel laser weld metal microstructure and rules of cooling rate, solidification rate and temperature gradient on the weld metal microstructure, are of equal interest and beneficial since the final weld metal properties are related to the resultant microstructure.

1.2 Statement of Objectives

The overall objective of this research was to develop a better understanding of the microstructural characteristics of the 200-series stainless steel laser weld metal and to propose a model for the solidification and subsequent solid-state transformations which

occur in 200-series stainless steel laser weldments. This can be achieved by understanding the roles of cooling rate and solidification growth rate, R , on the solidification behavior of the laser weld deposit, and also, by following the solidification sequences and behavior of the 200 stainless steel melt which cooled at a lower cooling rate than the laser cooling range.

More specifically, the objectives of this research were as follows:

- 1) To propose a solidification mechanism for the 200-series stainless steel laser weld metal.
- 2) To estimate the cooling rate of a 200-stainless steel laser weld pool by correlating it to the secondary dendrite arm spacing.
- 3) To determine how the variations in cooling rate and solidification growth rate can influence the following:
 - a) The solidification mode of 200 steel laser weldments. This allows a prediction of whether the weld metal will solidify as primary austenite or primary ferrite.
 - b) Shape, amount, size and distribution of ferrite and austenite phases in 200 stainless steel laser weldments.
 - c) Primary and secondary dendrite arm spacings.
 - d) Solute redistribution.

1.3 Layout of the Thesis

The thesis is divided into five chapters. In chapter 1 the effect of the rapid cooling, such that encountered during laser welding, and the other important factors, on the solidification behavior and microstructural characteristics of austenitic stainless steel are presented. The objectives of the present study are also presented in this chapter.

Chapter 2 is the literature review, which is divided into two sections. In the first section there is a discussion of the solidification processes that occur during the slow and rapid cooling of metals and alloys. The second section is a review of the literature relevant to the microstructural characteristics and solidification behavior of general types of austenitic stainless steel during arc, electron beam and laser welding.

Chapter 3 is description of the experimental procedures used in this study.

Chapter 4 contains the results and their discussion.

Finally, the conclusions of this investigation are presented in chapter 5.

Chapter 2

LITERATURE REVIEW

The first section of this chapter consists of a review of the literature on the solid-liquid interface kinetic effects on microstructure evolution under slow and rapid cooling and the development of the microstructure as a function of solidification growth rate and temperature gradient. The second section is a review of the previous work on solidification behavior, ferrite morphologies, and the solid-state transformation of austenitic stainless steel weld metal. The important factors which affect the weld metal solidification mechanisms for the austenitic stainless steel welds are also reviewed.

2.1. Solidification Processes During Welding

2.1.1 Solid-Liquid Interface Kinetic Effects on Microstructure

Depending on the equilibrium conditions at the liquid-solid interface, the resultant microstructure will be either dependent on the local equilibrium growth process or on the degree of undercooling, which is related to the cooling rate. Liquid metals can

be cooled to temperatures far below their equilibrium freezing points before solidification begins. The temperature difference between the equilibrium freezing temperature and the solidification temperature is defined as the undercooling. Increasing the cooling rate results in increased undercooling. When conditions of local equilibrium exist at the solid-liquid interface, microstructural development results from differences in the growth process.

In the case of very slow cooling there will be enough time for the rejected solute or solvent to get mixed with the remaining liquid, and transportation occurs by diffusion. Therefore, slow cooling allows the solid-liquid interface to advance slowly enough that the rejected solute or solvents are mixed uniformly with the liquid, and diffusion of solute or solvent in the solid is sufficiently rapid to keep the solid at the composition which is in equilibrium with the composition of the remaining liquid.

For non-equilibrium conditions at the solid-liquid interface, where liquid is sufficiently undercooled either by rapid cooling or by suppression of heterogeneous nucleation, the first nuclei to form grow as solid with the same composition as that of the liquid. Therefore, solidification without diffusion is possible because the decrease in free energy, which is thermodynamic driving force for solidification is available without change of composition if the undercooling is great enough. Thus the solute or solvent does not have time for movement and mixing occurs in the solid or liquid.

2.1.2 Microstructure Evolution Under Slow Cooling

Solidification during crystal growth is almost never slow enough to approach equilibrium solidification, although such solidification is possible and would result when $L^2 \ll D_S t$, where L is the length of the growing crystal, D_S is the diffusion coefficient of the solute in the solid, and t is solidification time. In addition to the assumptions given above, those of equilibrium solidification, such as occur in welding, are simply complete diffusion in the liquid state and complete diffusion in solid state. Solidification of most metals and alloys from their melts is closely approximated by the assumption of equilibrium at the interface during growth.

During solidification of pure metals, the latent heat must be dissipated before solidification can continue. It can be conducted from the liquid-solid interface into the solid or liquid. Since heat flows to alleviate a negative temperature gradient the latent heat flows towards the cooler side of the solid-liquid interface. In pure metal, solidification is controlled by the rate at which the latent heat can be conducted away from the solid-liquid interface. Consider for example solid growing at a velocity V , with a planar interface into a superheated liquid as shown in figure 1. The heat flow away from the interface through the solid must balance that from the liquid plus the latent heat generated at the interface (14), i.e.,

$$K_S G_S = K_L G_L + V L \quad ,$$

where the subscripts s and l refer to the solid and liquid alloy respectively and K_i ($i = s$ or l) is the thermal conductivity, and G_i is the temperature gradient. When a solid grows into a superheated liquid, as in figure 1, the solid-liquid interface advances uniformly and tends to be smooth and planar. The situation is, however, different for a solid growing into supercooled liquid, as shown in figure 2. If a protrusion forms on the solid in this case the negative temperature gradient in the liquid ahead of the nodule will decrease and become negative. As a result, heat is removed more efficiently from the tip of the protrusion than from the surrounding regions allowing it to grow preferentially. This leads to the formation of dendrites and cellular structures.

To demonstrate the effect of undercooling and latent heat on dendrite and cell formation, figure 3 shows that the temperature inversion during freezing can be considered. This represents a region containing a liquid-solid interface with the heat being removed through the solid. By assuming that a considerable degree of undercooling has been attained, so that the temperature of the liquid is well below the equilibrium freezing point, the latent heat that is released at the interface will raise the interface temperature above that of the liquid and the solid. The temperature will therefore drop as one moves from the interface into either the liquid or solid. The temperature decreases into the liquid because there is a natural flow of heat from the interface into the undercooled liquid, and into the solid because this is the heat flow direction. The interface

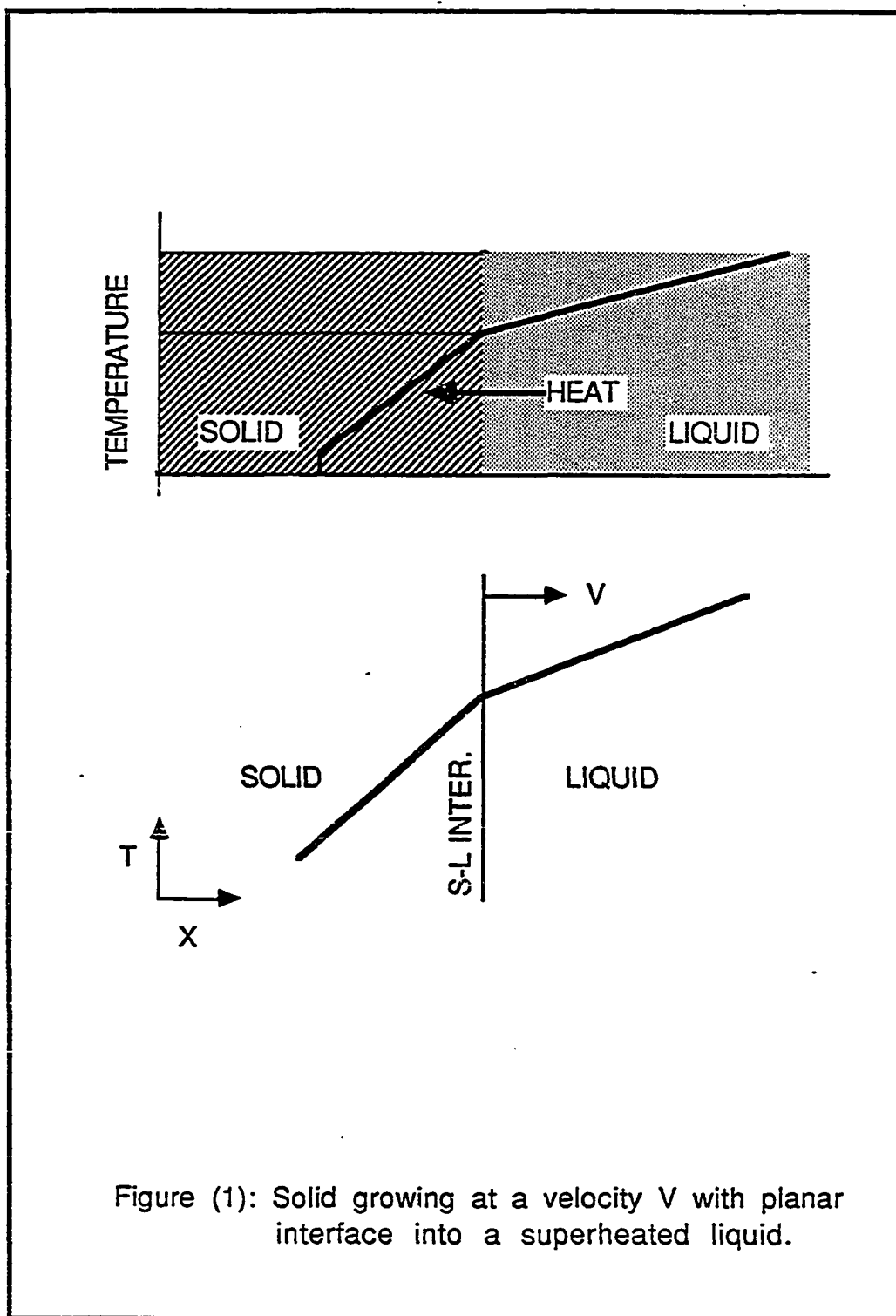
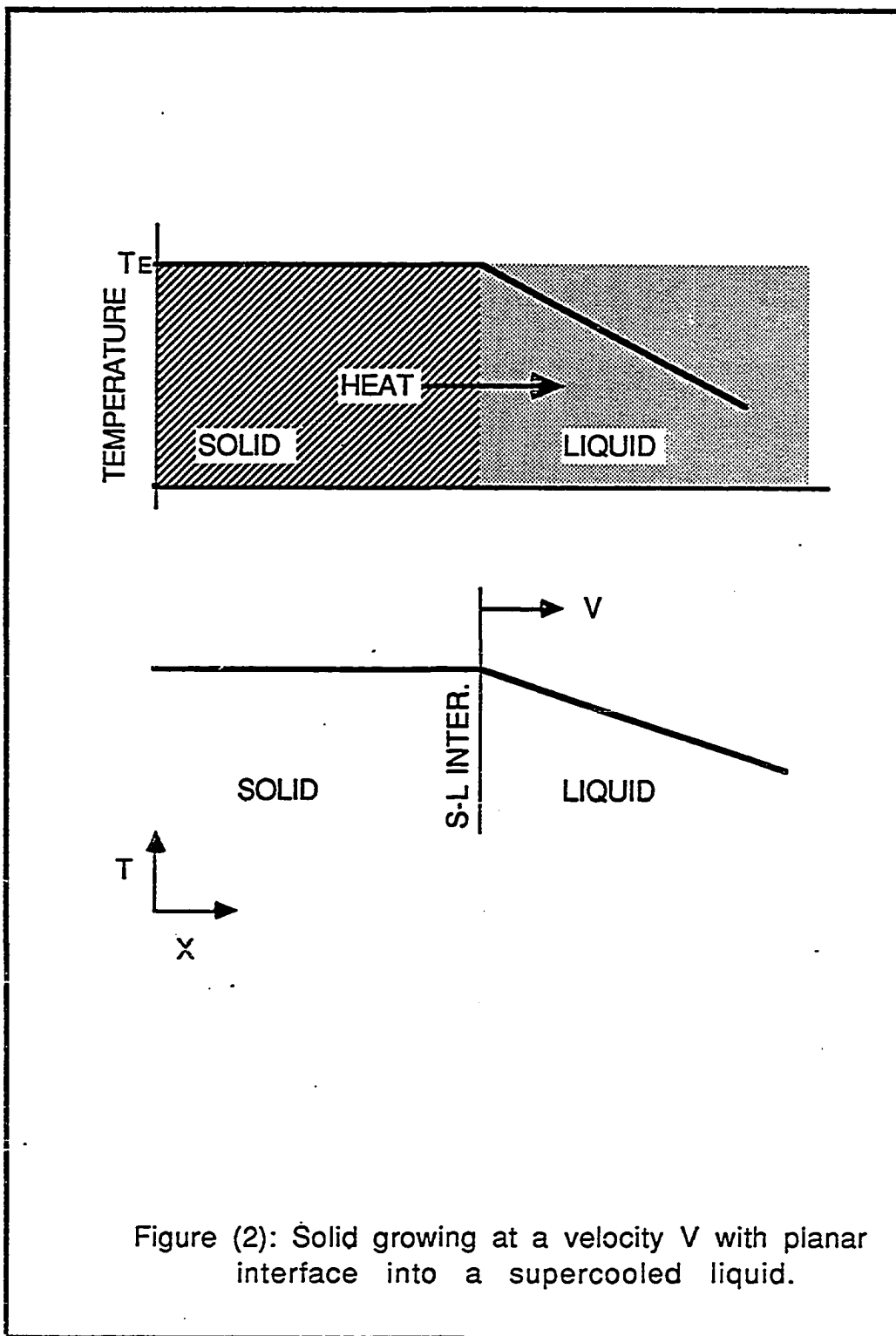


Figure (1): Solid growing at a velocity V with planar interface into a superheated liquid.



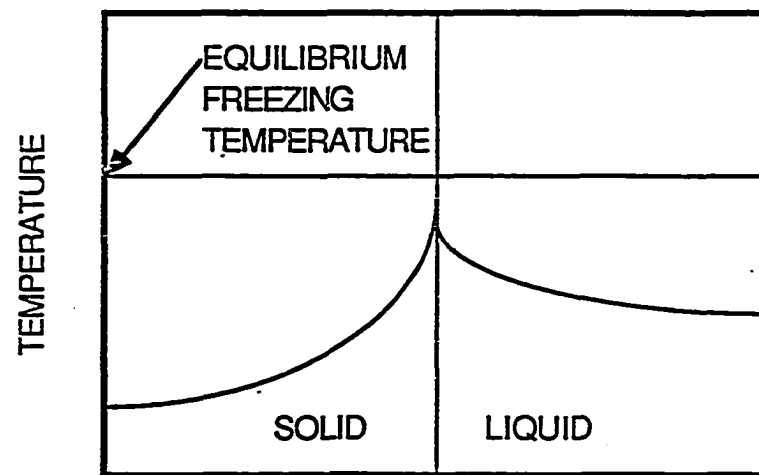


Figure (3): Temperature inversion during freezing (14)

becomes unstable as the temperature falls in the liquid in advance of the solid-liquid interface. Consequently, an initially planar interface will be unstable in the presence of a temperature inversion if perturbed and the perturbation results in anisotropic growth. Protuberances shoot out from the general interface into the liquid and become spikes whose spacing is controlled by the lateral flow of latent heat from the growing spikes, and whose rate of growth is determined by the rate at which heat is conducted away from the growing tips. These spikes are generally referred to as dendrites. The net result is that a number of dendrites of almost equal spacing is formed as shown in figure 4. Branching occurs because the liquid between the spikes is supercooled, the direction of growth is always crystallographic and is known as the dendritic growth direction. The process repeats on a finer and finer scale until there is insufficient undercooling to develop irregularities of growth into branches.

Dendritic freezing usually occurs when the undercooling layer, of thickness x in figure 5, is sufficiently large. If it is thin, the growth of true spikes is not possible because of the limited depth of the undercooling layer into which they can grow (14). In this case, the instability of the interface may result in the formation of a surface composed of more or less oval projections of the type shown in figure 6-a. Because the movement of a surface of this type is coupled with the forward motion of the narrow undercooled region, its shape is stable. In order for the surface to maintain its shape,

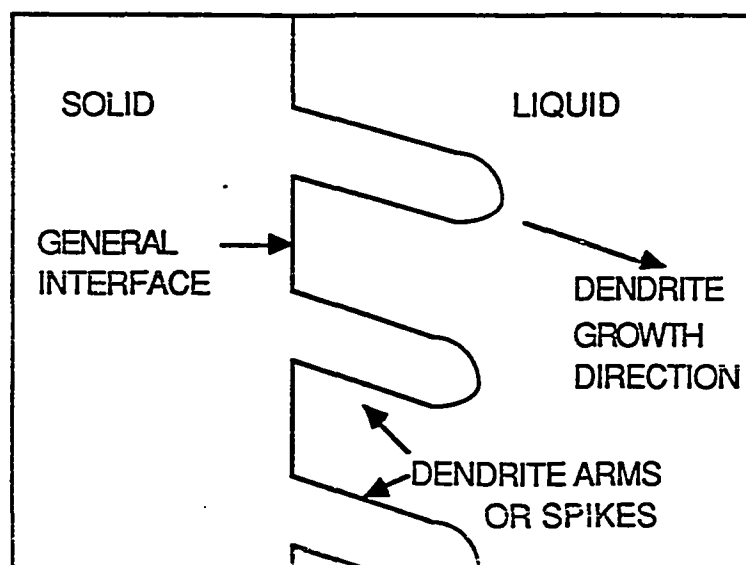


Figure (4): Number of spikes of almost equal spacing formed during first stage of dendritic growth (14).

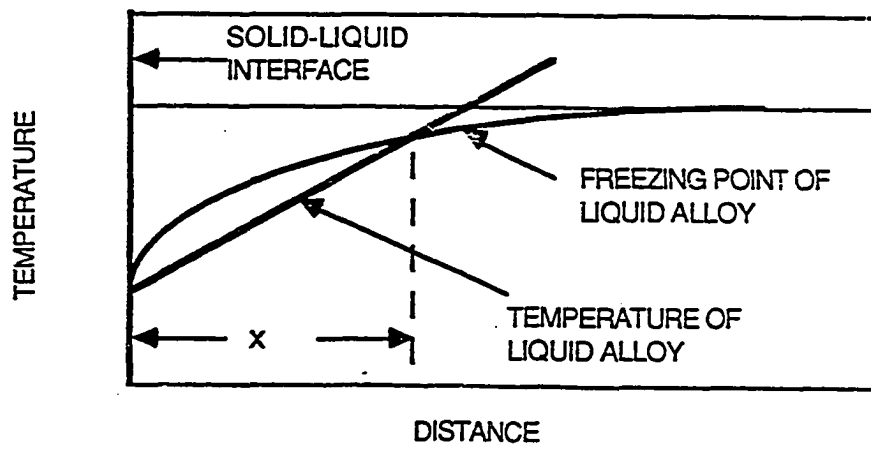
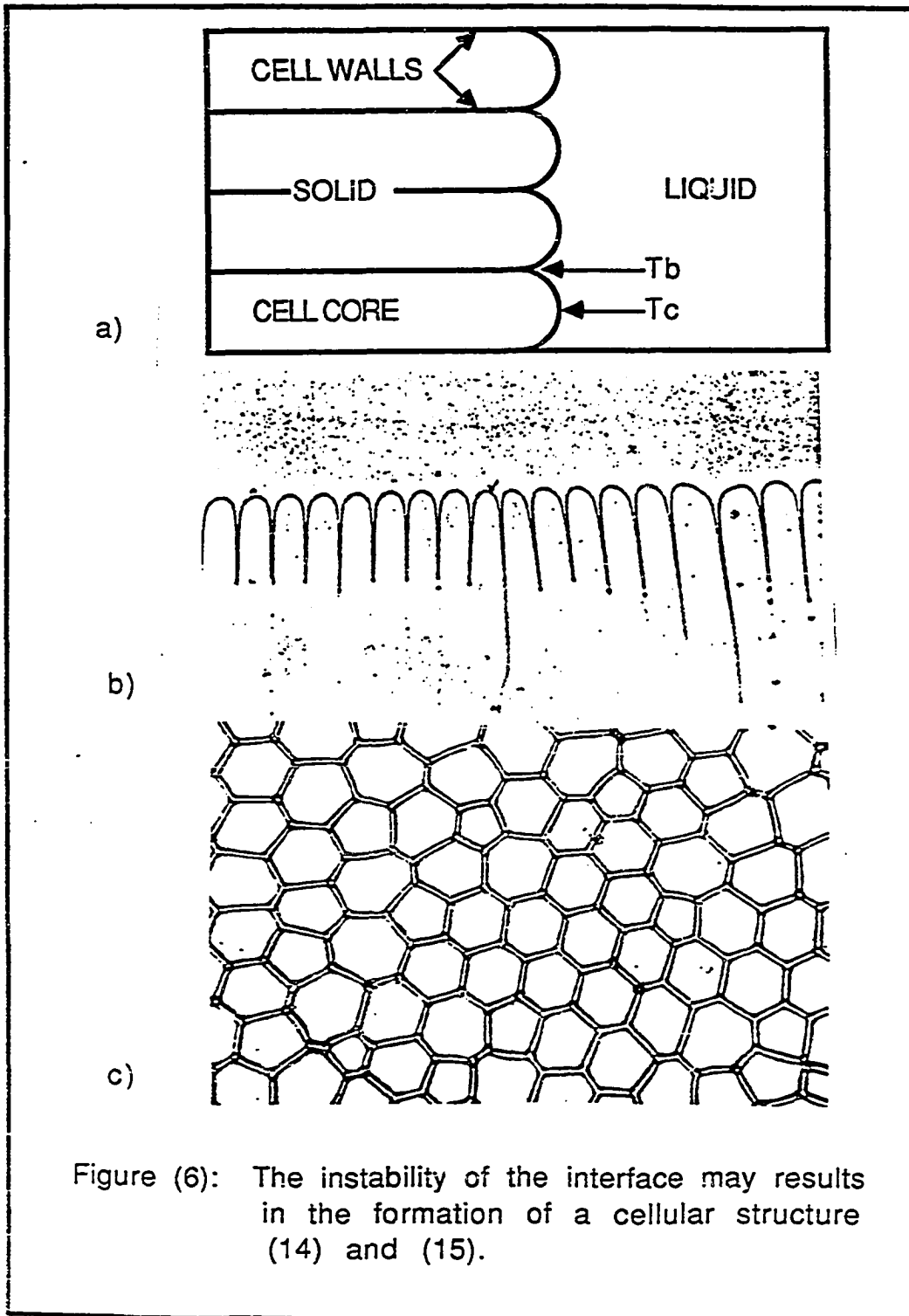


Figure (5): Within the distance x the liquid lies at a temperature below its freezing point(14).



freezing must occur uniformly over the entire area. However, the solid on the surface at the center of the projections at a temperature (T_c) higher than that of the boundaries (T_b). Coupled with this temperature difference is a difference in the composition of the liquid that freezes at the two compositions. That which solidifies at the boundaries has a higher concentration of solute than that at the center of the projections. The result of this freezing process is the formation of a cellular structure in which the cell walls are defined as regions of high-solute concentration. Figure 6-b and c show diagrams of this cellular structure (15).

2.1.3 Microstructural Evolution Under Rapid Cooling

The above discussion has been concerned with microstructural development under slow cooling. However, if undercooling of a liquid, which is related to the cooling rate, is sufficient, novel microstructures can be produced due to local non-equilibrium conditions at the solid-liquid interface. By increasing the cooling rate to greater than the conventional $100^{\circ}\text{C}/\text{sec.}$, researchers (16) have demonstrated considerable refinement in the microstructural features. At higher cooling rates, nucleation can be depressed to temperatures well below the liquidus temperature, resulting in novel microstructures such as extended solid solutions, microcrystalline phases, and amorphous structures.

At the faster quenching rates there can be large departures from local equilibrium at the advancing solid-liquid interface with resulting solid phase entrapping and supersaturated concentrations of solute and impurities. The resulting solid may have the same composition as the parent liquid (17, 18). Figure 7 illustrates the results of increasing the cooling rate on microstructure.

To understand the concept of extended solid solutions, microcrystalline phases, and amorphous structure development during rapid cooling of an alloy, a simple eutectic phase diagram like that shown in figure 8-a can be used. This model illustrates the concept of undercooling, where nucleation of the α -phase occurs at temperatures less than liquidus temperature, T_1 . In order to reduce the level of chemical segregation, the degree of undercooling should be as large as possible. The model shown in figure 8-a illustrates three undercooling conditions from the liquid state, with composition C_a , associated with temperatures T_1 , T_2 and T_3 , as shown in figure 8-b. Nucleation occurs at T_1 , T_2 and T_3 after which latent heat is evolved (recalescence). During the first stage of undercooling, usually called hypocooling, solidification starts massively at T_1 but local equilibrium and compositional partitioning occur when the interface temperature becomes greater than the solidus temperature due to recalescence. The second condition corresponds to undercooling from the liquid state to T_2 and in this instance the recalescence temperature is described as critical undercooling. Solidification in this case takes place massively

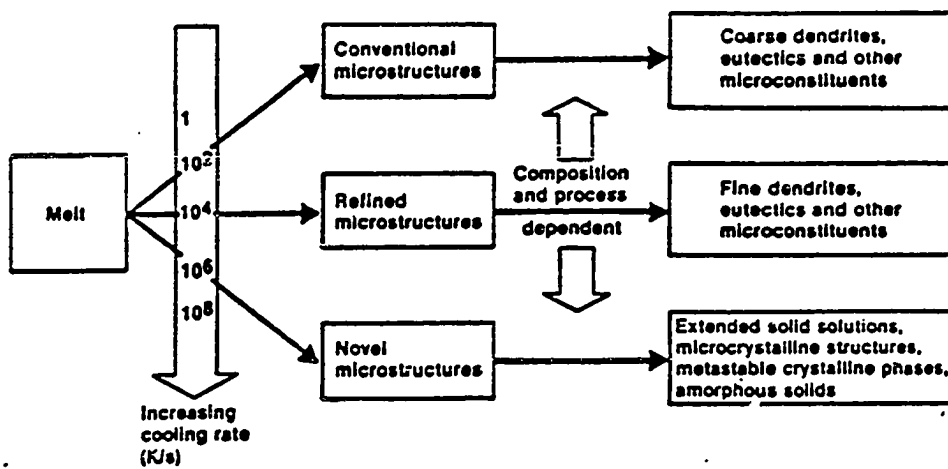
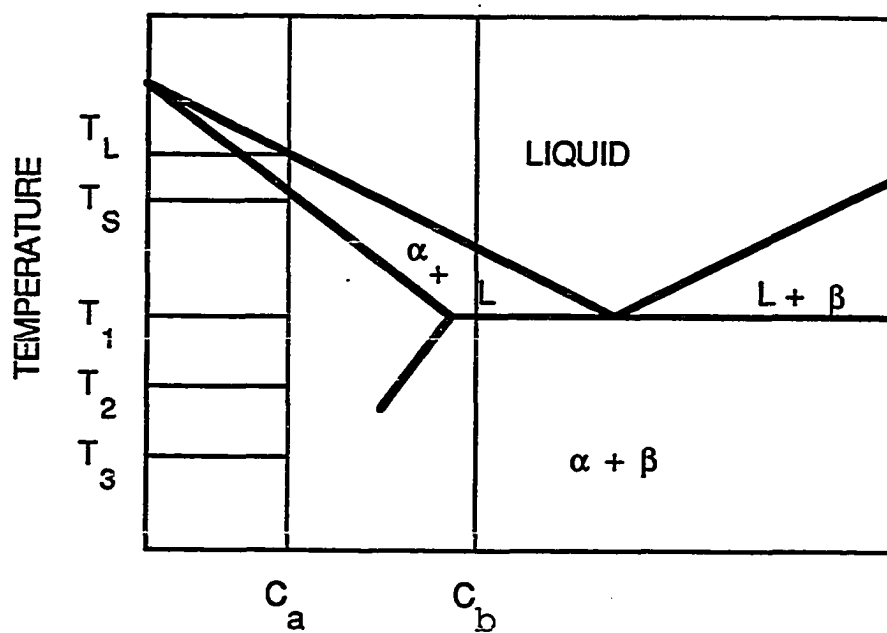
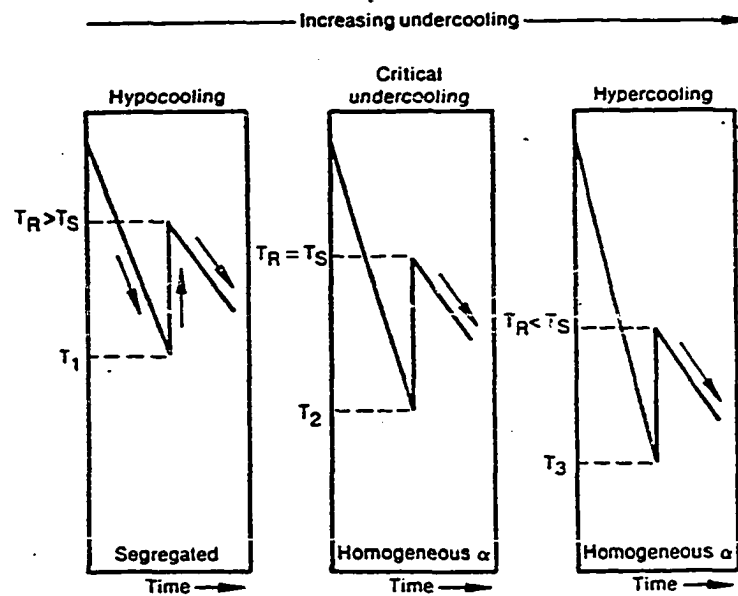


Figure (7): Microstructural consequences resulted from increasing in cooling rate (17).



a)

Figure (8): a) Schematic for representing the concept associated with undercooling of the Alpha-phase for a simple eutectic system (18).



b) Illustration of hypocooling, critical undercooling, and hypercooling for solidification of the Alpha phase (16).

Figure (8): (Continued)

without partitioning or local equilibrium at the solid-liquid interface. Because the interface temperature does not increase above the solidus temperature the result is a microcrystalline microstructure. The third condition is classified as hypercooling. During hypercooling no segregation occurs and complete solute trapping occurs. Since the nucleation rate is very fast compared to the solidification growth rate, the resultant structure is very fine. An extreme case of hypercooling is when no nucleation occurs and therefore no latent heat evolution, so an amorphous solid is formed if the undercooling goes below the glass transition temperature of the material. Recent assessment by investigators (19) using the STEM has shown some very interesting microchemical patterns in centrifugally atomized alloy powders which cooled very rapidly. The examinations were performed on high phosphorus steel and high sulfur type 303 austenitic stainless steel powders. In the cellular region for the high phosphorus steel, a second phase of high P, Ni, and Cr compositions near the cell walls was observed. Microdiffraction was used to show that the second phase is amorphous. Other investigators (20, 21) have shown amorphous particles of Mn-Si in type 316 austenitic stainless steel laser weld metal, which is unusual in austenitic stainless steel weldments.

It was noted earlier that rapid cooling or solidification can extend the amount of solute beyond normal equilibrium levels, or extend the solute solubility and produce metastable phases. This concept is shown in figure 8-a. Once again a single eutectic binary

diagram can be used for illustration. If a melt with composition C_b can be sufficiently undercooled, the liquidus and solidus boundaries can be extended such that α -phase plus liquid will co-exist at temperatures below the equilibrium eutectic temperature. This can lead to a condition where the β -phase is totally suppressed. Ge et al. (22), have reported a study on a nickel-base superalloy which contains a large concentration of refractory metals. In the conventional cast form, the superalloy contains gross cast structures and high temperature segregated phases. They observed that after laser-glazing treatments, the high melting point phases disappear, and the composition becomes more homogeneous with near elimination of chemical segregation.

2.1.4 Microstructural Development as a Function of Solidification Growth Rate and Temperature Gradient

One method of representing microstructures in cast metallic systems has been by correlation with two parameters important in instability theory--the solidification growth rate, R , and the temperature gradient, G , in the liquid phase just ahead of the advancing interface.

The effect of R and G on microstructures formed from the melt for local equilibrium conditions at the solid-liquid interface has been presented by Cohen et al. (17) as shown in figure 9. Generally, a

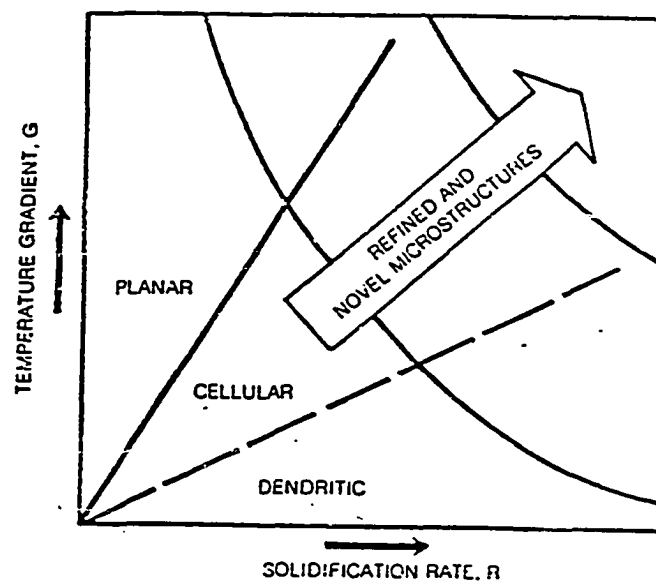


Figure (9): Schematic showing morphological developments as a function of solidification growth rate, temperature gradient and cooling rate (17).

steep temperature gradient tends to stabilize planar front growth and homogeneous microstructures. The boundary between the planar and cellular regions is the locus of G , R combinations that just balance the aforementioned two tendencies. To the left of this line, the temperature gradient effect dominates, resulting in planar front growth, whereas to the right of this line the solute gradient effect dominates, resulting in cellular growth. With still higher R , the familiar dendritic-growth morphology is encountered.

2.2 Solidification Behavior and Microstructural Characteristics of Austenitic Stainless Steel Welds

In this section a review of literature on solidification behavior, ferrite morphologies and solid-state transformation in stainless steel weld metal are given. The important factors affecting the weld metal solidification mode and morphology, the proposed solidification mechanism for the austenitic stainless steel welds, and the effect of delta-ferrite on the properties of the weld are also reviewed.

2.2.1 Microstructure and Solidification Behavior of the Slow Cooled Weld Metal

An understanding of the solidification behavior of austenitic stainless steel weldments is complicated by the occurrence of a variety of ferrite morphologies. However the Fe-Ni-Cr ternary diagram shown in figure 10-a and b can be used to discuss, in general terms, the solidification process. Compositions on the Ni-rich side of the eutectic will solidify as primary austenite. As the composition reaches the eutectic, some ferrite will form during the last stages of solidification. This will then be confined to the solidification cell boundaries. Alloys sufficiently far from the eutectic, at the Cr-rich side, however, are known to solidify as

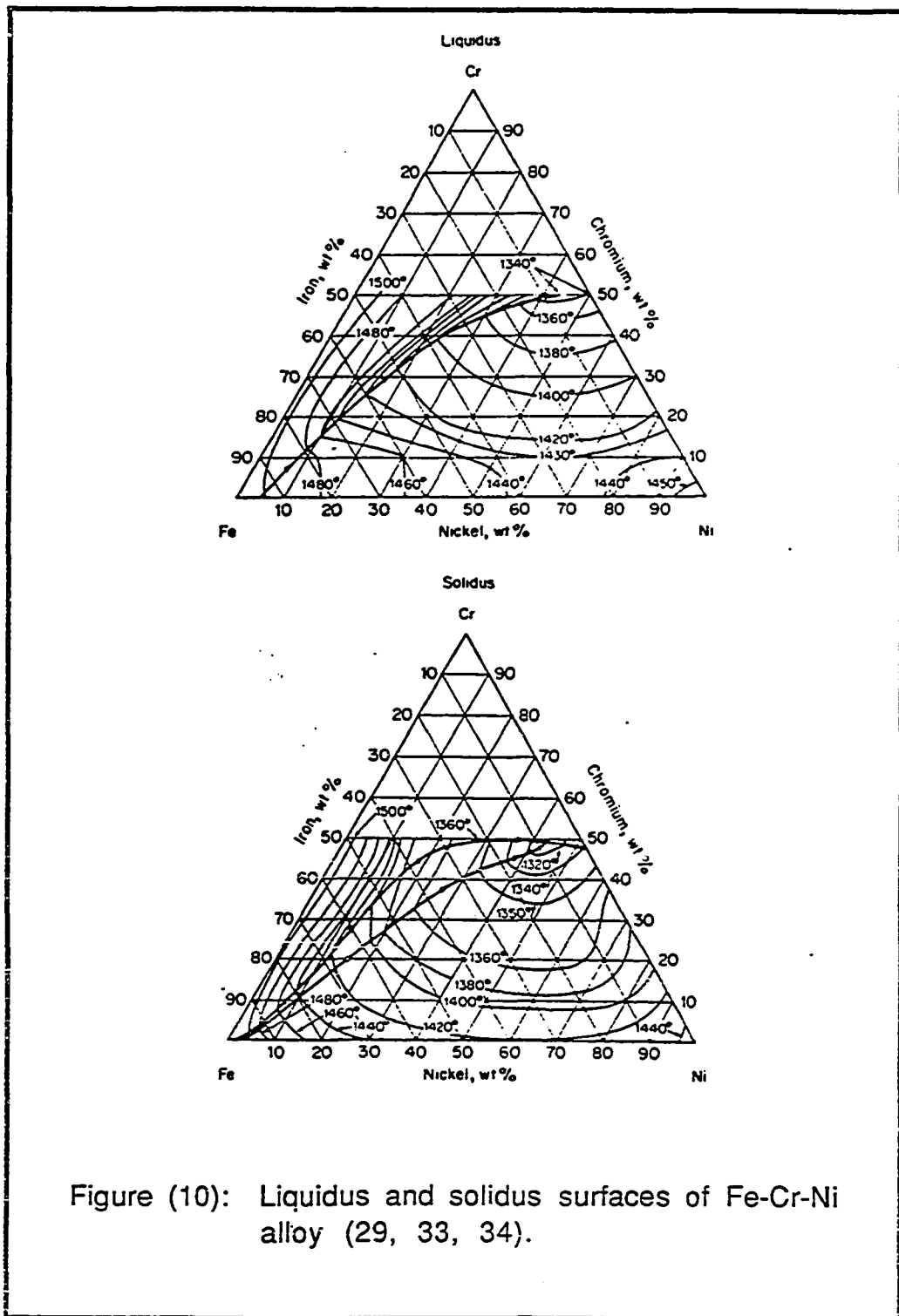


Figure (10): Liquidus and solidus surfaces of Fe-Cr-Ni alloy (29, 33, 34).

primary ferrite, but much of the ferrite will transform to austenite on cooling.

As shown by the vertical section of the ternary diagram in figure 11, compositions may have an equilibrium structure of 100% ferrite at elevated temperatures but still be partly or completely austenitic at lower temperatures. This transformation leads to various ferrite morphologies, and these may appear similar to the eutectic ferrite of primary austenite solidification structures.

Detailed studies by Fredriksson (23) on 304 stainless steel castings indicated that alloys could solidify as primary ferrite or primary austenite, and still contain a rather small amount of ferrite at room temperature. Using controlled solidification experiments, he found that a large fraction of each dendrite solidified as primary ferrite, but upon cooling through the gamma-delta two-phase region, transformed to austenite except for thin rods or strips of ferrite along the core of the original dendrite.

Studies by Arata et al. (24) on 304 stainless steel showed that as much as 70-80% of the dendrite can form as primary ferrite before the remaining liquid becomes enriched enough in Ni to solidify as austenite.

Sutala and co-workers (25) classified the stainless steel weld metal solidification modes of the AISI 300 series into three types, A, B and C. The three different solidification types are distinguished by the ratios of Cr to Ni equivalents as follows:

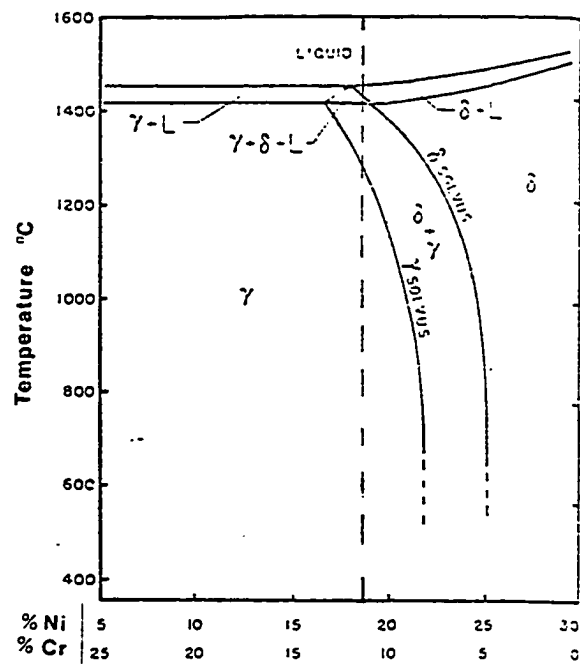


Figure (11): Vertical section of the ternary Fe-Cr-Ni phase diagram (29, 33, 34).

Type A: $C_{req} / Ni_{eq} < 1.48$

Type C: $C_{req} / Ni_{eq} > 1.95$

Type B: intermediate between A and C.

These three types are plotted on a Schaeffler diagram as shown in figure 12. Type A solidifies primarily as austenite, and the delta ferrite, if any, forms from the melt between austenite and dendrite. Type C solidifies as single phase ferrite, followed by a solid-state transformation to austenite, preferentially at ferrite grain boundaries.

A schematic by Suutala et al. (26) and others (27, 28) depicting the weld structures during solidification and subsequent cooling is shown in figure 13 for several C_{req} / Ni_{eq} ratios. Their interpretation of the resulting modes and ferrite morphologies for both primary austenite and primary ferrite is as follows. Figure-a shows solidification as 100% austenite while in figure 13-b, some eutectic ferrite has also formed during the last stages of solidification. In figure 13-c, solidification occurred as primary ferrite, but austenite also formed from the melt. On cooling, much of the ferrite transforms to austenite, leaving only ferrite along the dendrite skeleton. At higher C_{req}/Ni_{eq} , as shown in figure 13-d, the solidification proceeds in a similar way except that the ferrite morphology starts to take on a lathy appearance. At even higher C_{req}/Ni_{eq} ratios (figure 13-e), solidification occurs as 100% ferrite and larger lath packets are formed.

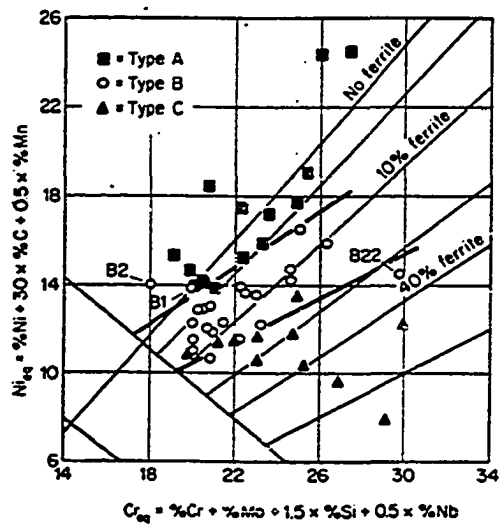
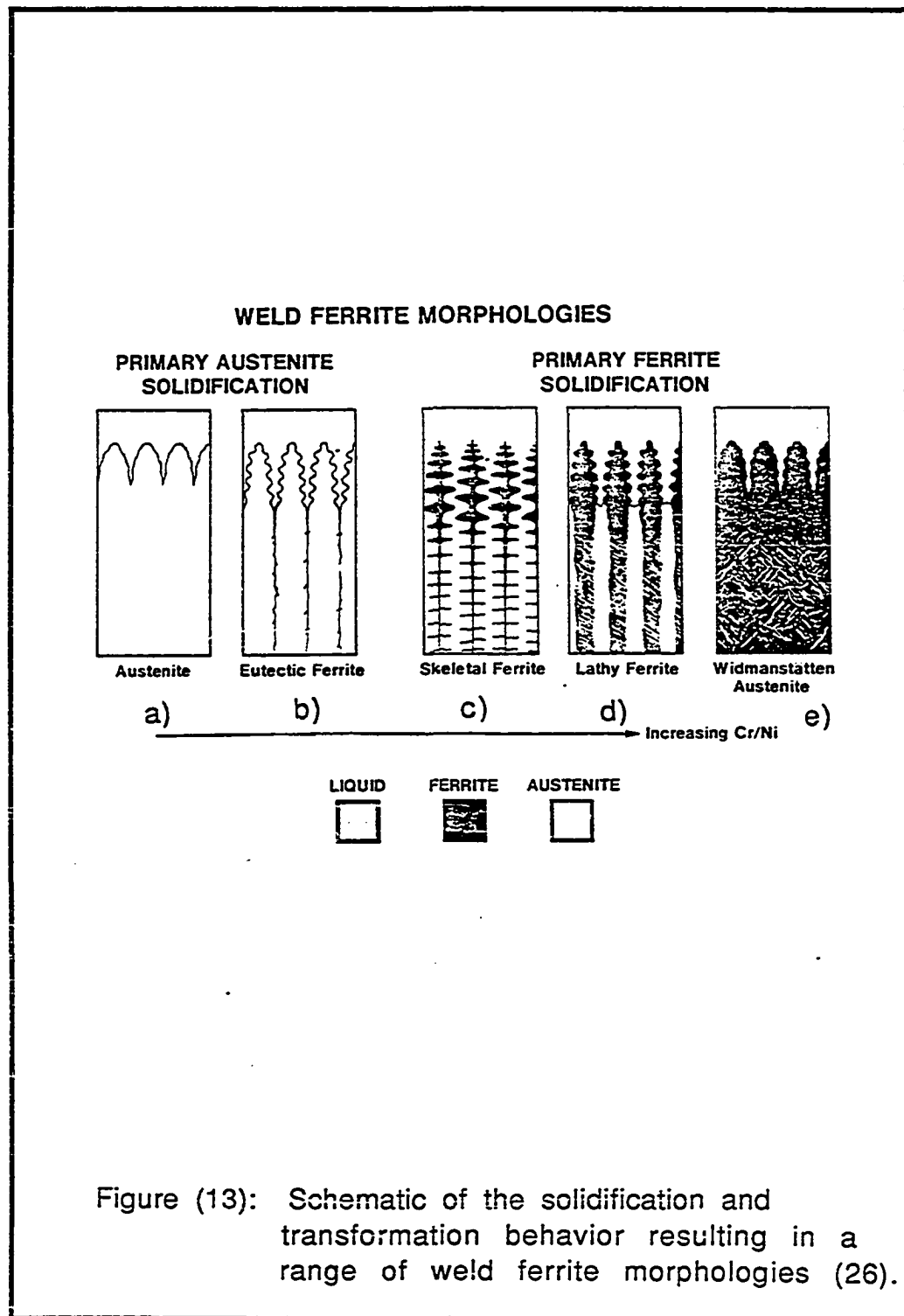
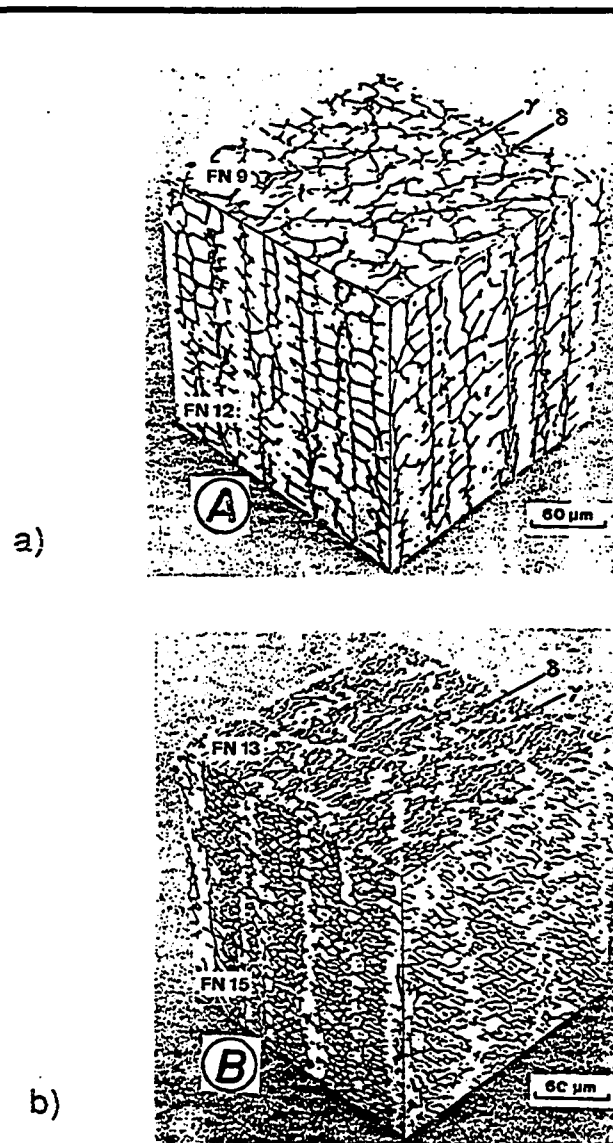


Figure (12): Three types of microstructure and morphology of delta ferrite plotted on schaeffler diagram (25, 26).



As seen in figure 13 the ferrite morphologies can be quite varied, and may lie within the dendrite core or be present as eutectic ferrite within the cell boundaries. The terminology for the different ferrite morphologies is not well established and can be rather confusing. Brooks (29) has identified a terminology of ferrite morphologies from the schematic sketches such as shown in figure 13. When the ferrite is definitely within the cell boundary, figure 13-b, it is referred to as eutectic or cellular ferrite. If it is definitely within the center of the cell (figure 13-c) it is termed skeletal, or lathy ferrite (figure 13-d). The "vermicular" term was used by Brooks to define the ferrite morphology which often appears similar to that shown in figure 13 c. The difference results from the transition from cellular to cellular dendritic solidification, and to the increase in ferrite content. For simplicity, and to reduce the confusion resulting from ferrite terminology, skeletal and vermicular will be termed "skeletal" in this thesis, and lathy as "lacy".

David et al. (30) conducted similar studies in which they used 308 stainless steel weld metal and the gas tungsten arc process to study the solidification morphologies. Four distinct types of ferrite morphologies have been identified. These four types are shown in figure (14). The first type, called a skeletal morphology, is shown in figure 14-a. In this the primary solidification occurred as ferrite. This is located within the cores of the primary and secondary dendrite arms and is the result of the incomplete primary delta to



Figure(14): Three-dimension composite micrographs of various ferrite morphologies in type 308 stainless steel welds (30).

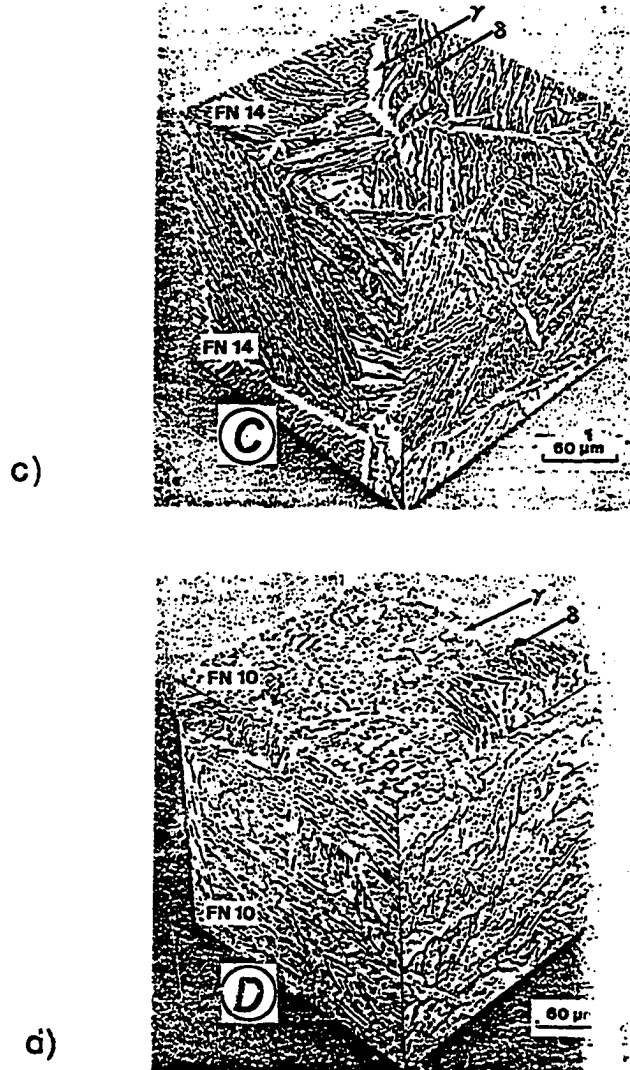


Figure (14): (Continued)

gamma transformation. The second type is the lacy morphology and is characterized by long columns of an interlaced ferrite network oriented along the growth direction in an austenite matrix. The ferrite is located within the cellular dendrites. This type is very similar in its description to the lathy ferrite morphology described by Brooks. The third type is the acicular morphology characterized by the random arrangement of needle-like ferrite distributed in an austenite matrix. Unlike the two morphologies just described, the structure here has no directionality. The fourth type is named globular and is characterized by the ferrite in the form of globules randomly distributed in a matrix of austenite. As in the globular form the structure has no directionality.

It has been suggested by Moio et al. (31) that ferrite morphologies in the welds are dependent upon the Cr_{eq} / Ni_{eq} ratios based on the Schaeffler diagram. They suggest that for ratios of $Cr_{eq} / Ni_{eq} < 1.48$, the ferrite is eutectic in nature; that at ratios of 1.48 - 1.95 the ferrite exhibits primarily the skeletal morphology; at ratios of 1.95-2.3 the ferrite exhibits mainly the lathy morphology; and that above a ratio of about 2.3 the austenite exhibits a Widmanstätten morphology, primarily along the cell boundaries within a ferrite matrix.

Lippold and Savage (33,34) have qualitatively related the ferrite morphologies to the arrangement of the phase diagram. They suggest that the same ferrite progression described above occurs, but they relate the morphology to the distance of the nominal composition

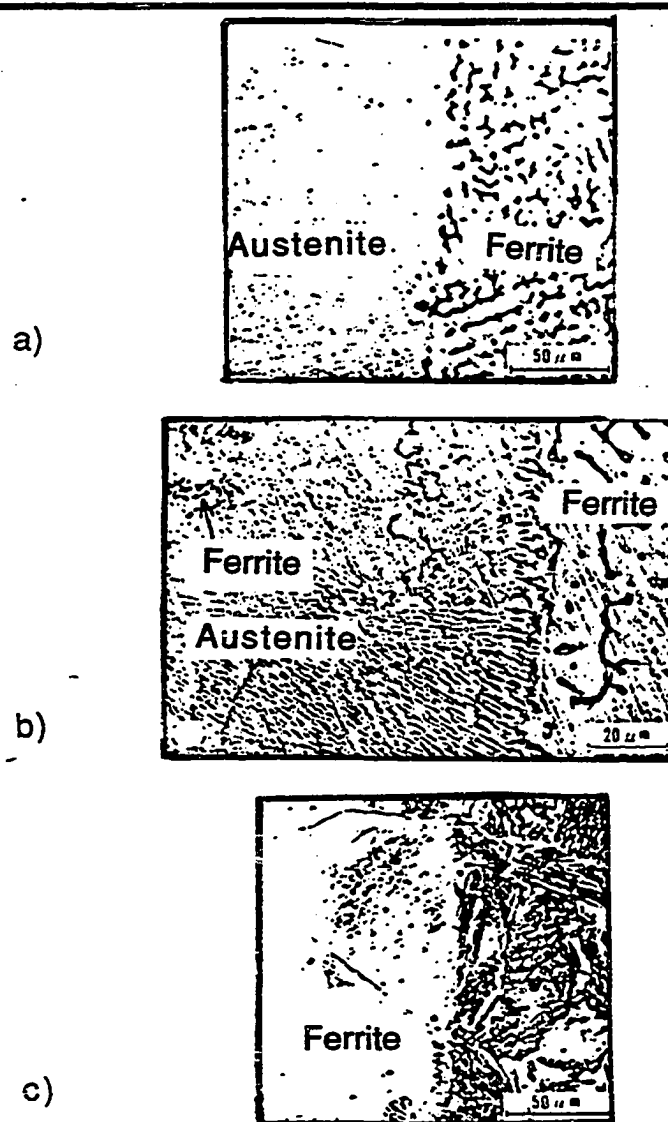
from the eutectic trough and the shape of the gamma-delta two-phase region. They suggest that lathy structures are favored at high Cr concentrations for a constant Fe level.

2.2.2 Microstructure and Solidification Behavior of the Rapidly Cooled Weld Metal

The rapid solidification of the melted material encountered during laser welding can alter the resultant microstructure of the weld metal. Consequently the weld metals produced by the laser would show a more complicated microstructure which is quite different from that of normal arc weld metal.

Several papers will be discussed later in this section, indicating that a number of factors such as the chemical composition of the steel weld metals, the rate of cooling to room temperature and subsequent solid-state ferrite-to-austenite transformation behavior could affect the morphology, amount and distribution of residual delta-ferrite.

Katayama and Matsonawa (35, 36) have related the ferrite morphologies in pulsed laser type 304 austenitic stainless steel welds to the Cr and Ni equivalents. Figure 15 shows the typical microstructure of laser weldments with different Cr and Ni equivalents. In figure 15-a, about 7% intercellular eutectic ferrite is seen in the as-cast material on the right part of the micrograph,



Figure(15): Typical microstructures of pulsed laser weld metal of stainless steels: a) Cr/Ni ratio = 1.43 , b) Cr/Ni ratio = 1.695 and c) Cr/Ni ratio = 1.962 (35, 36).

but a fully austenitic cellular structure is observed in the pulsed laser weld metal on the left. Thus, the solidification in the laser weld is considered to have occurred as an austenite single-phase in contrast to the eutectic solidification in the as-cast material. Although the base metal in figure 15 b which has a Cr_{eq}/Ni_{eq} ratio = 1.695 shows about 9% of skeletal ferrite, the pulsed laser weld metal exhibits an almost fully austenitic microstructure together with a much smaller amount of retained ferrite. In figure 15-c, with Cr_{eq}/Ni_{eq} ratio of 1.962, austenite is precipitated in a feathery Widmanstten pattern at the ferrite grain boundaries, while a fully ferritic cellular microstructure is seen in the laser weld metal.

David (37) has related the solidification mode in continuous wave CO_2 laser austenitic stainless steel welds to the cooling rate. He showed that under rapid solidification conditions with cooling rates on the order of 10^5 K per second, the structures of the type 308 and 312 steels were found to be extremely sensitive to quite small differences in the cooling rate. In the case of type 308 stainless steel, a fully austenitic structure was found in the most rapidly solidified samples, whereas a duplex structure was present in the slowly cooled laser welded samples. For the type 312 stainless steel the structure varied from fully ferritic at high cooling rates to duplex austenite plus ferrite as the cooling rate decreased.

Reduction in the weld ferrite content was observed by Vitek and David (15) in laser welds produced in type 308 stainless steel when

the laser welding speed increased from 13 mm/s to 63 mm/s. The low weld speed 308 stainless steel showed about 8% ferrite, while at a high welding speed the weld metal ferrite content was only 1%. In addition, they reported the existence of a uniform distribution of amorphous Mn-Si spherical particles in the fully austenitic welds which were produced at higher welding speed. The microstructure of the 63 mm/s laser weld showing these particles is shown in figure 16. The mode of formation of these particles was not explained.

2.2.3 Effect of Ferrite in Austenitic Stainless Steel Welds

1) On weld metal hot cracking: Investigations of fully austenitic weld metals have related a high incidence of hot cracking both in the fusion zone and in the heat affected zone. By comparison, austenitic stainless steels which produce a duplex austenite-ferrite microstructure in as-deposited welds are reported to be more resistant to both fusion zone and heat affected zone hot cracking than fully-austenitic alloys (37,38,42,43,44,45,46). A number of rationales have been proposed to explain the beneficial effect of ferrite, or primary ferrite solidification, in reducing weld cracking (42,43,44,45,46). Some of these rationales have been explained in

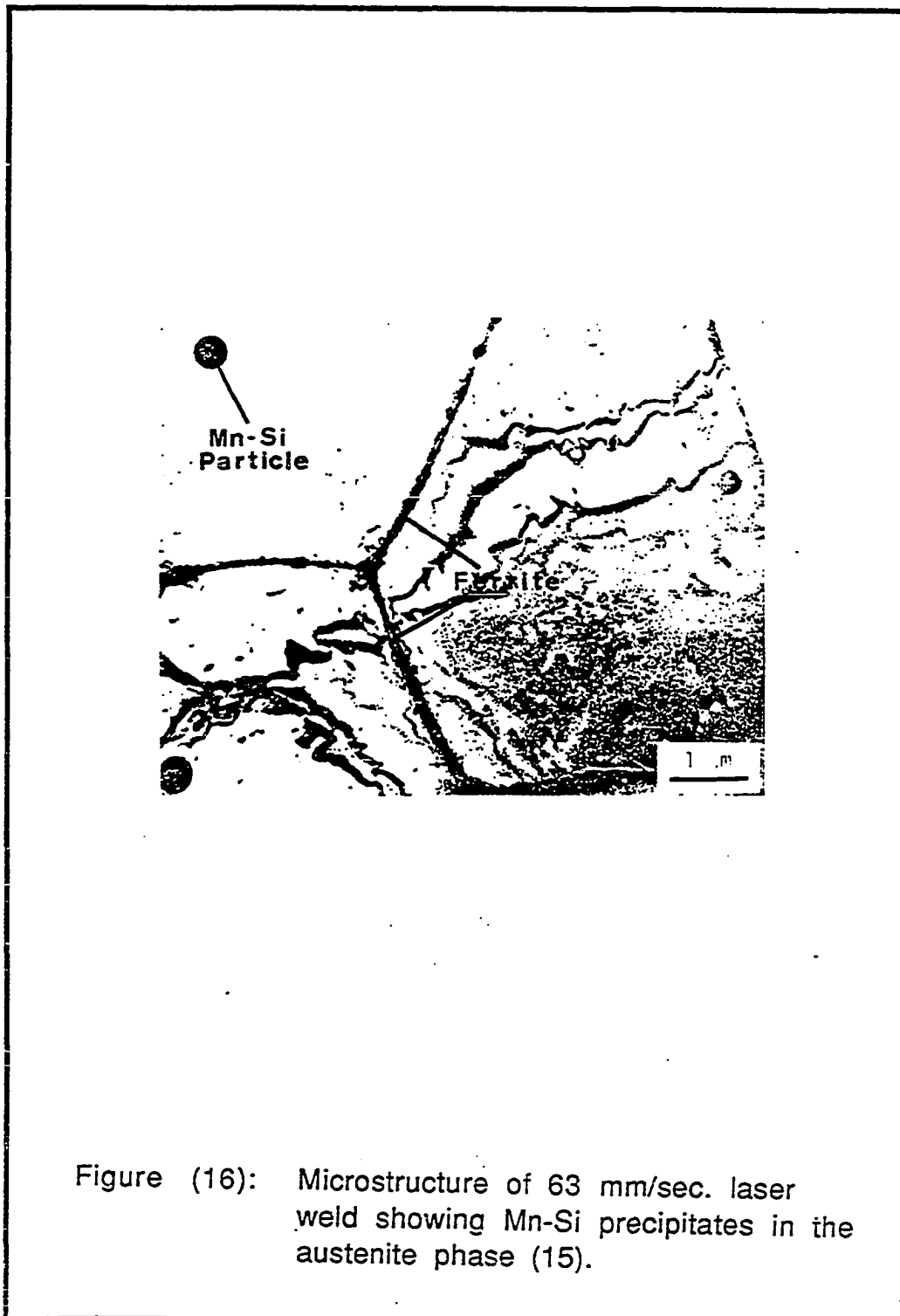


Figure (16): Microstructure of 63 mm/sec. laser weld showing Mn-Si precipitates in the austenite phase (15).

some detail by previous investigators (44,45). These rationales will be described very briefly:

- a) The higher solubility of harmful impurities in ferrite than in austenite results in less segregation during primary ferrite solidification than during primary austenite solidification (28).
- b) The thermal expansion coefficient of ferrite is less than that of austenite. This fact results in less thermal contraction on cooling of primary ferrite solidified welds (44,47).
- c) Partitioning of minor alloying elements during primary solidification can result in a synergistic behavior which affects cracking. During the solidification of ferrite, for example, Si may be less segregated to cell boundaries where it promotes liquid film formation, whereas Mn segregates to the cell boundaries where it reacts with S to form solid MnS, thus reducing the tendency for liquid sulfide film formation (28, 44).
- d) Cracks are arrested by the difficulty of propagation along a path of irregular ferrite-austenite boundaries rather than along rather smooth single-phase boundaries (44, 48).

As discussed above, many explanations have been put forth to explain the beneficial effect of ferrite in reducing weld hot cracking. However, there are probably two concepts which are most often quoted in the literature as being the major factors controlling weld cracking. These are the higher solubility of impurities in ferrite than in austenite and in the ferrite-austenite boundaries.

2) On mechanical and corrosion resistance properties: Despite the beneficial effect of delta ferrite in reducing hot cracking, the presence of ferrite in an austenitic matrix often results in either inadequate mechanical properties after extended service at elevated temperatures, or in reduced corrosion resistance. The tendency of delta ferrite to transform to the sigma phase at temperature between 400 and 900 °C (49, 50, 51) results in embrittlement of the weld metal. In addition, the resistance to stress-corrosion cracking can be significantly reduced when continuous or semi-continuous networks of delta ferrite are present in the structure (52).

Although ferrite acts as a strengthening agent in the weld metal, the subsequent drop in ductility is often undesirable. In addition, the presence of continuous ferrite networks (greater than 10 %) results in a decrease in impact properties, especially at elevated temperatures (52). Such duplex structure have also been shown to be less creep resistant than fully-austenitic alloys, although fatigue properties are comparable (52).

2.2.4 Proposed Mechanisms of Austenitic Stainless Steel Weld Metal

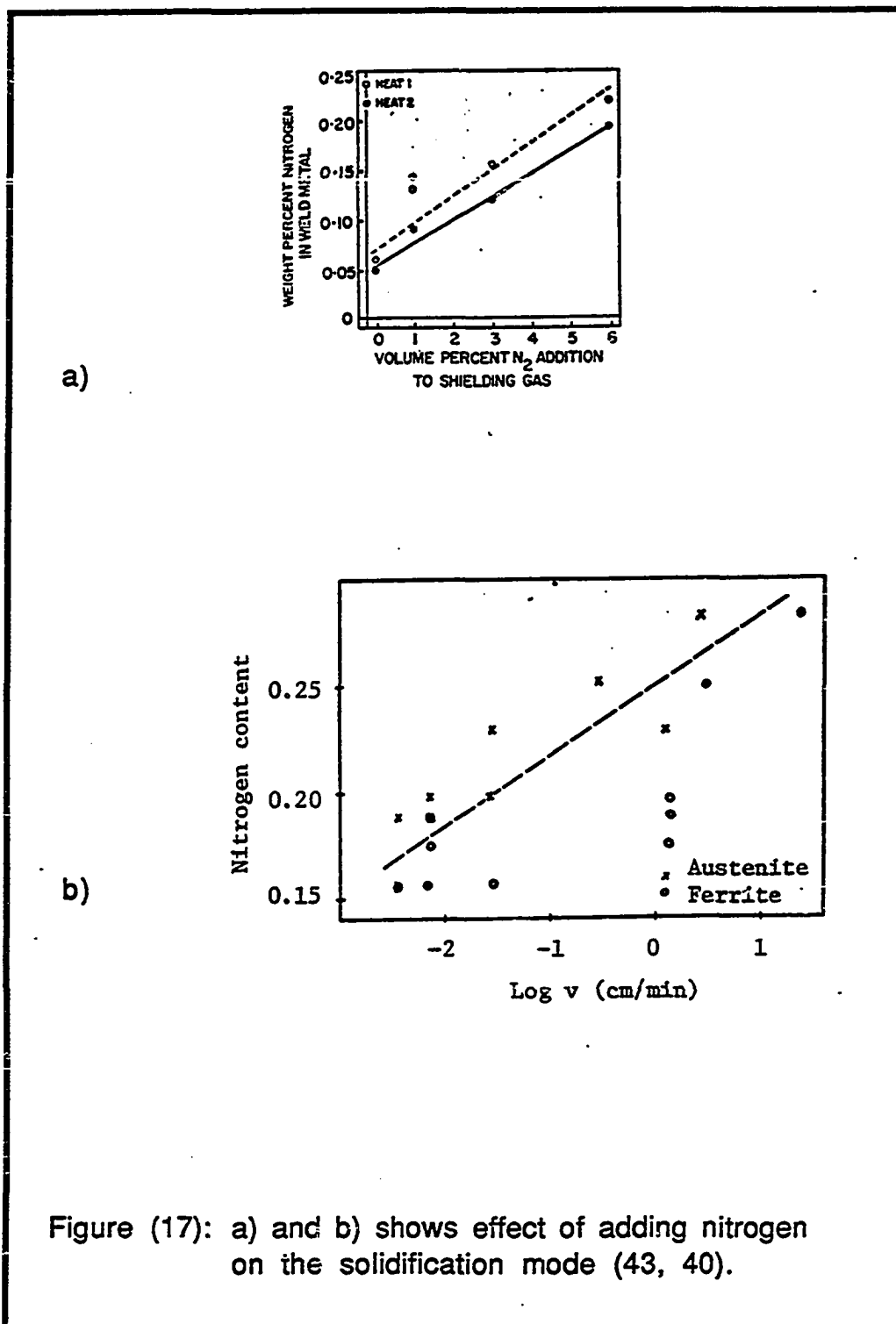
Several theories of duplex weld metal solidification and solid-state transformation have been proposed in the past twenty years. More recently Brooks et al. (29), Savage et al. (33,34), David et al. (37, 38), and Weatherly (40) have published papers proposing

solidification mechanisms for the austenitic stainless steel weld metal. In this section only these papers will be briefly reviewed.

In view of these papers, the following general mechanism can be deduced: Within the composition limits for a specific type of stainless steel, the balance between ferrite and austenite stabilizers is the major factor controlling the solidification mode. When ferrite stabilizers are dominant, delta-ferrite is the first solid to crystallize from the liquid; conversely when austenite stabilizers are predominant, austenite is the first solid to form from the liquid (29, 33, 34)

Other investigators (1, 43) attributed the change in solidification mode from delta to gamma to the increase in nitrogen content in the weld metal. Figures 17 a and b show the effect of adding nitrogen on the solidification mode. The amounts of nitrogen in the stainless steel melt were varied, in both experiments, by varying the partial pressure of nitrogen in the shielding gas.

On other hand, Lippold (39) and Weatherly et al. (40) have recently postulated that the conversion of primary delta-ferrite to austenite could occur by a diffusionless massive transformation as a result of the rapid cooling through the two-phase delta-plus-gamma region. This would apply to alloy compositions which lie on the Cr-rich side of the three-phase triangle on the pseudo-binary diagram where the primary solid phase is delta-ferrite. The transformation is characterized by the fact that the parent (delta-ferrite) and product (austenite) phases have the same chemical



composition but differ in crystal structure. Figure 18 is an optical micrograph which shows the massive austenite grains found in the samples that were rapidly quenched.

2.3 Summary

One of the most important concepts which can be drawn from this literature review is that the cooling rate associated with the solidification of metals and alloys can significantly change the final microstructure of the product. This is especially true when rapid cooling and solidification are encountered. For slow and moderate cooling rates such as occur in casting and normal arc welding processes, the composition is the primary factor controlling the structure and solidification mode. The effect of a slow cooling rate on the final structure of austenitic stainless steels is well known. However, the effect of cooling rate when the material is rapidly cooled is still not clearly understood.



Figure (18): Optical microstructure of a specimen cooled at 7000 C/sec. Massive austenite grains, with delta ferrite rims (39).

Chapter 3

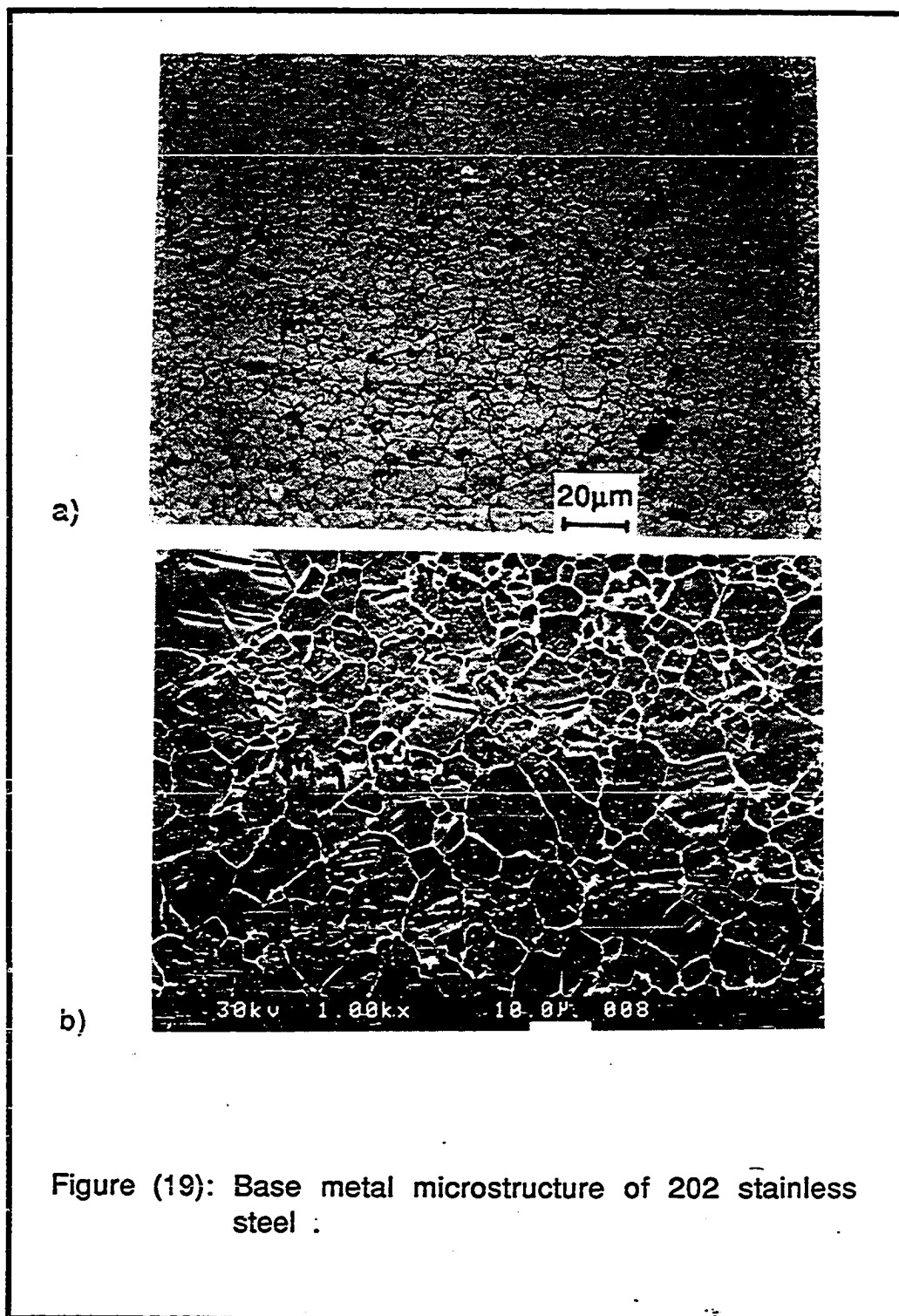
EXPERIMENTAL PROCEDURES

3.1 Material and Specimen Preparation

The materials used were 201 and 202 austenitic stainless steels containing a relatively high amount of manganese. The chemical compositions of these steels are given in table 1. The base metal microstructure is shown by optical microscope and SEM micrographs in figures 19 a and b and by TEM micrographs in figures 19 c and d. The structure consists of large austenite grains surrounded by delta ferrite. The 201 and 202 steel base metals were received as large plates about 30 cm long, 20 cm wide and 0.2 cm thick. Small 10 Cm x 5 Cm, pieces of both materials were cut on a band saw. Some of the pieces were used for melting and casting experiments. The others were cold rolled down to 0.1 cm using a two-high rolling mill. The rolled sheets, enclosed in a steel envelope, were then annealed for two hours at 1050 °F (565 °C) in an electric furnace. Re-rolling of the annealed specimens was performed after cleaning their surfaces. Final rolling to obtain 0.05 cm thick sheets was performed on a precision rolling mill. The

Table (1): Chemical compositions of AISI 201 and 202 high-Manganese stainless steels

ELEMENT	201 Wt. %	202 Wt. %
C	0.073	0.098
Mn	7.15	7.480
P	0.035	0.039
S	0.004	0.006
Si	0.560	0.470
Ni	4.870	4.720
Cr	17.00	17.85
N	0.069	0.070
Fe	Balance	Balance



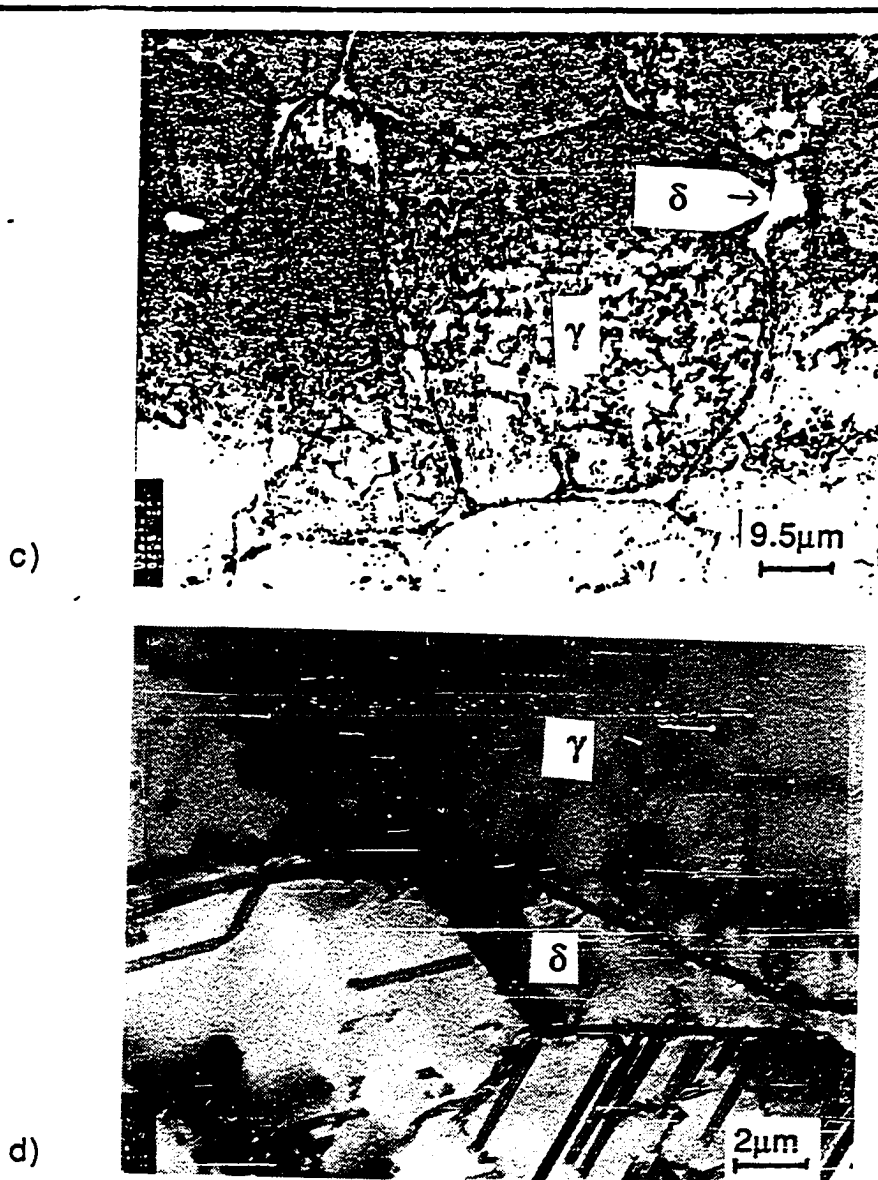


Figure (19): (Continued)

rolled sheets were then cut into approximately 5 cm x 2.5 cm pieces using a shear. Each specimen was thoroughly cleaned with acetone, and dried to remove any moisture which might lead to oxidation.

3.2 Melting and Casting

The 201 stainless steel samples used for the slow cooling solidification studies and cooling rate determinations were prepared by nonconsumable electrode arc melting using a drop casting furnace, which is shown in figure 20.

Typically, for alloy melting a solid hemispherical copper hearth was inserted into the hearth support, the charge of 201 stainless steel added, and the furnace chamber sealed. The furnace was purged three times by evacuating to 10^{-3} torr and then backfilling with argon to 1 atmosphere. The charge was melted, inverted, and remelted a total of three times. The alloy button was cooled to room temperature, the furnace chamber opened to the atmosphere, and the solid button removed.

For drop casting, the solid hearth was removed, and a split drop casting hearth support aligned so that the insert orifice was above the mold cavity. The hemispherical alloy button was placed within the drop casting hearth, the furnace closed, and the purging and getting operation repeated. The 201 stainless steel was first melted, then the power was increased with the arc positioned

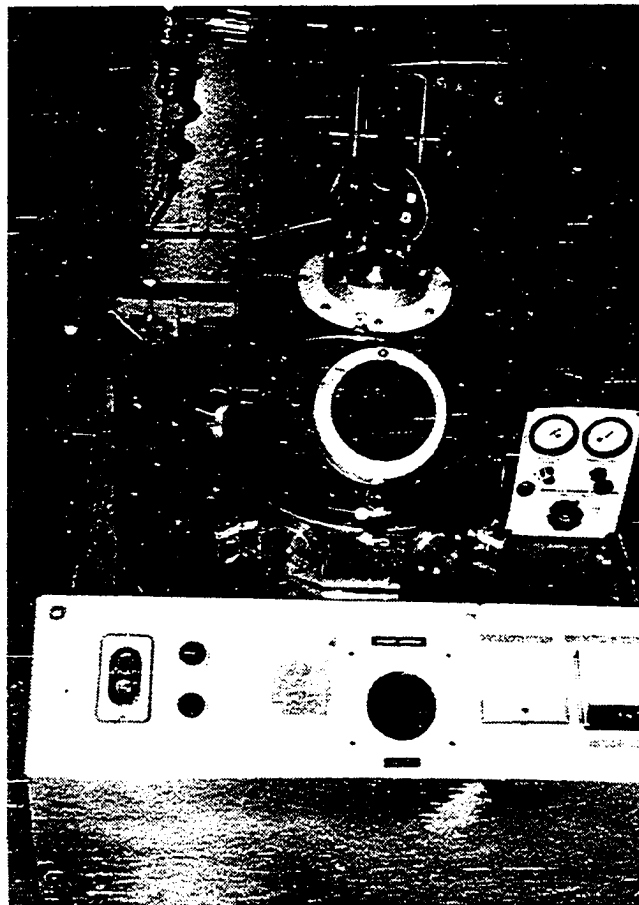


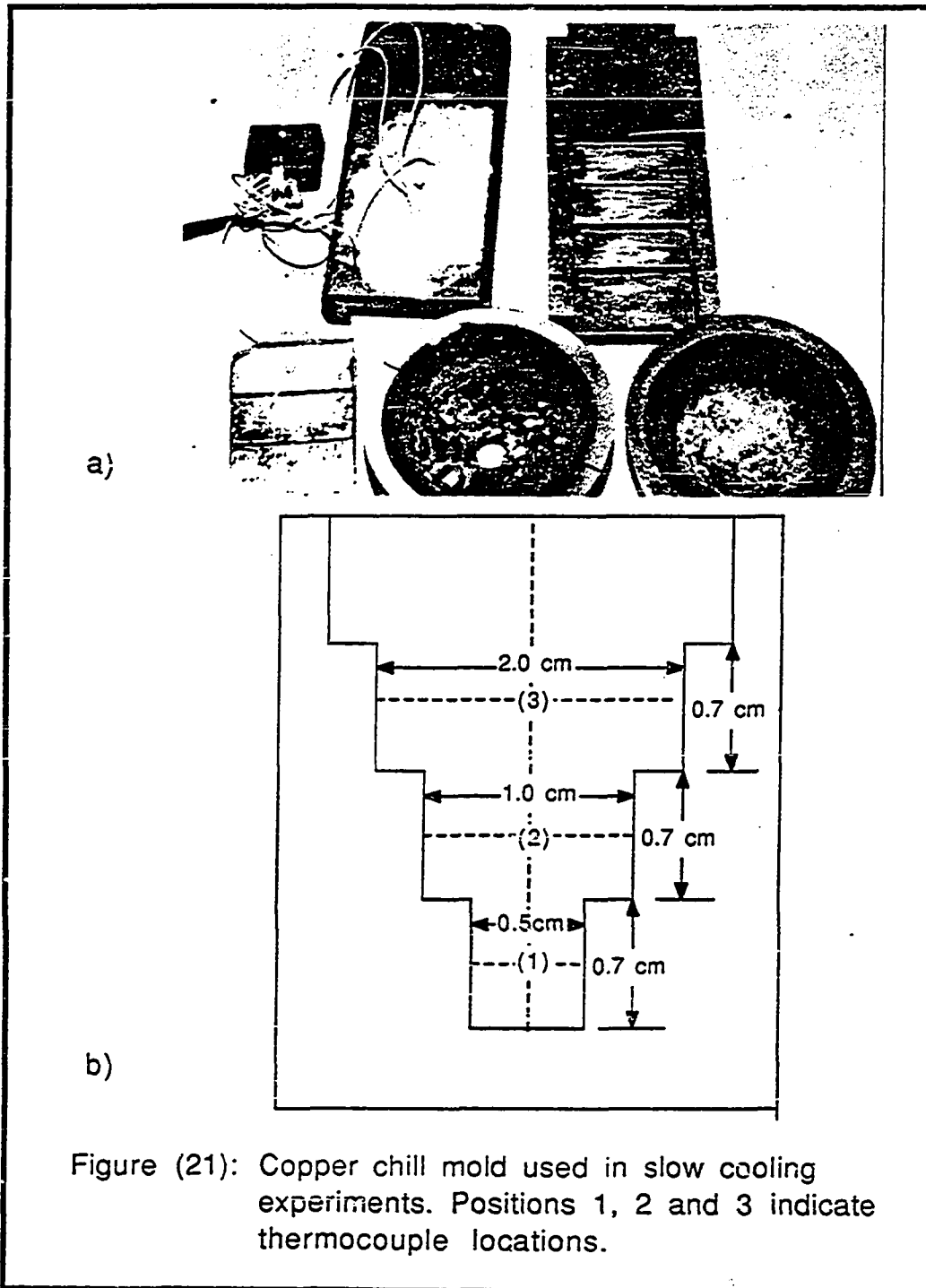
Figure (20): A drop casting furnace used in the melting and casting experiment.

directly over the drop casting orifice until the skull over the orifice melted and the alloy was drop cast.

To obtain different cooling rates a stepped water-cooled copper chill mold was used. Figures 21 a and b illustrate the copper chill mold and one 201 stainless steel ingot. Note the location of the thermocouple used to measure cooling rates along the center line of the casting. Pt-Pt 10 Rh thermocouples, located at the center line positions denoted 1, 2, and 3 in figure 21 a, 0.25, 0.5 and 1.0 cm from the chill wall respectively, were used to measure cooling rates. The thermocouples were fabricated by inserting 0.005 inch diameter wire into double bore alumina thermocouple insulators, welding, and coating the tips with a slurry of alumina powder in polyvinyle alcohol and water.

3.3 Welding

All the welding experiments were conducted using a carbon dioxide laser, the coherent model everlase # 525-1. This laser is capable of producing a maximum output power of 575 watts in the continuous mode. Samples of 201 and 202 stainless steel, approximately 5 cm long, 2.5 cm wide and 0.05 cm thick, were irradiated by the laser beam. Samples were placed on a computer controlled, electrically operated, table capable of providing linear motion in x and y directions. All welding was carried out inside a plexiglass box, which stopped any stray reflected laser beams and



maintained an inert atmosphere. Ultra purity helium gas was used for shielding. This helium provides a controlled atmosphere during the experiments and flushes the laser plasma from the laser beam /material interaction site. The helium flow rate was monitored by using a calibrated flow meter. The laser beam was focused on the workpiece by means of a 1.0-in diameter ZnSe (zinc selenide) lens with a 5.0-in focal length.

3.4 Metallographic Procedures

The instruments used in this investigation were the optical (OM) and scanning electron microscope (SEM) for analyzing the slow cooled and the laser welded samples, and the transmission electron microscope (TEM) for identifying the phases present in the welded metal microstructure. A Kevex x-ray microanalyzer also used to analyze the weld metal chemical composition.

The welded samples to be examined by OM and SEM were sectioned and mechanically ground on a series of 240, 300, 400 and 600 grit SiC papers. The samples were then polished with 1 micron and 0.5 micron diamond paper and then etched. Etching was conducted with two different etchants, a dilute oxalic acid (10 gm oxalic acid and 100 mg water) to reveal any carbides and sigma phases and Kalling's reagent to reveal ferrite and austenite. The latter reagent, which consists of 2 gm CuCl_2 , 40 ml HCl and 80 ml methanol, attacks the ferrite phase and leaves the austenite phase

unattacked. This etchant was especially effective with highly cored microstructures such as those which solidify as primary austenite. The etching time varied from 10 to 15 seconds.

To identify the phases present in the laser weld metal thin foils were prepared from the welds for examination using the TEM.

Due to the very small width of the laser weld (< 1mm) and to the fact that the surrounding base metal is more easily attacked by the polishing solution than is the weld itself, the possibility of getting a good TEM specimen is very small. Also, the small width of the laser weld metal makes the masking technique very difficult to use. To overcome these difficulties, a large number of specimens was prepared.

The laser welded samples were reduced in thickness to 0.03 mm and discs 3 mm in diameter were punched out in such a way that the laser pass had passed through the center of each disc. All discs were thinned in a solution containing 10 % perchloric acid, 20 % glycerol and 70 % ethanol using a twin-jet polisher. The foils were examined in a Philips 420 electron microscope operated at 120 KV.

Chapter 4

RESULTS AND DISCUSSIONS

4.1 Cooling Rate, Solidification Growth Rate, and Temperature Gradient of the 201 Steel Laser Weld Metal

4.1.1 Cooling Rate

In the first two chapters it was mentioned that high cooling rates can significantly alter the structure of the solidified region. Hence, the determination of the cooling rate of the laser weld metal is an important factor to be considered.

Because cooling rate measurements are difficult to make for the laser welded material, the possibility of using a structural characteristic such as the dendrite spacing as a measure of the cooling rate is of great interest. The spacing of dendrite arms is known to be a function of the degree of undercooling, and, since the extent of undercooling depends on the rate of cooling, one can expect a relation between secondary dendrite arm spacing (SDAS) and cooling rate. Accordingly, the cooling rates of three 201 stainless

steel casts (cooling rate of 100°C /sec. or less) were experimentally measured at the melting point of the alloy (1811 K), as explained in chapter 3, and plotted versus the secondary dendrite arm spacings (SDAS) measured from these casts. Table 2 shows the measured cooling rates of the three 201 casts and the corresponding values of SDAS, while figure 22 shows SDAS for casts cooled at 1, 45 and 100 °C/Sec. It is clearly seen that the SDAS decreases as the cooling rate increases. The relation between cooling rate and SDAS is linear when plotted on log-log coordinates as shown in figure 23. The relation found to be in good agreement with another work done by Brower, Strachan and Flemings (53) on commercial alloy 440C as shown in figure 23. The major alloying elements of 440C being 17 % Cr and 1 % Mn. This relation was extrapolated to high cooling rates. The following equation relating the cooling rate (r) to the SDAS (microns) has been determined from this plot.

$$\text{SDAS} = 47 \cdot r^{-0.41} \dots\dots\dots 1$$

Using this equation, the cooling rates for a number of 201 and 202 stainless steel samples laser welded at different welding speeds were determined using the measured values of SDAS. Table 3 shows the measured SDAS and the corresponding cooling rates. Figures 24 a and b show two SEM micrographs for dendrite arms of 202 steel samples laser welded at 20 mm/sec. and 31 mm/sec.

Theoretically, local cooling rate, r, is a result of product of solidification rate, R, and temperature gradient, G, as follows:

$$r \text{ (}^\circ\text{C/sec)} = R \cdot G \text{ (cm/sec) (}^\circ\text{C/cm) } \dots\dots\dots 2$$

Table (2): The cooling rates of the three 201 casts measured at the melting point and the corresponding secondary dendrite arm spacings (SDAS)

COOLING RATE	SDAS
C/sec.	Microns
1.00	47.0
45.0	10.0
100	7.00

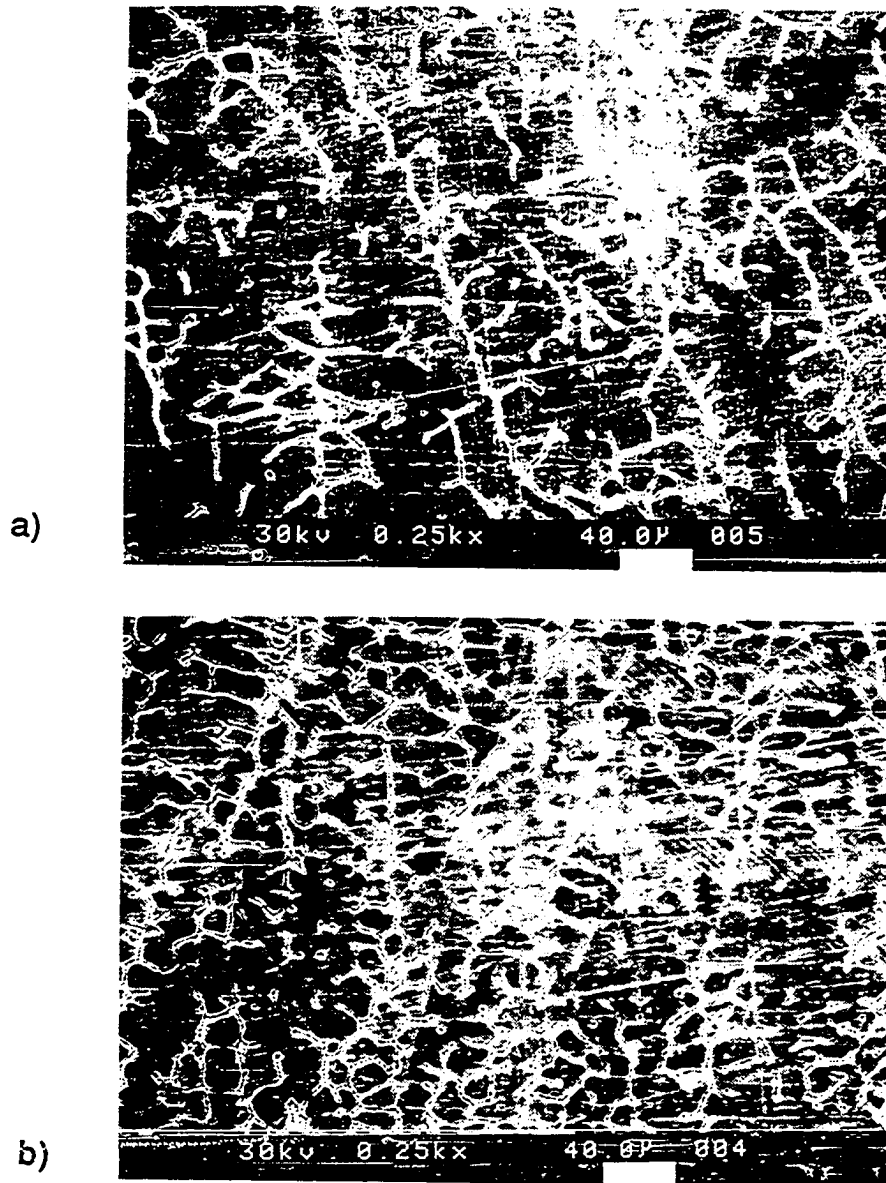


Figure (22): SEM micrographs showing secondary dendrite arm spacings for casts cooled at 1,45 and 100 C/sec.

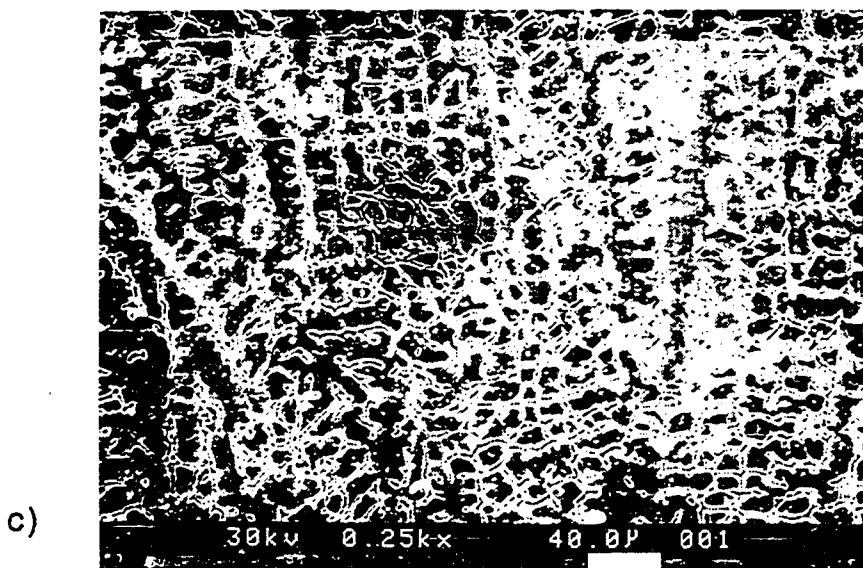
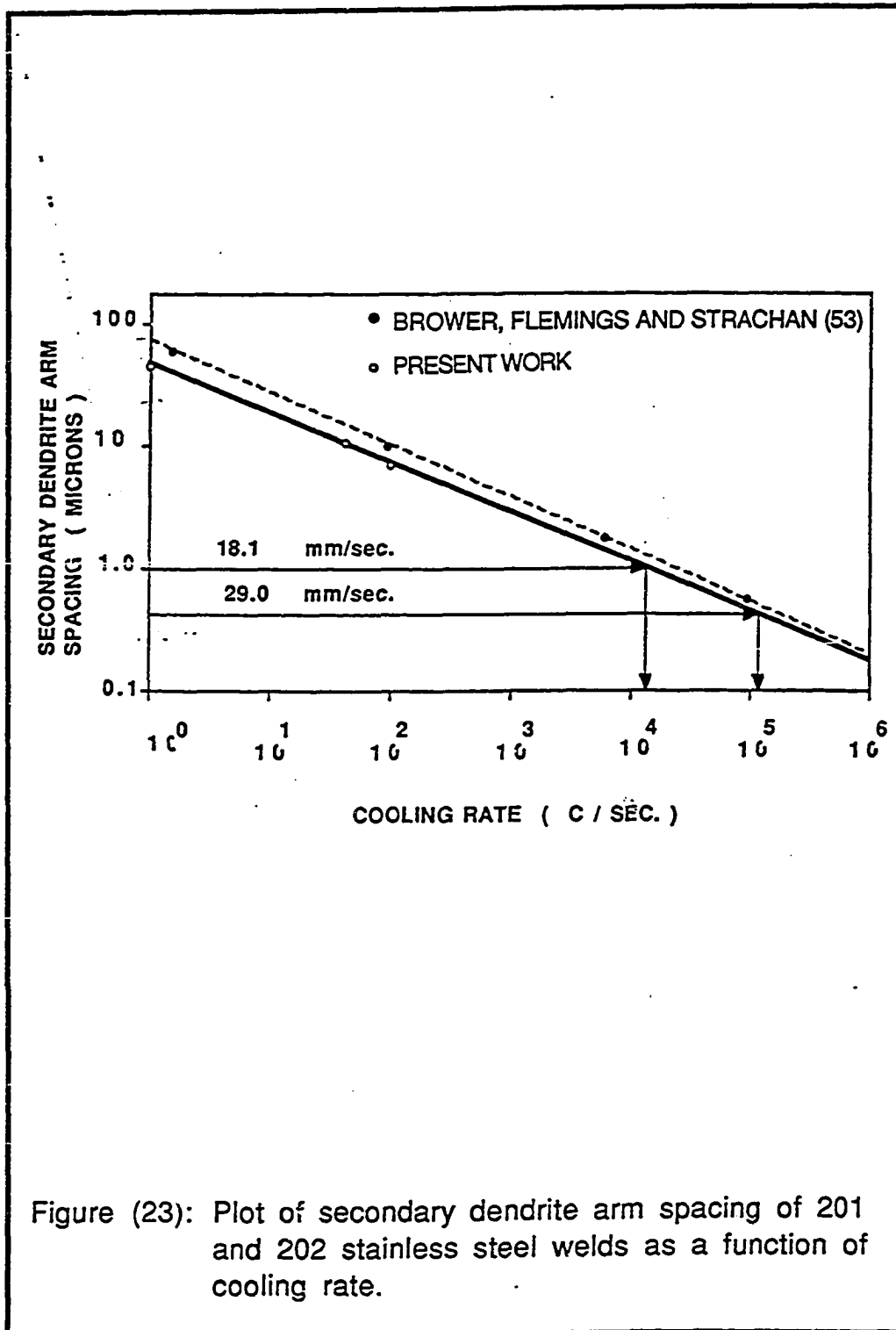


Figure (22): (Continued)



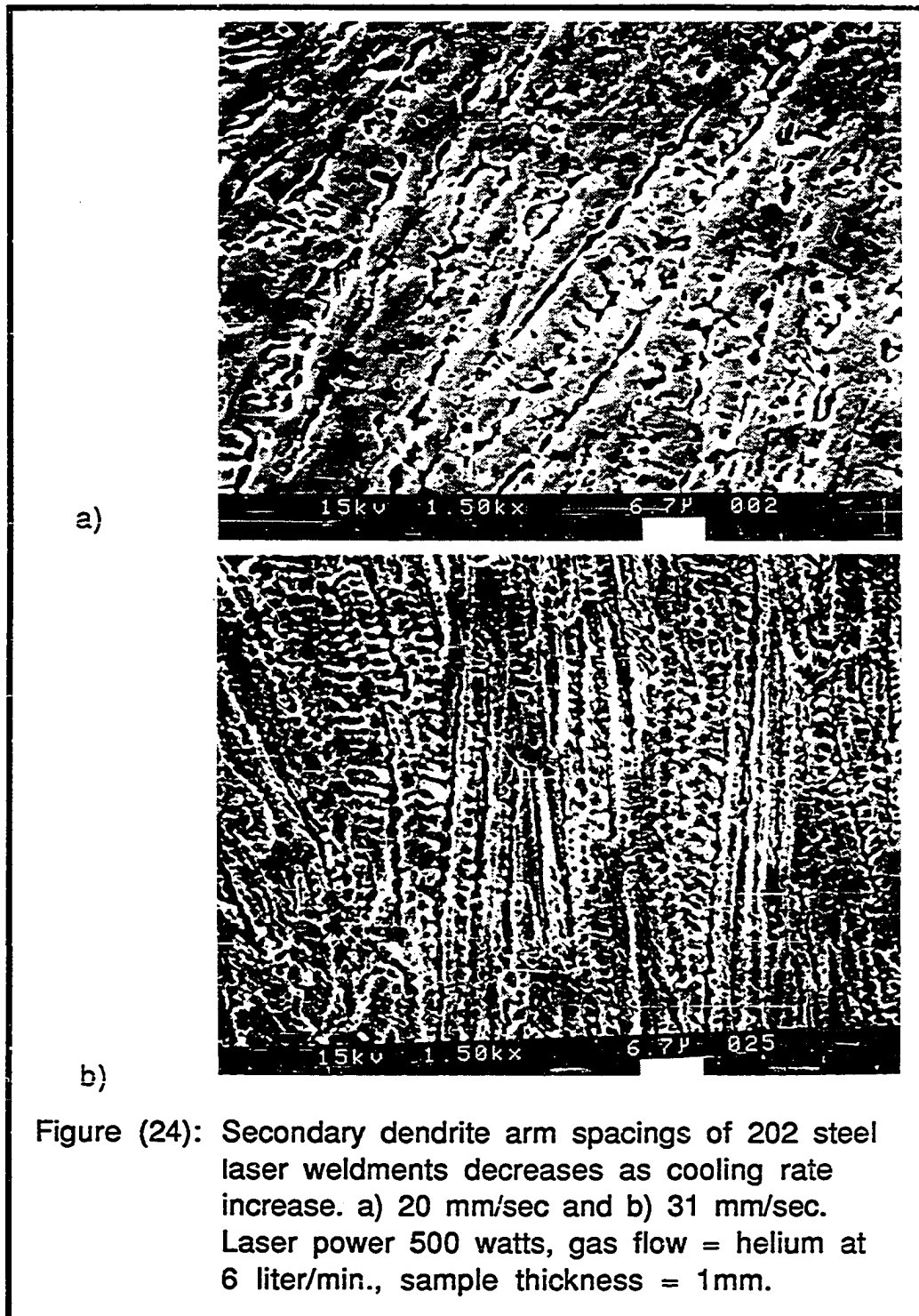


Table (3) : The measured secondary dendrite arm spacings (SDAS) of the 202 stainless steel laser weldments and the corresponding cooling rates determined using plot in figure 23. Laser power 500 watts, gas flow = helium at 6 liter/min., sample thickness =1 mm.

VELOCITY mm/sec	SDAS μm	COOLING RATE C/sec.
10.0	1.0	0.12×10^5
20.0	0.5	0.65×10^5
30.0	0.4	1.12×10^5
40.0	0.3	2.20×10^5

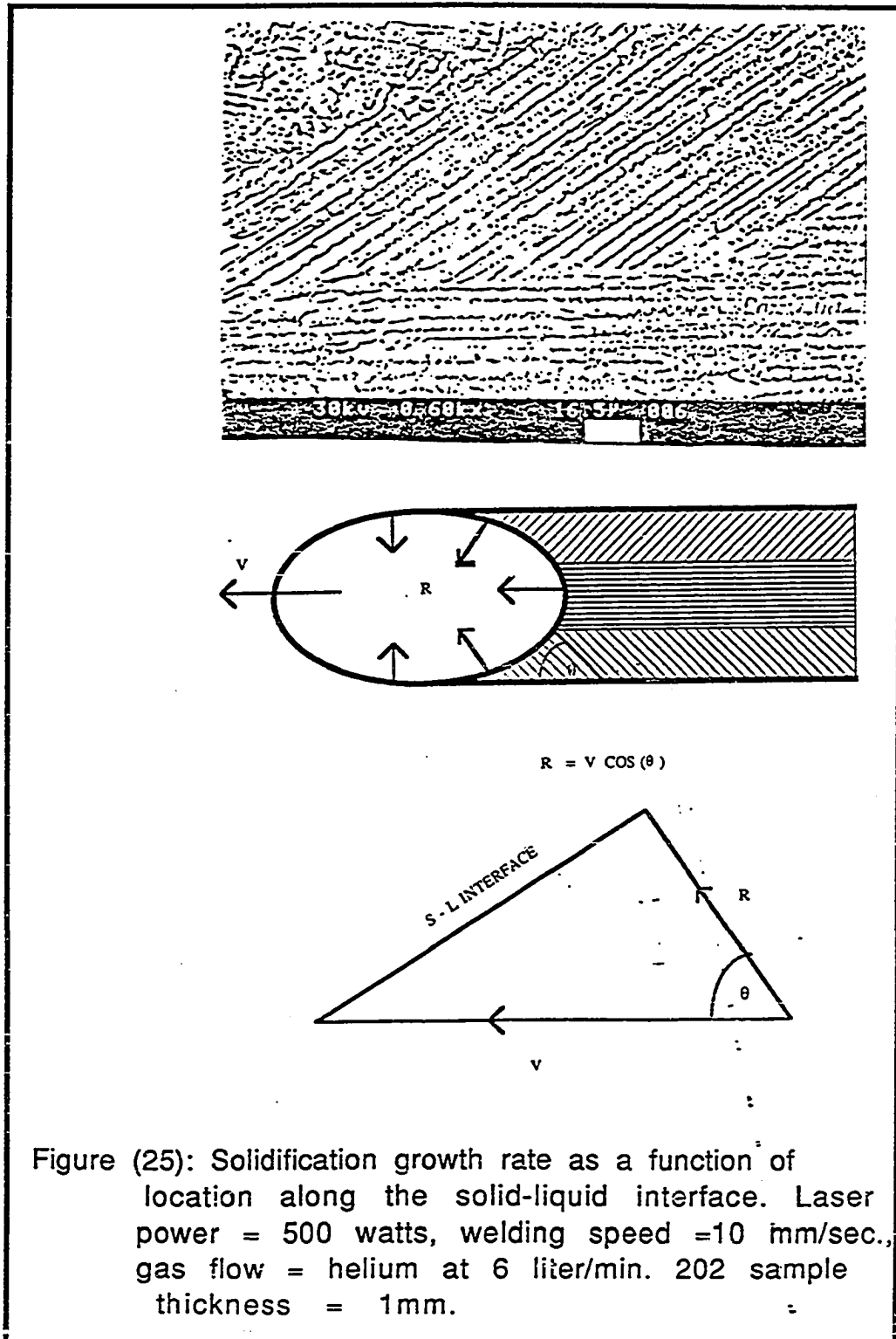
Solidification rate, R , is related to the laser welding speed, V , as follows:

$$R = V \cos \theta \dots\dots\dots 3$$

where θ is the angle between the welding direction and the solid-liquid interface as shown in figure (25).

Several samples laser welded at different welding speeds were longitudinally ground, polished and etched and an average value of θ was measured for each weld using optical microscopy. Figure 26 a and b show two SEM micrographs of the crystal growth direction for two samples welded at 10 and 75 mm/sec. It can be seen that the growth angle gets smaller as the welding speed increases. From the relation $R = V \cos \theta$, one can expect R to increase as the angle θ decreases. The solidification rate, R , reaches its maximum when θ is zero and equal to the welding velocity, V , since $\cos 0 = 1$. When θ equals zero, the crystal growth direction is parallel to the laser welding direction as shown in figure 25. Table 4 shows values of measured θ at different welding velocities and the corresponding values of solidification growth rate, R .

Once again, the cooling rate is the product of R and G , where R is determined as explained above, while G can be predicted using the method of Pauli (54). He numerically predicted temperature fields at several locations in the laser solidified weld pool. The temperature distributions were determined by computer solution of the equations of conservation of energy and momentum, and mass continuity



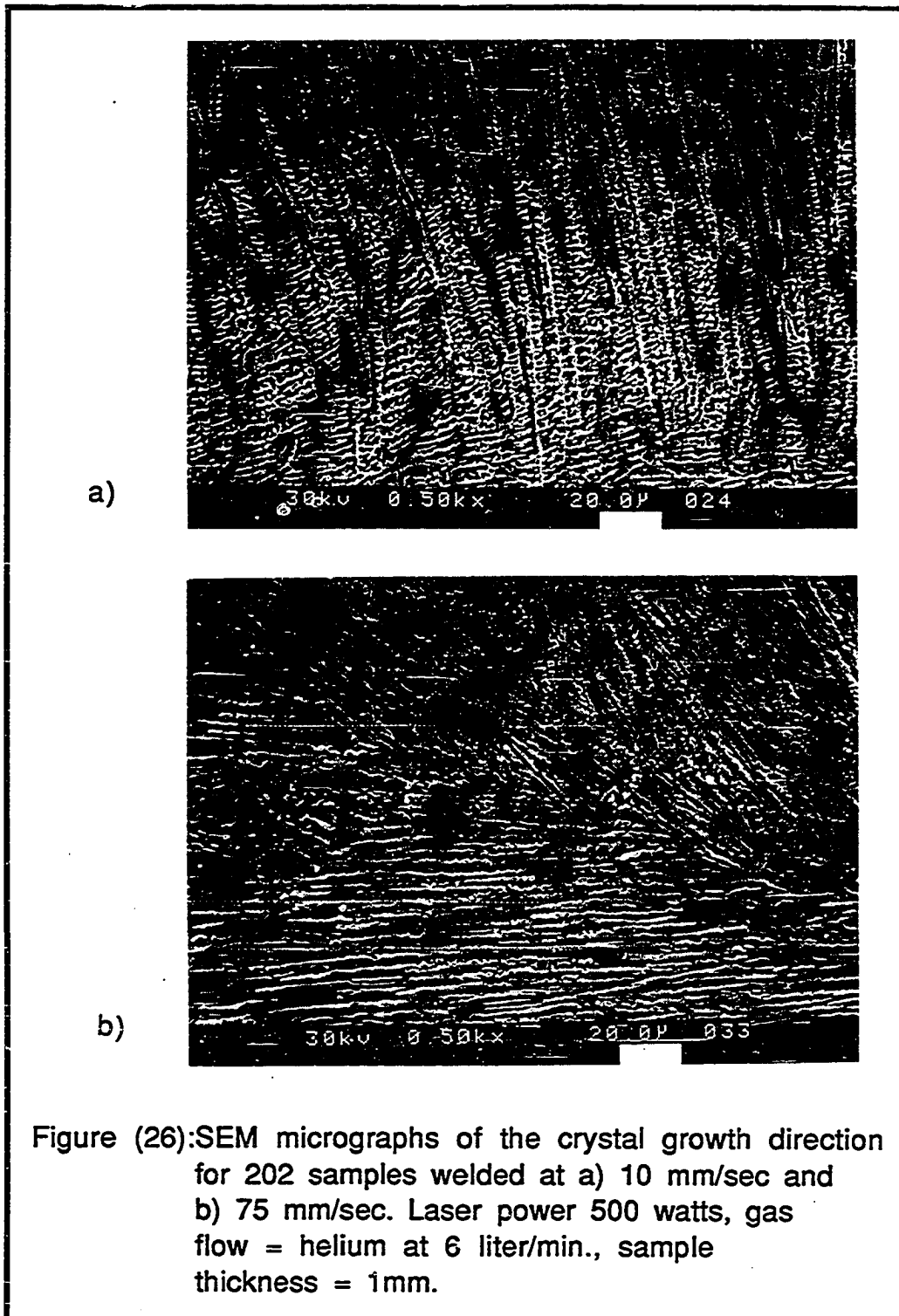


Table (4) : Measured values of (θ) at different welding speed (V) and the corresponding values of solidification rate (R) of 202 steel. Laser power 500 watts, gas flow = helium at 6 liter/min., sample thickness =1 mm.

V mm/sec	θ degrees	R mm/sec
5	37	4.0
10	30	8.7
20	25	18.1
31	22	29.0
40	21	37.0

equation. In formulating the model, the following assumptions were made:

- 1) The fluid flow and heat transfer inside the molten pool are adequately described by a two-dimensional, time-dependent, constant density representation.
- 2) The flow is primarily driven by the surface tension gradient produced as a result of the temperature gradient at the surface.
- 3) The power distribution of the laser beam is gaussian.

In two-dimensions the energy equation which was used to calculate the temperature distribution is :

$$\left(\frac{\partial H}{\partial t}\right) + u \left(\frac{\partial H}{\partial x}\right) + v \left(\frac{\partial H}{\partial y}\right) = K / \rho C_p \left[\left(\frac{\partial^2 H}{\partial x^2}\right) + \left(\frac{\partial^2 H}{\partial y^2}\right) \right] + S_H \dots\dots\dots 4$$

The laser power and welding speed (V) were included in the source term, S_H , by the following expressions :

$$S_H = \varepsilon \cdot J_H / Y_d \cdot \rho \dots\dots\dots 5$$

where;

$$J_H = \left(\frac{3 Q}{\pi r_b^2} \right) e^{-\left[\frac{3 (x+Vt)^2}{r^2} \right]} \dots\dots\dots 6$$

all the symbols are given in nomenclature.

The boundary conditions used for the solutions of change are described below.

Energy equation:

- 1) At the surface of the sample the source term was zero except for the region which was directly under the laser beam. For this region the source term was given by the gaussian expression (equation 5).

- 2) The heat transfer between the surface of the sample (which was not under the laser beam) and the surroundings was an input parameter.
- 3) In the transverse section of the sample, since symmetry was assumed about the laser beam, there was no heat flow across the plane of symmetry (center line).
- 4) The heat transfer at the bottom and the sides of the plate was calculated by equating the conduction heat flux with the heat due to convection from the plate surface.

Momentum equations:

- 1) In the transverse cross-section of the pool the mass transfer across the center-plane was zero ($u=0$) as symmetry was assumed.
- 2) At the surface of the pool the Marangoni effect was incorporated by equating the shear stress at the surface to the gradient of surface tension.
- 3) All velocities at the solid/liquid interface were zero as no-slip conditions were assumed.

Using Paul model, the temperature distribution has been predicted for different welding speeds and powers. Temperature gradients, G , were calculated near to the solid-liquid interface where the temperature is about the freezing point of the alloy from these numerically predicted temperature fields and tabulated in table 5.

Table (5): The local cooling rate of the laser weld metal determined by the product of the solidification growth rate and the computed temperature gradient.

POWER Watts	VELOCITY Cm/sec	R Cm/sec	G C/cm	r C/sec
300	1.0	0.87	53800	0.5×10^5
	3.0	2.8	64650	2×10^5
400	1.0	0.87	93150	0.8×10^5
	3.0	2.8	113400	3.2×10^5
500	1.0	0.87	94250	0.82×10^5
	2.0	1.81	134500	2.4×10^5
	4.0	3.7	148550	5.5×10^5

The local cooling rates for stainless steel welded at different speed and powers were determined by the product of the G values calculated above and the values of R given in the same table 5.

Lancaster (55) has presented a formalism to predict cooling rates based on three-dimensional analytical heat conduction model. Since that the physical properties governing the heat flow such as thermal conductivity and diffusivity vary with temperature along the weld pool, the Lancaster analytical solutions will only give an approximation to the actual temperature distribution. The expressions of the three-dimensional equation is:

$$(\partial T / \partial t) = - (V T_m / x_1) \dots\dots\dots 7$$

Where x_1 is the distance from the laser beam to the trailing edge of the pool ($x_1=0.021$ cm), T_m is the melting point (=1811K) and $K_1(Z)$ and $K_0(Z)$ are modified Bessel functions of the second kind. Cooling rates were calculated by the 3-D equation and are tabulated in table 6.

A comparison of the cooling rates determined by the three methods: the SDAS, the product of R and G, and the three-dimensional Lancaster formula is given in table 6. It can be seen that the cooling rates obtained by SDAS are consistent with those obtained using the other methods.

Table (6): A comparison of the cooling rates of 202 stainless steel weldments determined by the three methods, the SDAS, the product of R and G, and the 3-D Lancaster formula. Laser power 500 watts, gas flow = helium at 6liter/min., sample thickness =1 mm.

VELOCITY mm/sec	COOLING RATE		
	C/sec		
	SDAS	GR	3D
1.0	0.12×10^5	0.82×10^5	0.86×10^5
2.0	0.65×10^5	2.4×10^5	1.7×10^5
3.0	1.12×10^5	3.7×10^5	2.5×10^5
4.0	2.20×10^5	5.5×10^5	3.4×10^5

4.2 Effect of Solidification Growth Rate on Laser Weld METAL CHARACTERISTICS

4.2.1 Geometry of the Weld Metal

Figure 27 shows top and longitudinal views of 201 stainless steel specimens welded at various scanning rates by a 500 watt laser beam. The as-irradiated surface exhibits semicircular markings which indicate the shape of the back side of the molten zone. These markings, which correspond to a periodic undulation in the surface elevation, are believed to result from an overflowing of the melt pool due to periodic variations in beam temperature. Such temperature fluctuations may arise due to periodic variations in beam power or scan rate. The shape of these back side markings was found to vary with the scan rate. From figure 27, the weld shape changes from semi-circular at low weld rate (figure 27-a) to elliptical at high speed (figure 27-b). As the rate is increased the molten pool takes on a teardrop shape indicating that the heat is being increasingly withdrawn at the sides rather than the back of the molten pool.

Figure 28 shows the effect of increasing scanning rate on the weld pool depth, and width of the laser weld metal and thickness of heat affected zone (HAZ). Increasing the scanning rate, at constant power, results in a decrease in all these dimensions. The decrease in the size of the weld pool is due to the reduction in interaction time

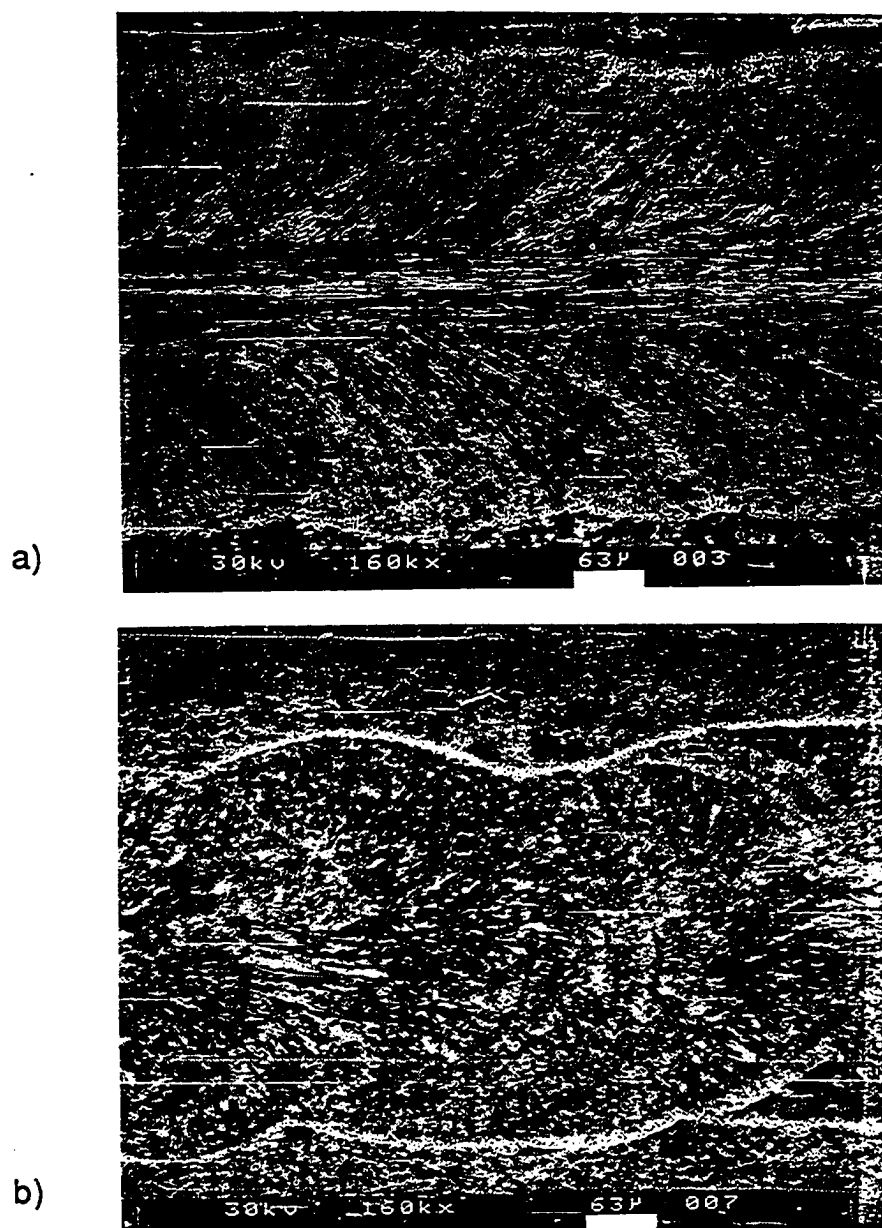
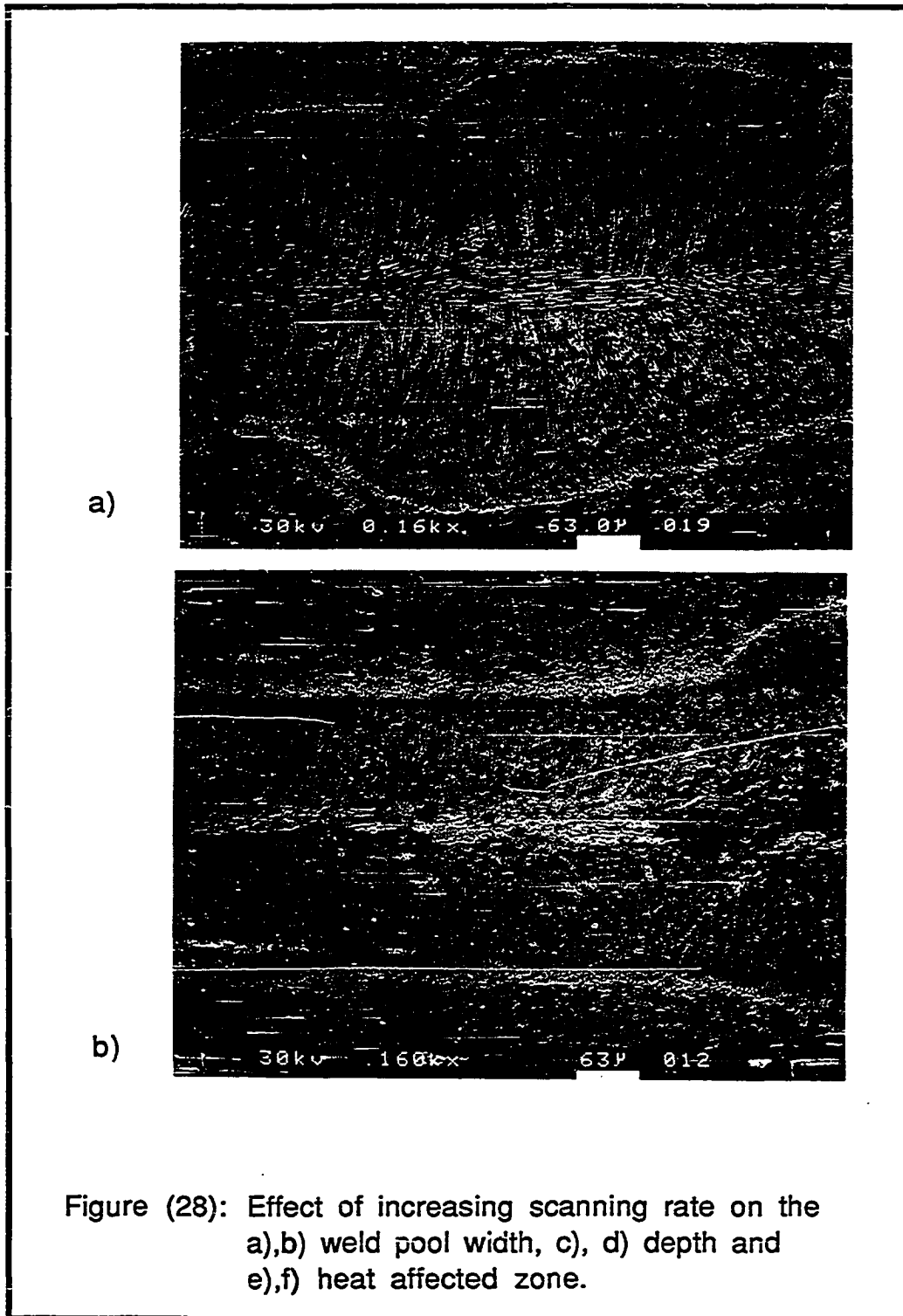
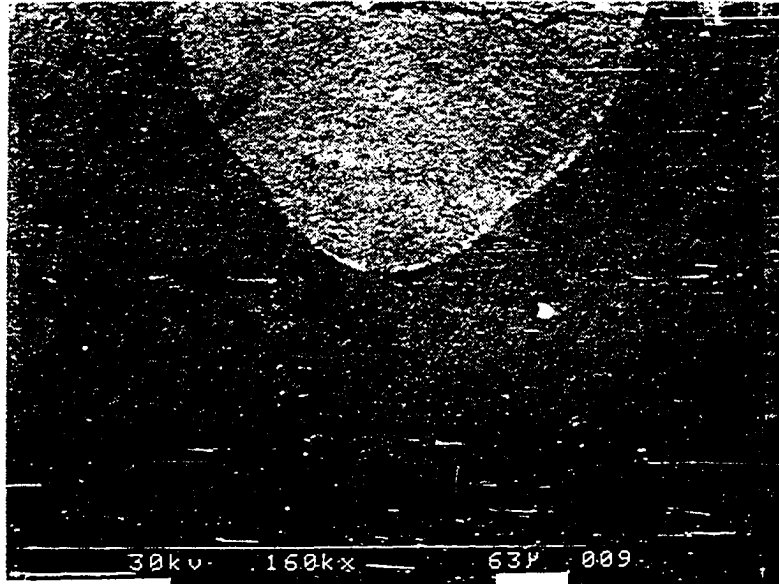
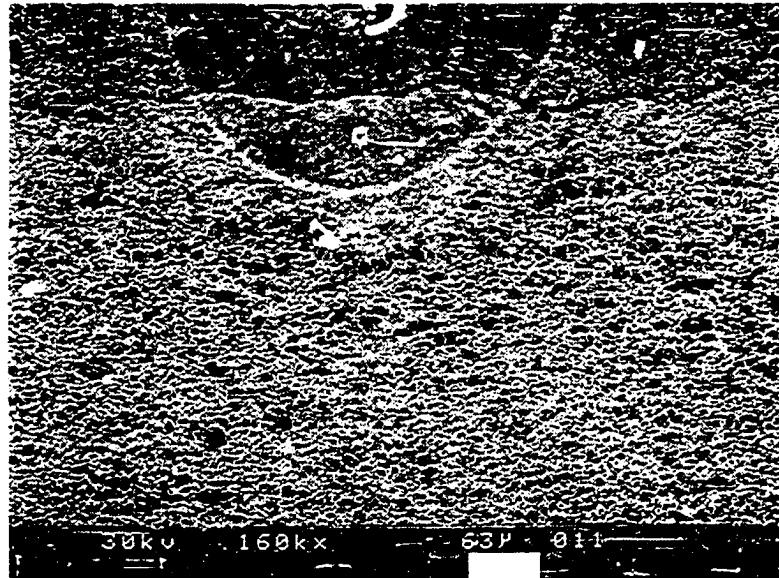


Figure (27): Top views of two 202 stainless steel samples welded at a) 1 mm/sec and b) 20 mm/sec.





c) R=18.1mm/sec.



d) R=29 mm/sec.

Figure (28): (Continued)

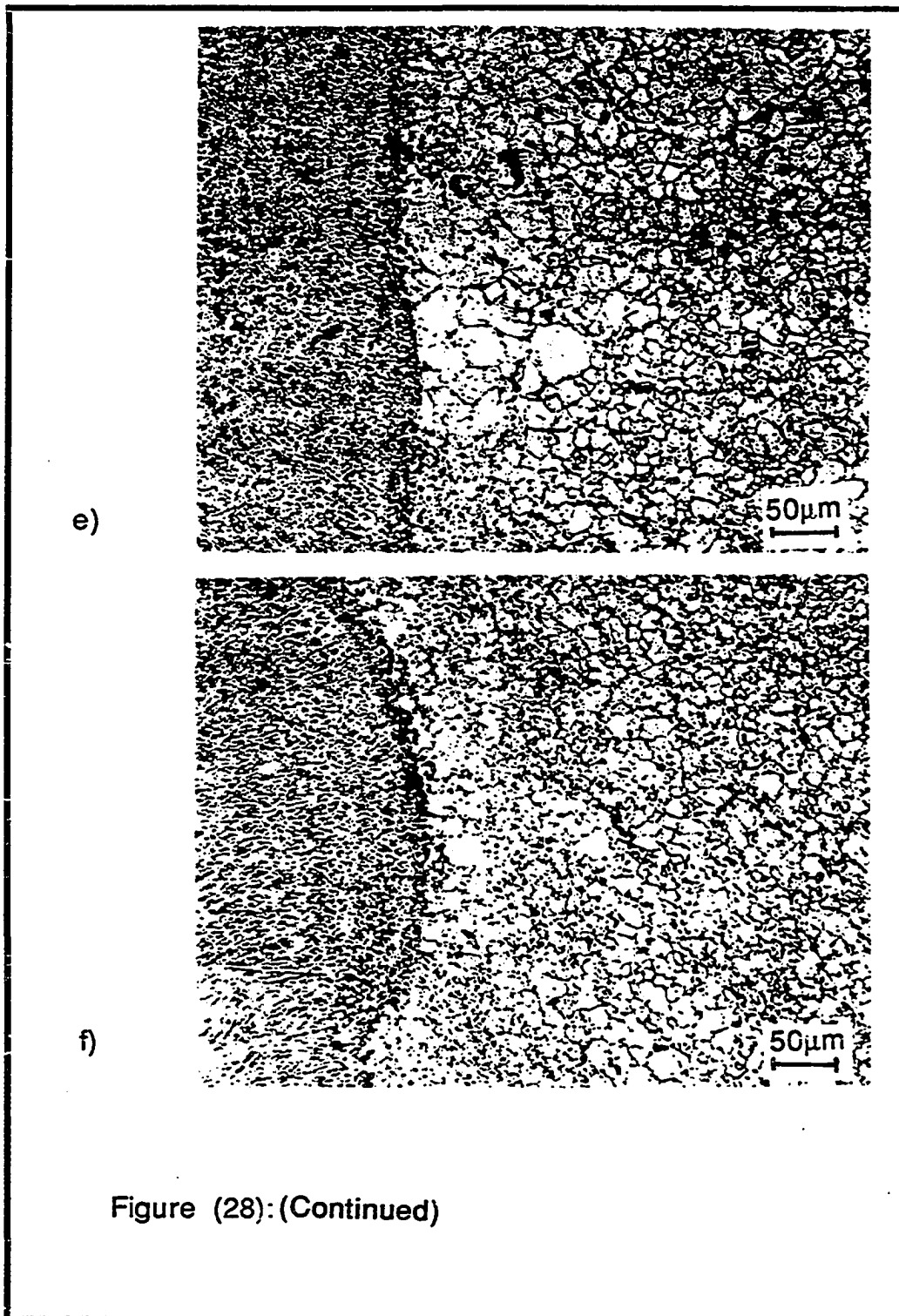


Figure (28): (Continued)

and heat input at higher welding speeds. The size of the HAZ also decreases as scanning rate increases. The measurement values of HAZ and depth and width of the weld metal are given in table 7.

4.2.2 Primary and Secondary Dendrite Arm Spacings

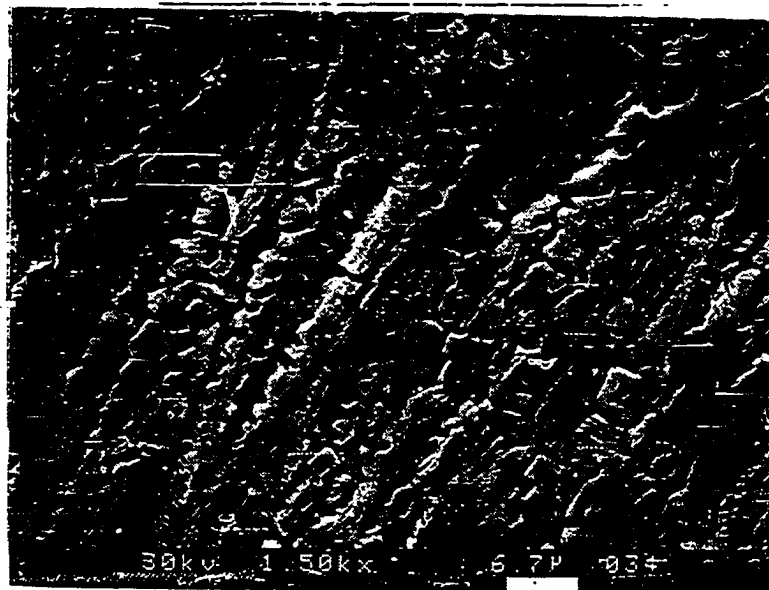
Primary and secondary dendrite arm spacings were measured directly from the longitudinal sections both by using a microscope with a calibrated scale within the eyepiece and by measuring the spacings from the SEM micrographs. All the measurements of primary and secondary arm spacings were taken from the center of the welds. Figure 29 a-d is of SEM micrographs showing that dendrite arm spacing decreases as R increases. The scatter in the measurements was reduced by averaging over groups of up to 10 arms. The measurements were made from several arms for several welded samples solidified at different rates. The values of arm spacings are tabulated in table 8. The average primary and secondary dendrite arm spacings were related to the solidification growth rate, R, as shown in figure 30. The error bars represent $\pm 1\sigma$ limits expected for the data. From this figure, it can be seen that the points fall on one reasonably straight line. It is clear that both primary and secondary arm spacings decrease as solidification rate increases. This is because of the fast freezing time at high solidification growth rates. To illustrate the influence of

Table (7): Depth, width and thickness of heat affected zone (HAZ) of 202 steel laser weld metal as a function of solidification growth rate (R).
Laser power 500 watts, gas flow = helium at 6 liter/min., sample thickness =1 mm.

R mm/sec	WELD DEPTH mm	WELD WIDTH mm	THICKNESS OF HAZ mm
4.0	0.41	0.66	0.12
8.7	0.35	0.50	0.09
18.1	0.25	0.42	0.063
29	0.16	0.34	0.044

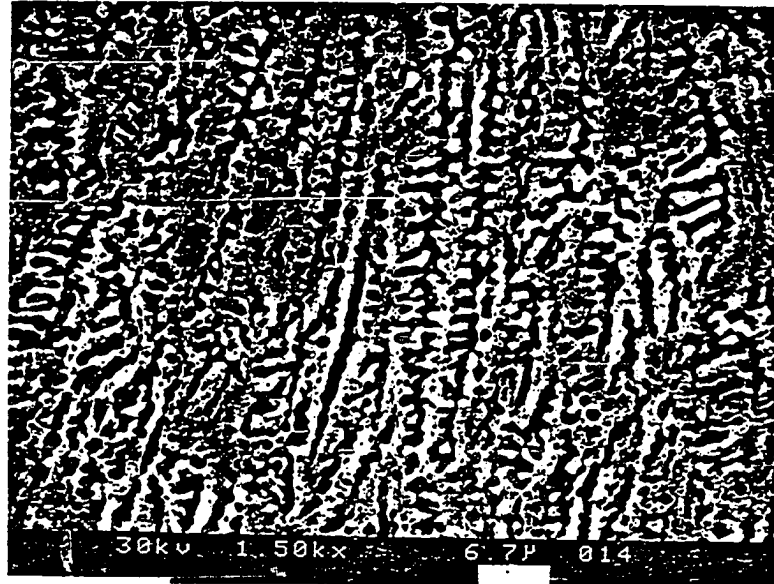


a) R=4.0 mm/sec.

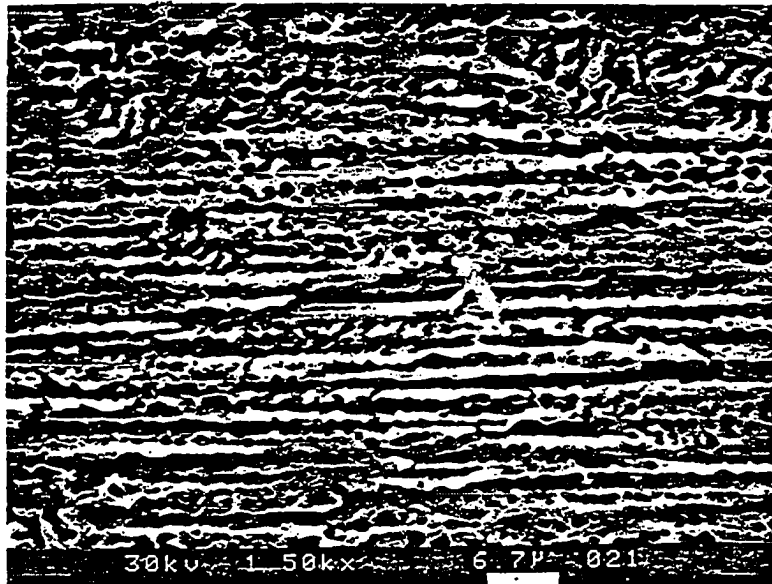


b) R=8.7 mm/sec.

Figure (29): Secondary dendrite arm spacings of 202 laser weldments decrease as solidification growth rate, R , increases.



c) R=18.1 mm/sec.

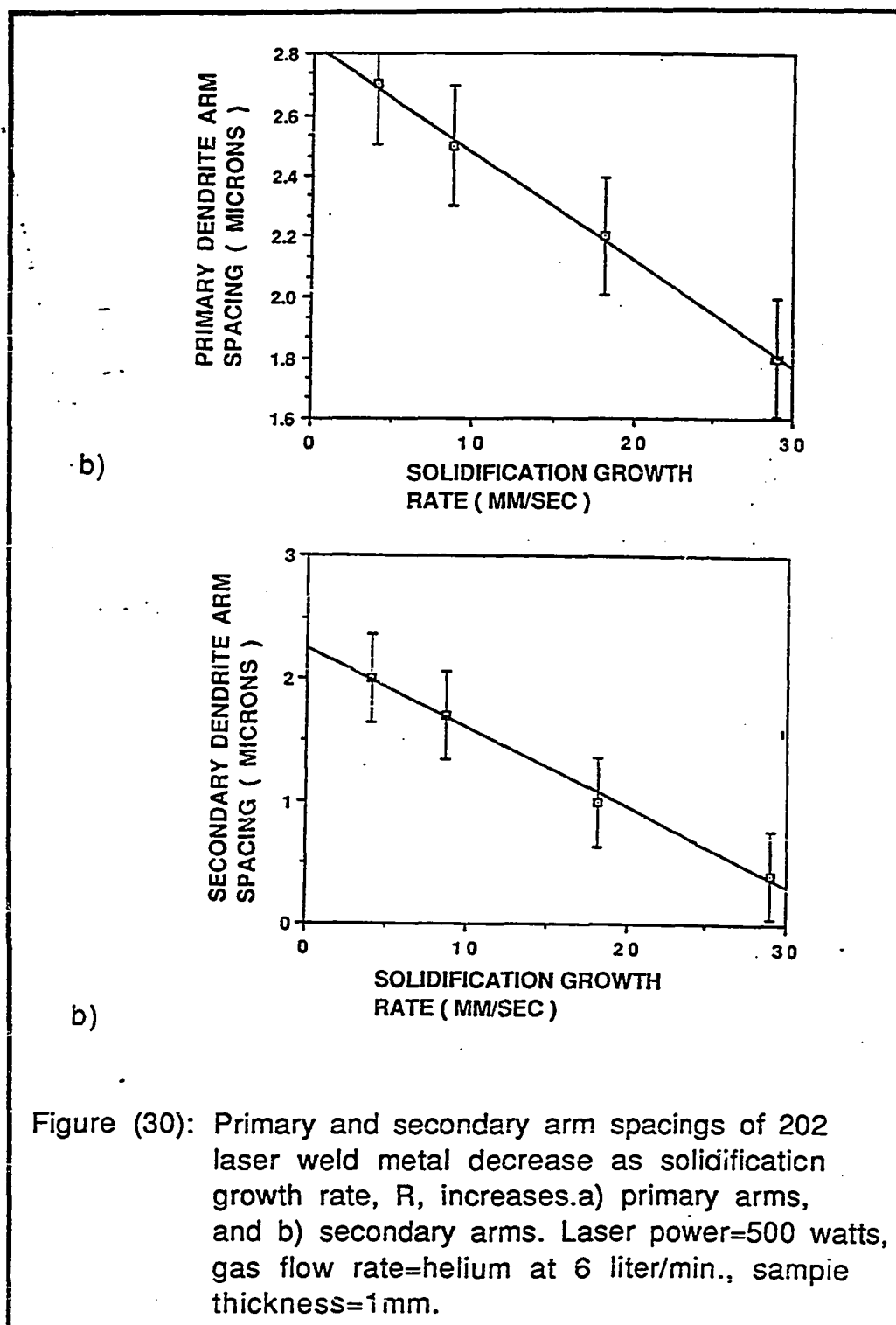


d) R=29 mm/sec.

Figure (29): (Continued)

Table (8): Primary and secondary dendrite arm spacings of 202 steel laser weld metal as a function of solidification growth rate (R). Laser power 500 watts, gas flow = helium at 6 liter/min., sample thickness =1 mm.

R mm/sec	PDAS μm	SDAS μm
4.0	2.7	2.0
8.7	2.5	1.7
18.1	2.2	1.0
29	1.8	0.4



solidification time upon the secondary dendrite arm spacing (SDAS), one may express the later as a function of time as following :

$$t \text{ (sec)} = \text{SDAS} / R \text{ (cm/cm/sec)} \dots\dots\dots 8$$

where R is the solidification rate, and t is the freezing time. Figure(31), where the data from figure 30-b is replotted against t, shows effect of freezing time on the secondary dendrite arm spacings (microns). The line drawn through the points is expressed by the following equation:

$$\text{SDAS} = 0.37 t^{0.47} \dots\dots\dots 9$$

4.2.3 Delta-Ferrite Content

Both the solidification mode and the solidification rate may affect the amount of ferrite retained. In laser welding, the melt solidifies with very high rates. Consequently, the austenitic stainless steel weld metal microstructure will contain a different amount of delta ferrite compared to weld metal solidified at slow rates.

Since R is one of the important factors which determines the presence and amounts of delta ferrite in the weld, the amount of ferrite has been counted in a number of welds solidified at different rates and plotted as function of R. Figures 32 and 33 illustrate the effect of R on ferrite content. As R increases, the amount of delta-

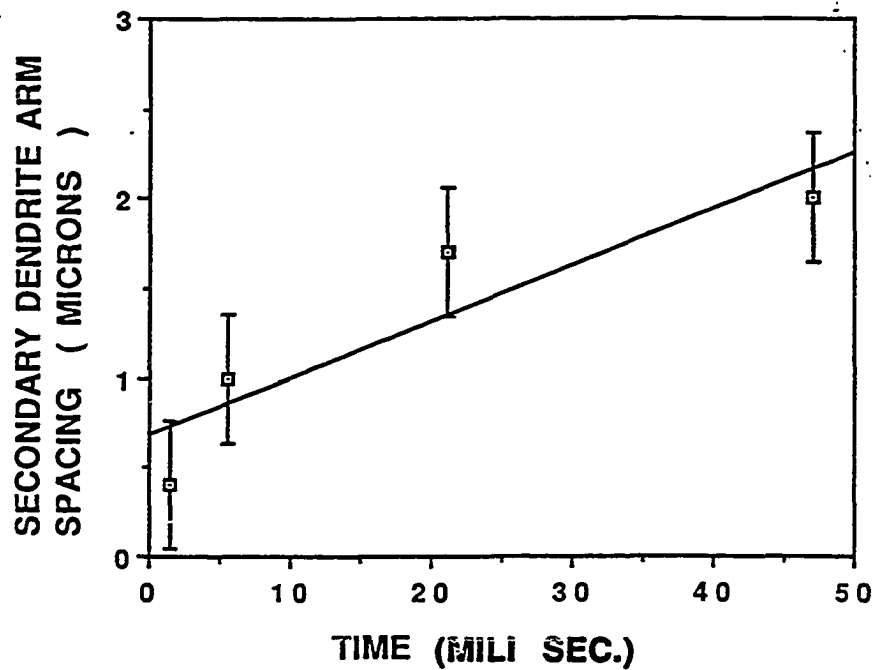


Figure (31): Secondary dendrite arm spacings of 202 laser weldment as a function of solidification time. Laser power = 500 watts, gas flow = helium at 6 liter/min, sample thickness = 1 mm.

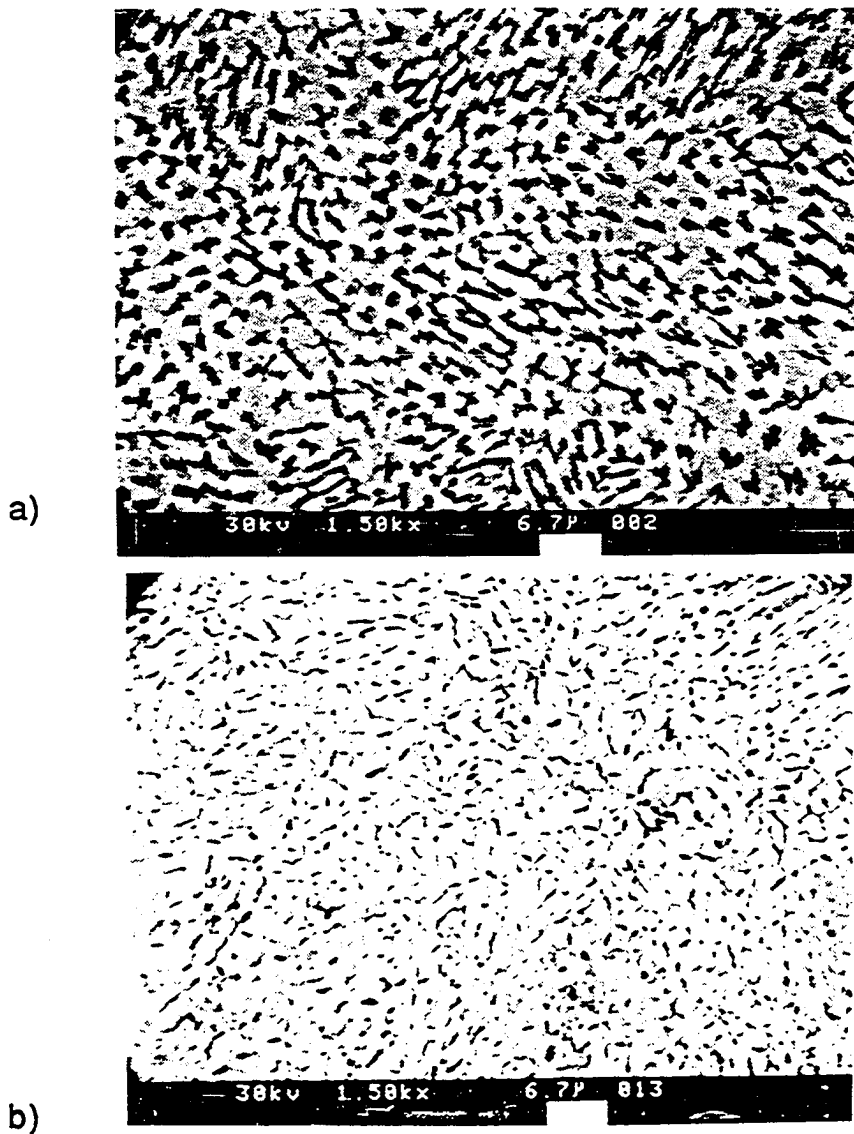


Figure (32): The laser weld metal delta-ferrite content of 202 laser weldment decreases as solidification growth rate increases.

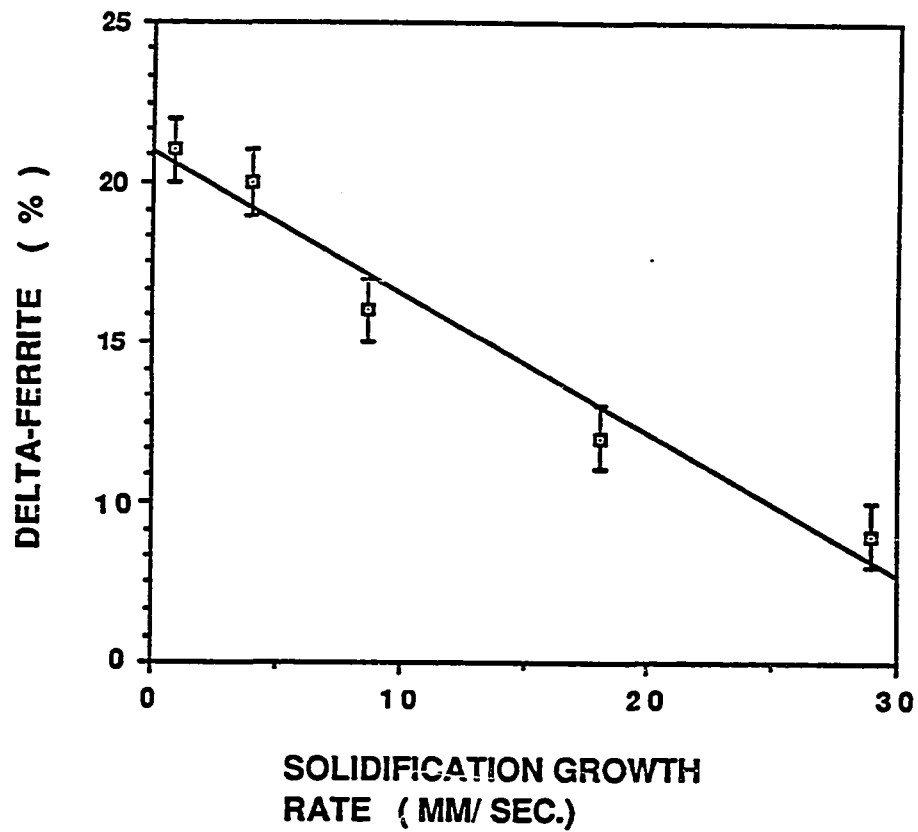


Figure (33): The laser weld metal delta-ferrite content of 202 laser weldments as a function of solidification growth rate. Laser power = 500 watts, gas flow = helium at 6 liter/min, sample thickness = 1 mm.

ferrite in the laser weld metal decreases. Consequently, the amount of the austenite phase will increase in the weld. This observation is directly opposed to that found in slow cooled samples, where the delta-ferrite content is found to be higher at high cooling rates. There are two reasons for decreasing ferrite, or increasing austenite, contents with increasing solidification rate. These are the solidification mode and degree of cooling. The solidification mode of the 200 stainless steel laser weld metal is found to be primary austenite, as will be explained in section 4.3.2. Figure 34 illustrates how the austenite content can be increased and the ferrite content decreased as R , or cooling rate, increases. The rapid solidification of the laser weld metal can result in undercooling the liquid to a lower temperature such as T_a in figure 34. The liquid starts to solidify at T_a , and the product of the weld metal likely to contain much more austenite than ferrite. If the solidification rate is sufficiently high to undercool the liquid to a lower temperature such as T_b , the solidified metal will have even more austenite than that solidified at T_a . Thus, from this diagram we expect to obtain only austenite if the liquid is further undercooled to lower temperatures such as T_c .

In previous work by David et al. on 308 stainless steel (56) and 202 stainless steel (57) a fully austenitic structure had been obtained when these steels were laser welded. Their welding speed was much higher than that used in this investigation. As a result of the high solidification rates encountered in their experiments the

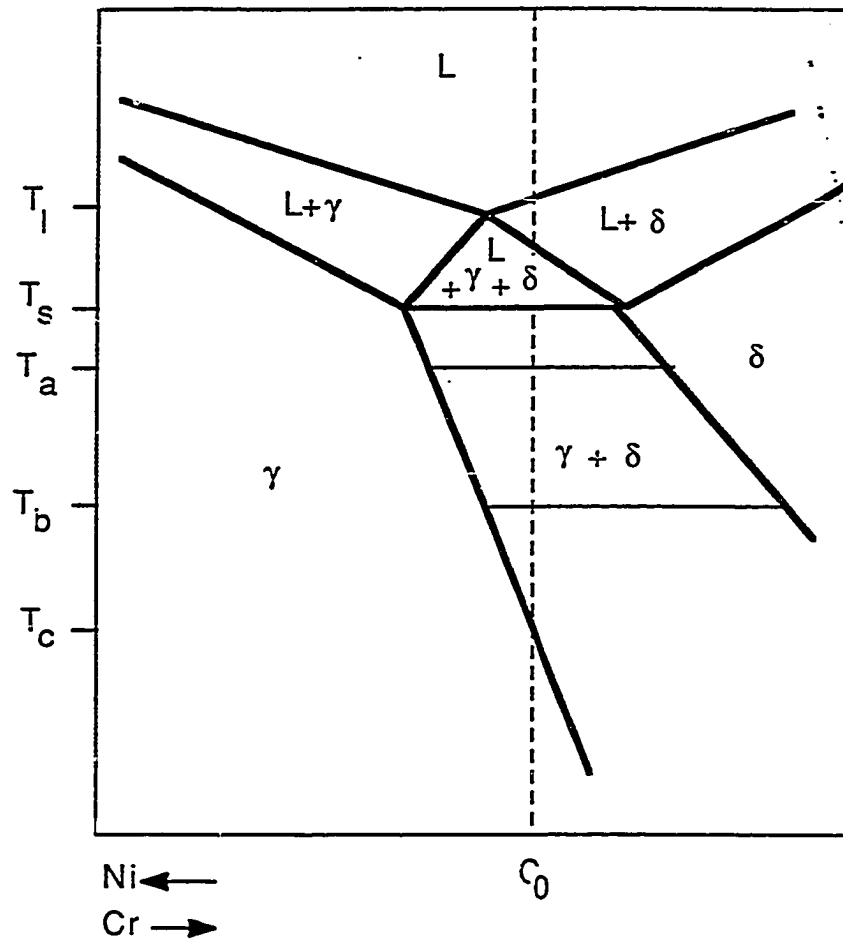
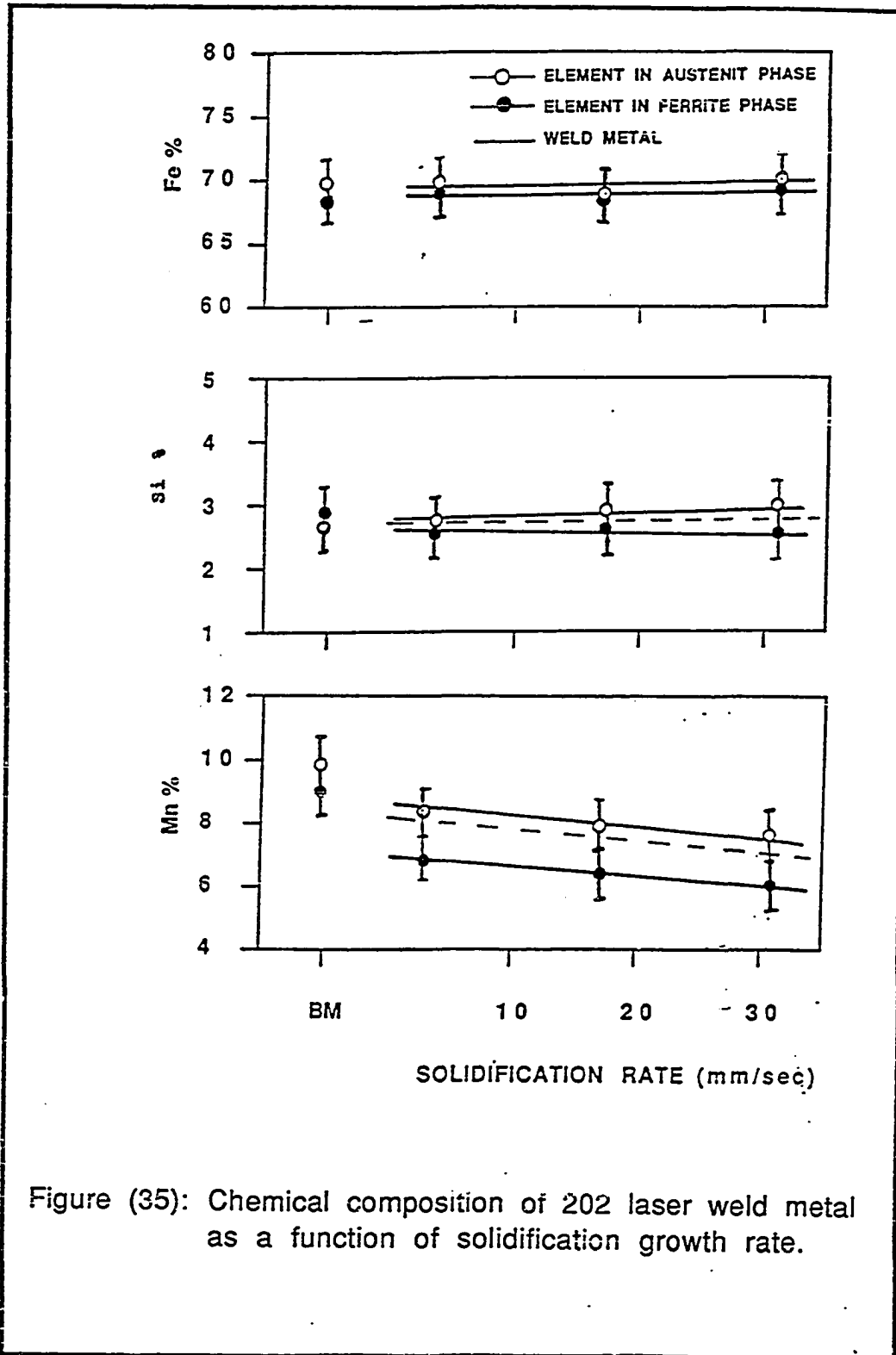


Figure (34): Amounts of austenite phase increase and of ferrite phase decrease as degree of undercooling increases.

liquid solidified within the austenite single phase region to produce a fully austenite weld metal structure.

4.2.4 Weld Metal Chemical Composition

Compositional analyses of the 202 stainless steel laser welds revealed that the austenite phase composition was almost constant for all the welds at approximately 3.85 pct Ni and 68.5 pct Fe. Generally, the changes in the concentrations of Fe, Ni and Si in the welds as a function of solidification rate are relatively small as can be seen from figure 35. However, a significant drop in manganese content from 8.50 to 6.56 is observed. This reduction in Mn content is found to increase as solidification rate increases. This is in agreement with the results obtained by DebRoy et al. (10,11,12) on 202 stainless steel laser welds. They attributed the high Mn loss at high scanning speeds to diminished obstruction of the beam energy by the metal vapor and the plasma, which resulted in relatively more exposure of the laser beam on the sample surface. Figure 35 also indicates some partitioning of Cr in the ferrite phase. The degree of partitioning varied, however, depending on the solidification rate. As solidification rate increased, the Cr enrichment in the ferrite was reduced. This observation is readily explained since the solidification time, which determines the degree of partitioning possible, varies inversely with solidification rate. Thus, as solidification rate increases, the possible degree of partitioning



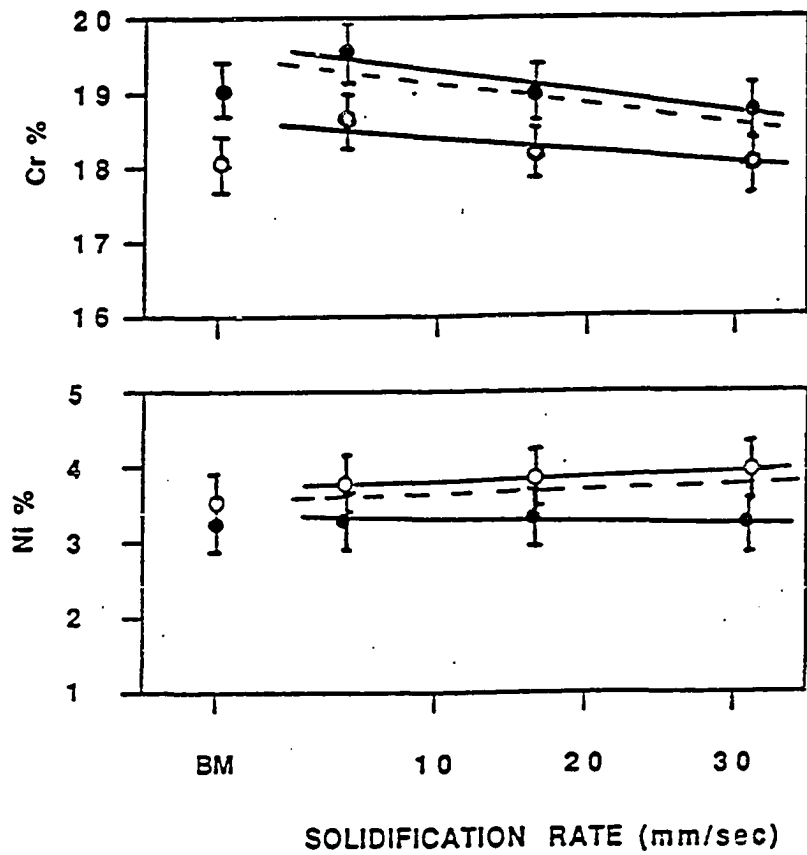


Figure (35): (Continued)

decreases. It should be mentioned that the width of the ferrite grain is normally 0.5 to 1.0 microns, which is about same or smaller than the diameter of the primary beam. It is therefore unlikely that depth profiles obtained by the x-ray analyzer would represent only the data from one grain of ferrite, especially if the beam is not in the center of the ferrite grain. To minimize the error, several readings from ferrite were taken.

4.3 Solidification Studies

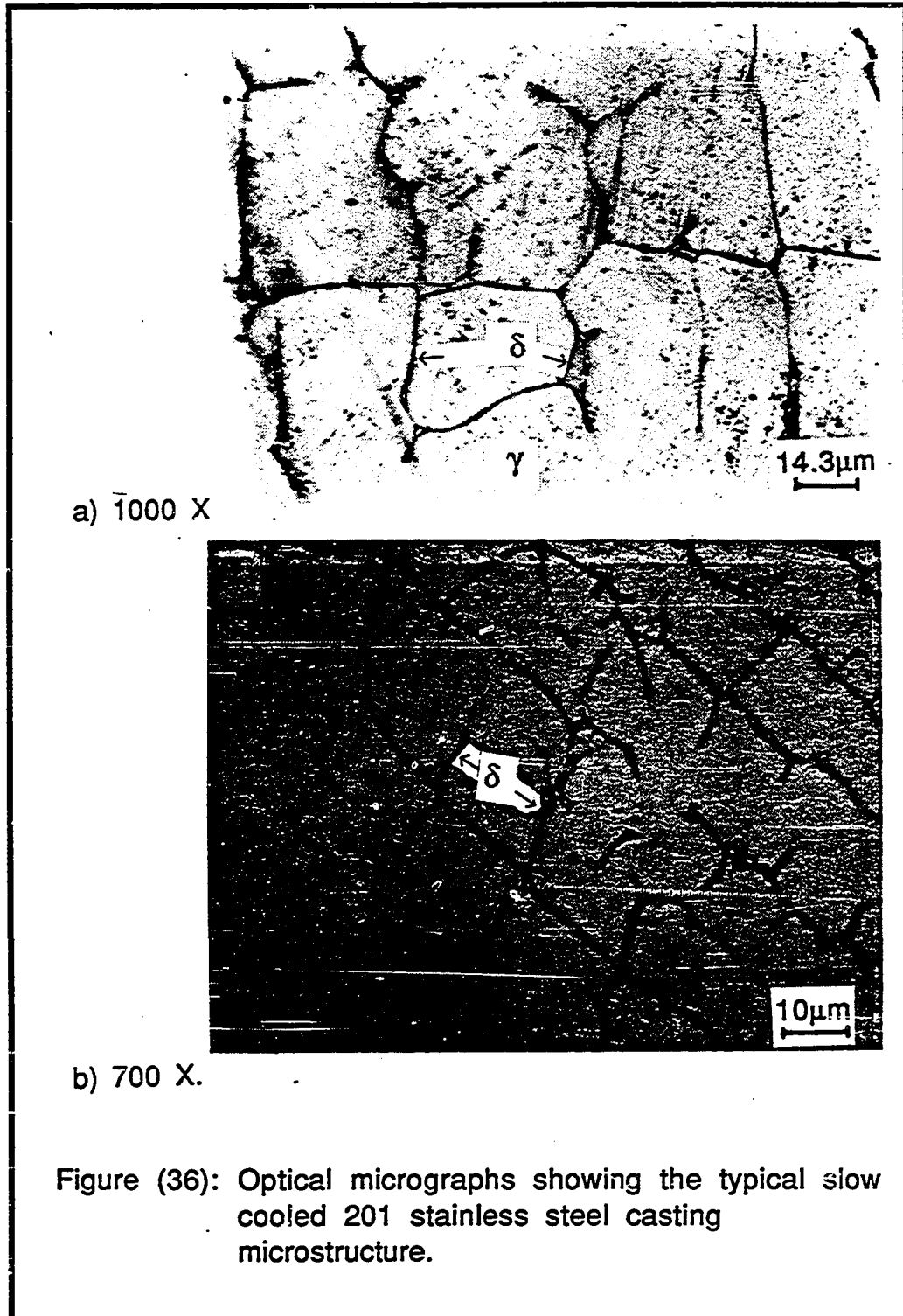
4.3.1 Microstructure Morphology and Solidification Mode of Slow Cooled 200 Stainless Steel

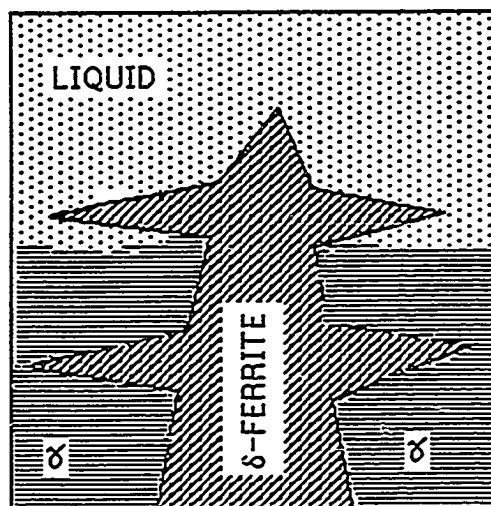
In order to study the effect of cooling rate on the structure and solidification behavior of austenitic stainless steel, type 201 steel samples were melted and solidified at 1, 45 and 100°C /sec. Optical microscopy and scanning electron microscopy were used to analyse the solidified structure.

4.3.1.1 Primary Delta-Ferrite Solidification

Figure 36 is an optical micrograph showing the slow cooled 202 stainless steel casting microstructure. To distinguish between austenite and ferrite, Kalling's reagent was used to etch the samples. This reagent attacks the ferrite phase which therefore appears darker than austenite. Figure 36 also shows that ferrite is located in the dendrite cores. This indicates that delta-ferrite is the first (primary) phase to solidify from the liquid.

Primary solidification of either ferrite or austenite is important in austenitic stainless steel. A number of investigators (42-46) have shown that when austenitic stainless steel solidifies as primary ferrite, the steel is more susceptible to hot cracking than if solidified as primary austenite. Solidification as primary





c) Schematic of solidification as primary delta-ferrite.

Figure (36): (Continued)

ferrite is schematically presented in figure 36-c, where delta-ferrite is located in the dendrite core, which is the first solid formed from the liquid during solidification.

This observation, primary ferrite solidification, is consistent with those found in other investigations (23, 33, 37, 40, 42, 43) which were performed on austenitic stainless steels. Previous work by Savage et al. (33) showed that solidification as primary ferrite results in Cr segregation at the spines of the ferrite dendrites. Thus, ferrite should have a higher Cr content than the austenite matrix when the liquid solidifies as primary ferrite. Results of chemical analyses of 202 stainless steel castings done in the present study showed that the average Cr content of the ferrite dendrites is higher than in the austenite. The amounts of Cr and other elements are given in table 9.

The primary ferrite solidification can be explained by using the diagram in figure 34, where 202 steel is superimposed. When 202 alloy cooled slowly enough from the liquid to room temperature, the solidification reaction can be described as follows :



where L, δ and γ represent liquid, ferrite and austenite, respectively. It is clear that delta-ferrite is the first solid to form from the liquid.

Table (9): Concentrations of various elements (Wt. %) in the base metal (BM), ferrite (δ) and austenite (γ) phases in the 202 steel laser weld metal. Laser power = 500 watts, welding speed =10 mm/sec., gas flow = helium at 6 liter min., sample thickness =1mm.

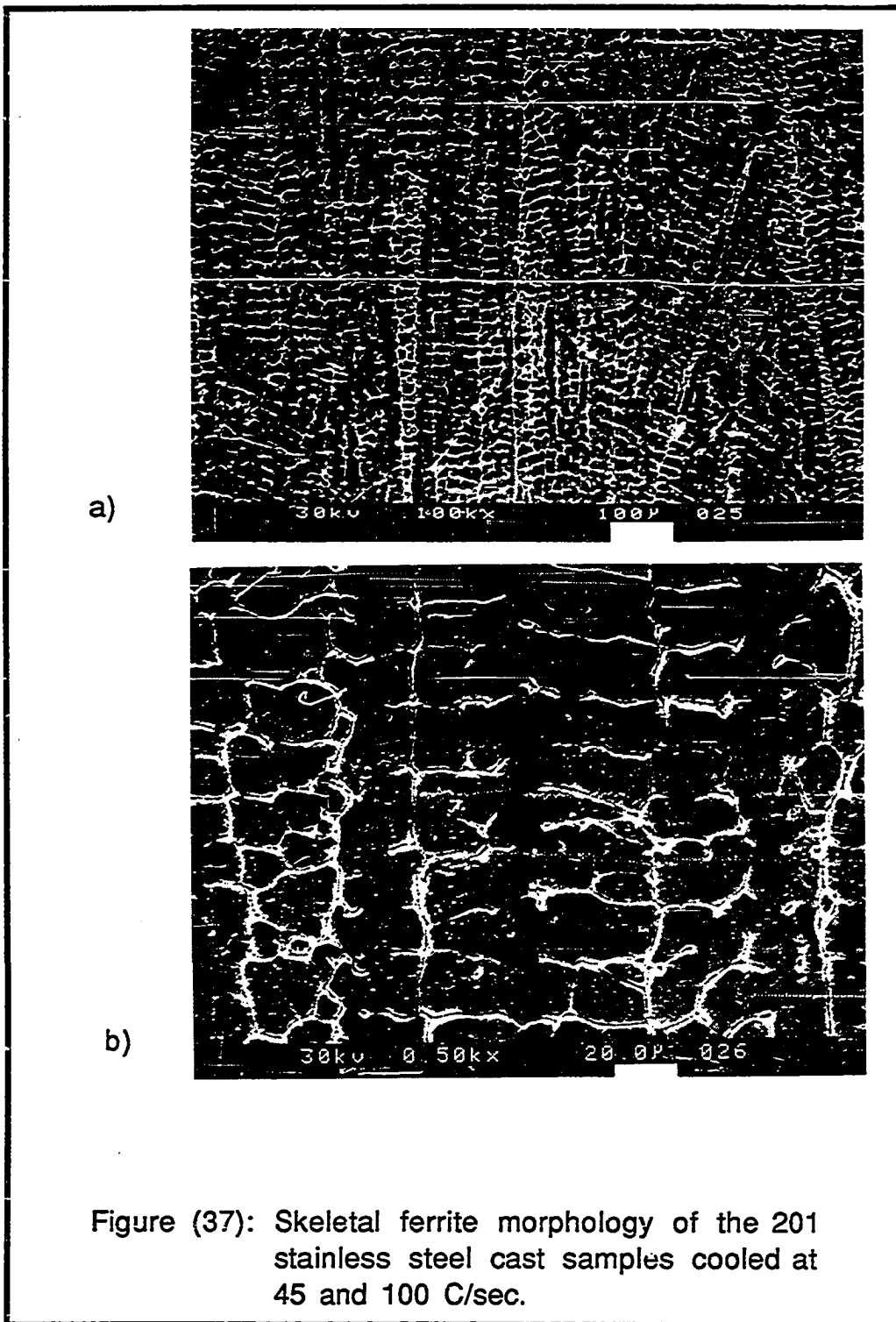
ELEMENT	IN	IN	
	BM	δ	γ
Cr	17.5	16.98	15.89
Ni	5.3	3.41	4.82
Mn	7.5	6.58	8.88
Si	1.0	0.77	0.97

4.3.1.2 Structure Morphology

The typical slow cooled 201 steel microstructure is shown in figure 37-a. The structure consist of ferrite dendrites in an austenite matrix. In figure 37-b, showing the dendrites at a higher magnification, primary dendrite columns with secondary branches and sometimes ternary branches can be seen.

The type of ferrite morphology seen in figure 37 is usually classified as skeletal (25,30), and is the one most commonly observed in austenitic stainless steel welds containing a duplex structure. In the present study this particular morphology was predominantly observed in all areas of the two 201 castings, cooled at 45 and 100 °C / sec, but only at the edges of the 201 cast which cooled at 1 °C / sec. Depending on the orientation of the cross-section, the ferrite could appear as an aligned skeletal network as shown in figure 37. The alignment is along the heat flow direction, which is also the primary dendrite growth direction. The ferrite is located within the cores of the primary and secondary dendrite arms and is the result of the incomplete primary delta to gamma transformation which will be discussed later.

At the center of the cast samples cooled at 1 °C /Sec the structure still consists of ferrite and austenite, but the ferrite morphology has been changed to lacy instead of skeletal. The lacy form of ferrite is shown in figure 38 and is characterized by its regularity and the ferrite is located within the cellular dendrites.



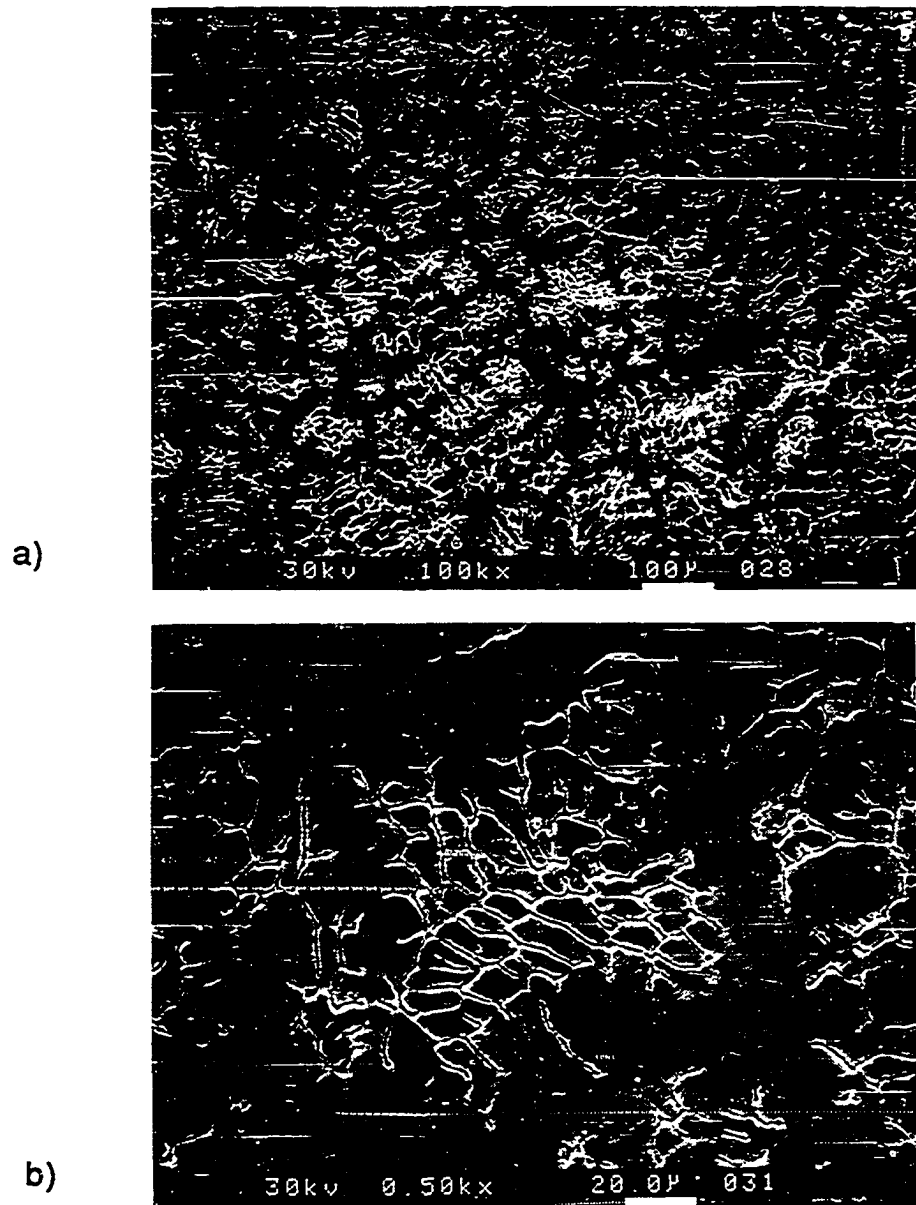


Figure (38): Lacy ferrite morphology at the center of the cast sample cooled at 1 C/sec.

The change in ferrite morphology can be mostly attributed to the change in local cooling rate from the edges to the center. At the edges, where the cast is close to the chill, the cooling rate is highest while at the center it is lowest. A high cooling rate favors a dendritic structure while a low cooling rate favors a cellular structure. The change in structural morphology from skeletal to lacy may be also attributed to the relatively high Cr content found at the center of the cast to that at the edges. Table 10 compares the Cr contents at these two regions. This explanation is supported by the schematic diagram of Suutala (figure 13) which relates the change in ferrite morphology from skeletal to lacy to the increase in Cr/Ni equivalent.

4.3.1.3 Solid-State Transformation of Delta-Ferrite to Austenite

The normal cast microstructure of 202 steel contains on the order of 8 - 20 volume percent delta-ferrite at room temperature (figure 39), despite the fact that immediately following solidification, the structure is almost completely composed of delta-ferrite. Studies by Matsuda et al. (24) indicated that at least 75 % of the final solidification structure of a type 304 stainless steel consisted of delta-ferrite, although after cooling to room temperature only about 10 to 20 volume percent ferrite was retained.

Table (10): Chromium and other element contents of the ferrite (δ) and austenite (γ) phases in the center and edge of the 201 stainless steel cast cooled at 45 °C/sec..

ELEMENT	FERRITE		AUSTENITE	
	center	edge	center	edge
Cr	16.98	16.64	15.89	15.47
Ni	3.41	3.43	4.82	4.08
Mn	6.58	7.76	8.88	7.10
Si	0.77	0.80	0.97	0.87

In figure 39, the delta-ferrite content for three cast samples cooled at different cooling rates is plotted as a function of the cooling rate. As the cooling rate decreases the delta-ferrite content of the casts decreases. The reason for this is that as cooling rate decreases, there will be more time for the delta to gamma transformation to occur. As a result of this, more ferrite (delta) will be consumed by austenite (gamma) resulting in smaller amounts of ferrite remaining in the cast structure. Thus, an extensive transformation of delta-ferrite to austenite must occur on slow cooling through the solidification range.

Inspection of the phase pseudo diagram in figure 34 indicates that an alloy of composition C_0 would begin to solidify as primary ferrite. At temperature T_a the alloy is in the two-phase austenite plus ferrite region. At this point, if equilibrium conditions hold, austenite begins to form from delta ferrite of composition C_0 . As the alloy cools under equilibrium conditions, the austenite which forms from the ferrite becomes progressively richer in chromium until the overall composition of the austenite is C_0 and the delta ferrite has been completely consumed.

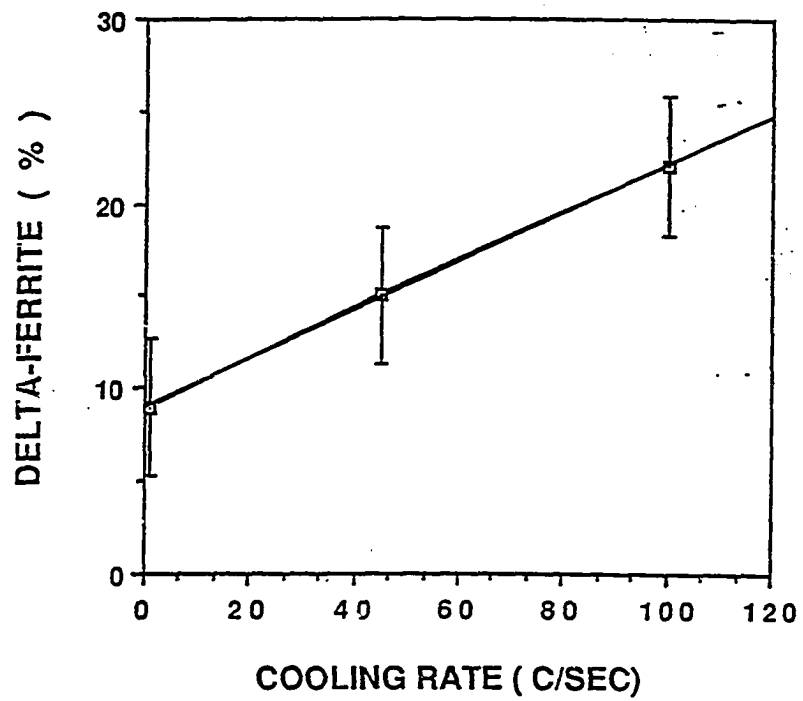


Figure (39): Amount of delta-ferrite of 201 stainless steel casts as a function of cooling rate.

4.3.1.4 Diffusion Controlled Mechanism in the Solidification of the Slow Cooled 201 Stainless Steel

In practice, the pseudo diagram predicts that the interval $T_S - T_C$ in figure 34 is of the order of 200 °C for the majority of austenitic stainless steel alloys which solidify as primary delta-ferrite (33). Since the cooling rates experienced in castings and in most conventional arc welding processes are usually in the range of 1 to 100 °C / sec., the alloy is present in the two-phase region approximately 2 to 200 seconds on cooling from the solidification range.

Diffusion data collected from the literature (58, 59) for chromium and nickel in austenitic stainless steels at elevated temperatures indicate that the diffusion rates of both elements support the possibility of a diffusion-controlled transformation of delta-ferrite to austenite in the presence of slow cooling rates. The diffusion coefficients and rates for Cr and Ni in austenitic stainless steel are given for a series of temperatures in table 11. In addition, the average diffusion distance, x , is calculated for both species within the indicated temperature interval. The average diffusion distance is defined as:

$$x = 2 \sqrt{Dt}$$

where D is the average diffusion coefficient in the temperature interval, and t the corresponding time, assuming a uniform cooling rate.

Table (11): Diffusion rates and diffusion distances (μm) of the Cr and Ni in austenitic stainless steel.

TEMPERATURE $^{\circ}\text{C}$	D_{Cr} cm^2/sec	$X_{\text{Cr}} (\mu\text{m})$				
		1	45	100		
		$^{\circ}\text{C}/\text{sec}$				
1400	1.8×10^{-9}	}	9.6	1.40	0.70	
1300	5×10^{-10}		5.2	0.73	0.40	
1200	1.7×10^{-10}		}	2.9	0.41	0.29
1100	3.9×10^{-11}					

TEMPERATURE $^{\circ}\text{C}$	D_{Ni} cm^2/sec	$X_{\text{Ni}} (\mu\text{m})$				
		1	45	100		
		C/sec				
1400	1.3×10^{-10}	}	3.13	0.44	0.22	
1300	4.1×10^{-11}		1.40	0.20	0.10	
1200	1.1×10^{-11}		}	0.73	0.10	0.05
1100	2.5×10^{-12}					

Table 11 indicates that on cooling from 1400 °C to 1300 °C a Cr atom diffuses an average of 9.6 microns while a Ni atom which must diffuse in the opposite direction, moves only 3.13 microns. At lower temperatures, diffusion becomes more difficult for both species. Since the typical primary delta-ferrite dendrites are on the order 1 to 5 microns in diameter, the diffusion rate calculated above would be sufficient to redistribute the solute in a diffusion-controlled reaction under low cooling rates.

4.3.2 Microstructure and Solidification Mode of 200 Stainless Steel Laser Weld Metal

4.3.2.1 Fusion Zone and Heat Affected Zone Microstructures and the Mode of Solidification

The typical microstructure of the laser welds is shown in figure 40. The weld metal contained an austenite and ferrite duplex ($\delta + \gamma$) microstructure. Depending on cooling rate, the delta ferrite percent varied from 8 % in high cooling rate samples to 20 % in low cooling rate samples. This delta-ferrite is formed at the grain boundaries during primary austenite solidification and represents the retained delta-ferrite observed in the laser weld metal microstructure. The presence of delta-ferrite in the laser weld metal was confirmed both by etching techniques and electron diffraction patterns using

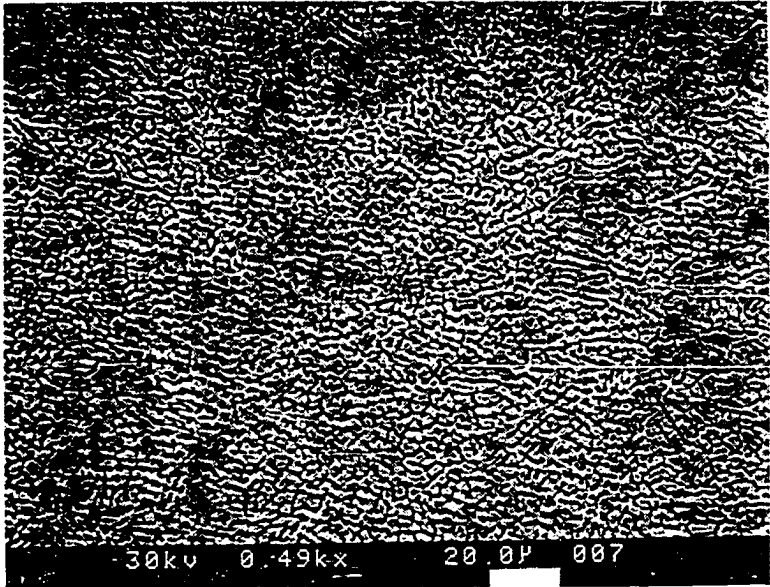


Figure (40): Typical microstructure of 202 laser weld metal.

TEM. Kalling's reagent was used for the etching because it rapidly attacks delta-ferrite leaving austenite unattacked. Figure 41 is an SEM micrograph of laser weld metal shows columns of austenite dendrites (light etch) left unattacked on the surface as a three-dimensional network. The ferrite, which is interlocked between the austenite dendrites, is attacked by the etchant so that it appears dark in the micrograph. TEM is used to identify the phases present in the weld. Figure 42 is a TEM micrograph showing delta-ferrite rims between austenite dendrites, while figures 43 a and b show the bright and dark field images taken from the ferrite rims, and figures 43 c and d are the electron diffraction patterns taken from the ferrite and austenite respectively.

A close examination of the laser weld microstructure has been made using TEM. A significant number of dislocations within the austenite dendrites was evident. These are possibly due to the thermal stress caused by the rapid cooling during laser welding. Also, the austenite dendrites contain a number of stacking faults. These stacking faults may be produced by the rapid freezing which disturbs the growth of the crystalline structure during solidification resulting in a new atom layer being formed in an incorrect sequence. Figure 44 is a TEM micrograph showing a number of dislocations and stacking faults in two austenite dendrites.

The microstructural difference between the base metal (BM) and heat affected zone (HAZ) was studied using optical and scanning electron microscopy. Figure 45 is an optical micrograph of a

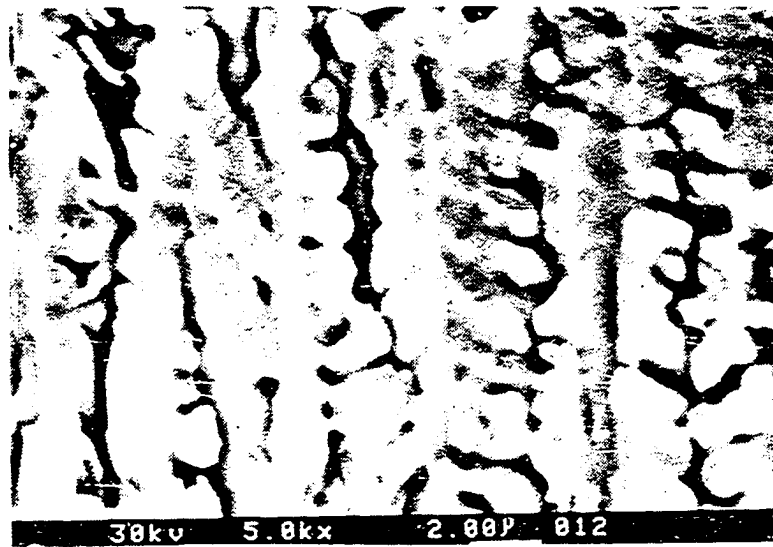


Figure (41): Columns of austenite dendrites are left on the surface unattacked as three-dimension network.

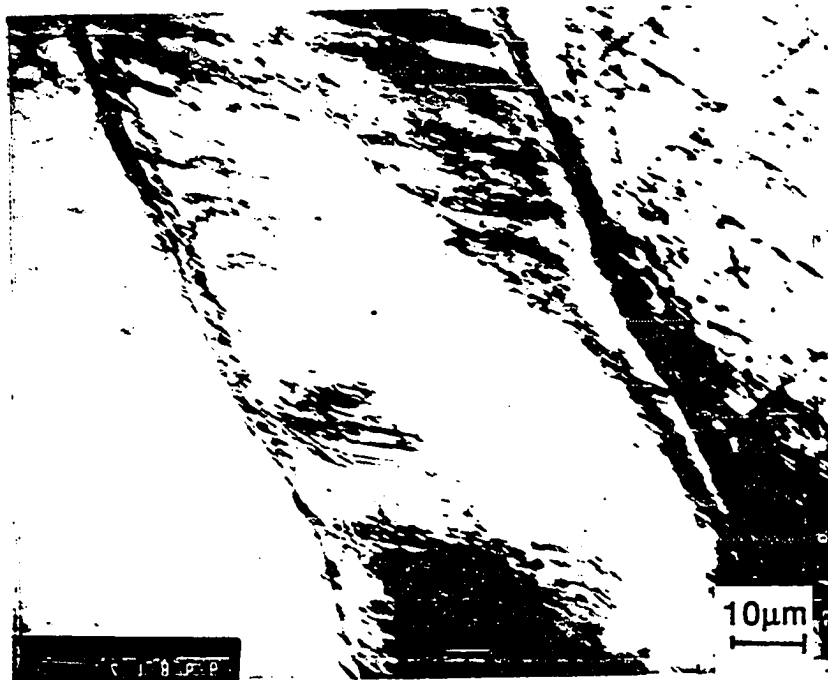


Figure (42): TEM micrograph of 202 laser weldment showing delta-ferrite rims between austenite dendrites.

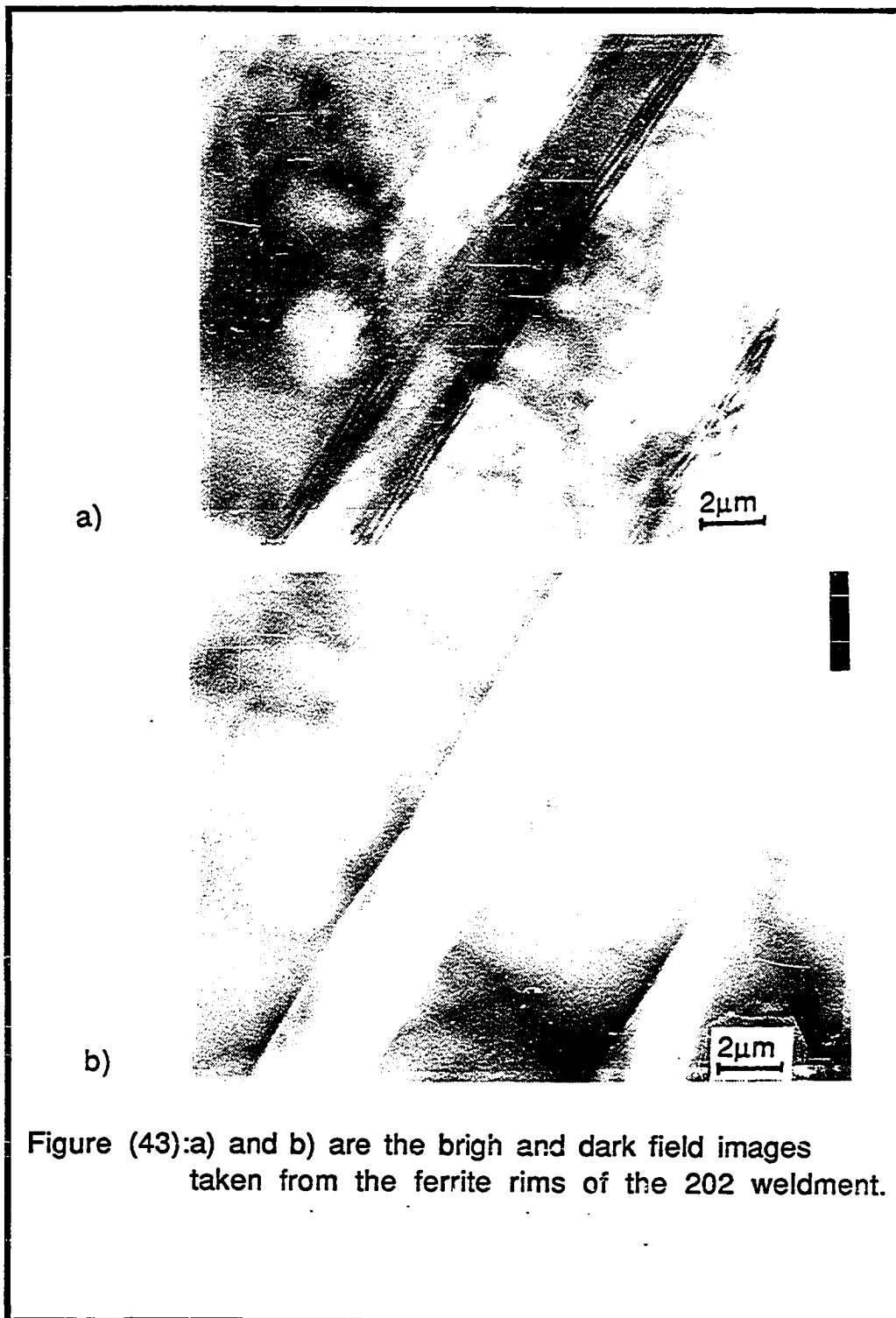
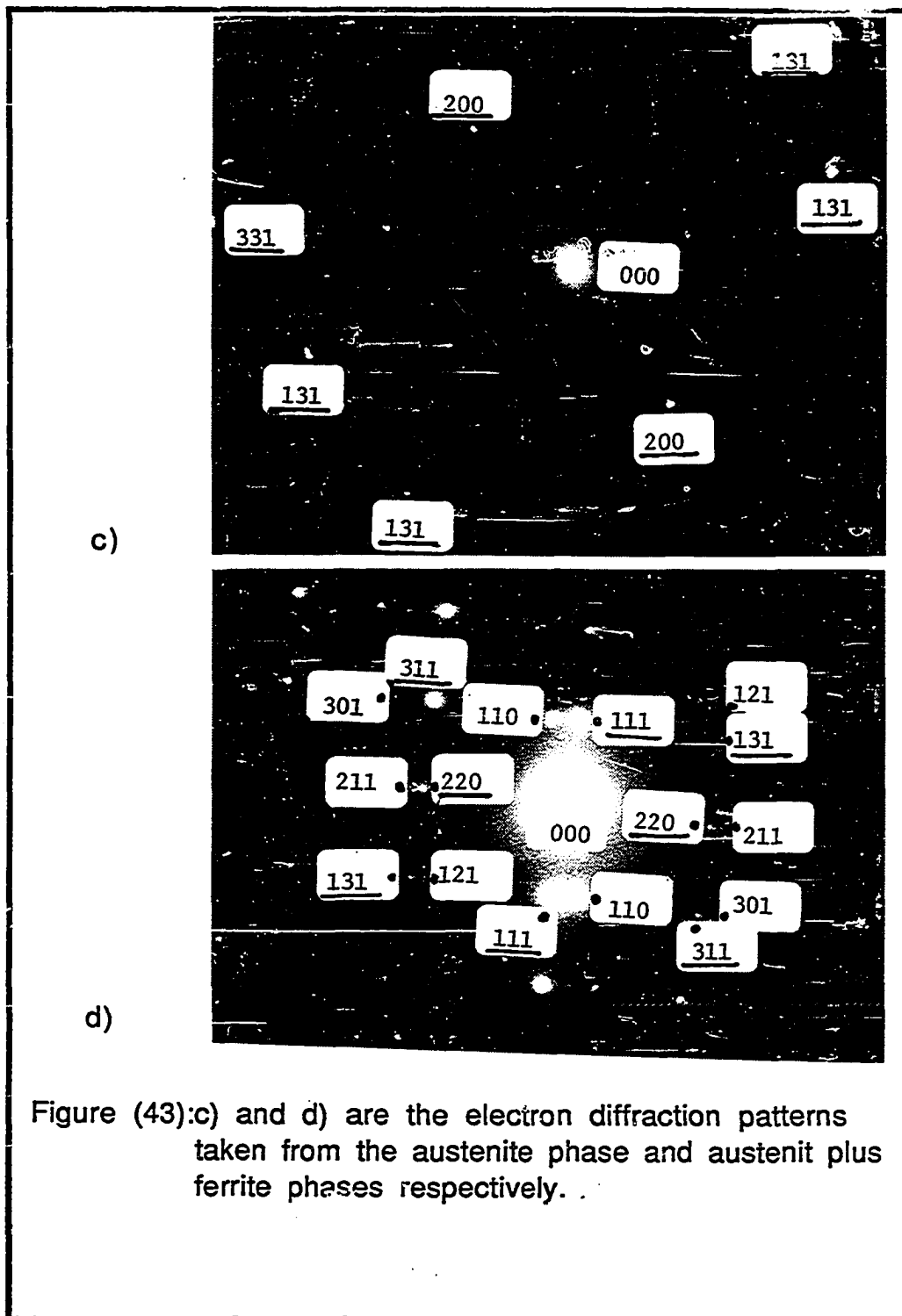


Figure (43):a) and b) are the bright and dark field images taken from the ferrite rims of the 202 weldment.



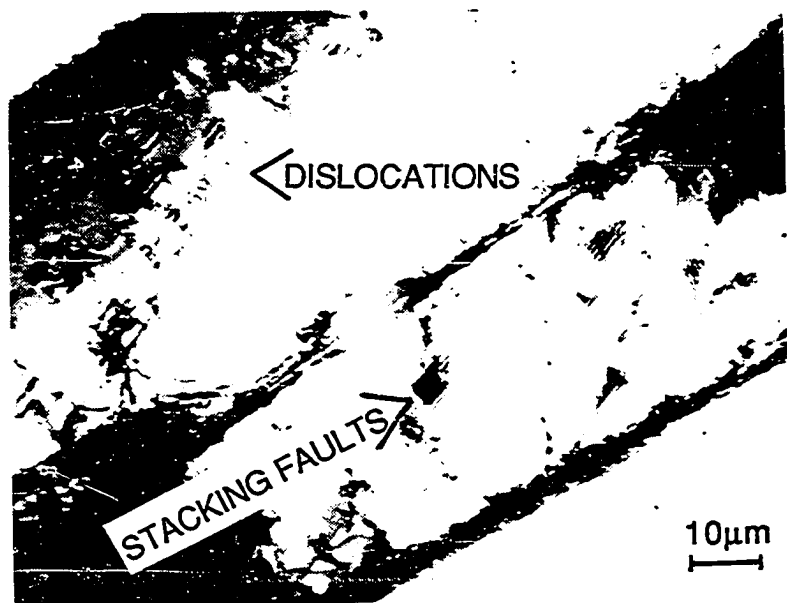


Figure (44):TEM micrograph showing number of dislocations and stacking faults in two austenite dendrites of the 202 weldment.

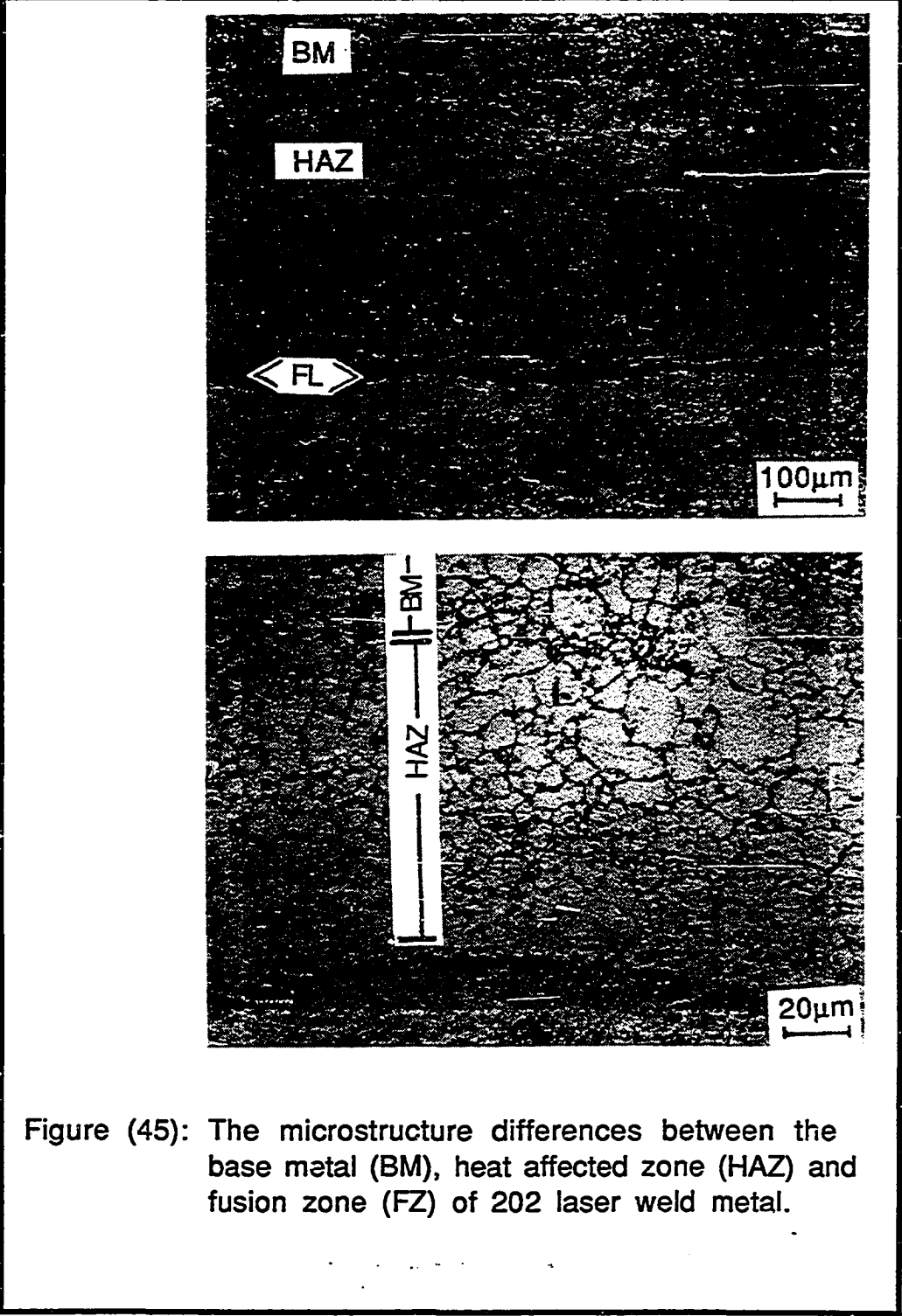


Figure (45): The microstructure differences between the base metal (BM), heat affected zone (HAZ) and fusion zone (FZ) of 202 laser weld metal.

longitudinal section of the laser welded specimens and shows the transition in microstructure from the fusion zone to the base metal. Several distinct zones are visible. The first zone after the fusion zone is a thin layer which is approximately 12 microns wide usually known as the unmixed zone or fusion line (FL). In this layer delta-ferrite is present in great amounts as shown in figure 45. The reason for this is the compositional gradient which must exist between the unmixed zone at the base metal and the portion of the fusion zone. Rapid quenching experiments performed by Lippold et al. (34, 60) and Arata et al. (61) on type 310 stainless steel indicate that chromium and nickel are rejected to the liquid during primary austenite solidification. Both studies show that Cr segregates more than Ni. The rapidly segregated Cr is seized by the unmixed base metal to accumulate at the thin layer adjacent to base metal. As a result the remaining liquid in this layer is rich in Cr which is a strong ferrite stabilizer.

Traversing into the base metal, the next zone is the HAZ. It is approximately 0.0125 mm wide and characterized by large grains of austenite with an average diameter of 20 microns surrounded by delta-ferrite. The HAZ is a region of base metal adjacent to the weld which is only affected by heat but is not melted. Therefore, it reaches a temperature close to the melting point of the alloy and as a result experiences a number of microstructural changes. This has been known as a factor in determining an alloy's susceptibility to corrosion, cold cracking and reheat cracking in welds. Thus, the

smaller the HAZ the less the chance of the weld exhibiting these undesired properties. The size of the HAZ in stainless steel welds produced by a laser is much smaller than those produced by arc welding processes. The narrow HAZ would generally result in good properties in many metals and alloys, and thereby this should be regarded as an advantage of laser welding.

Next to the HAZ come the base metal which has an average grain diameter of 10 microns.

4.3.2.2 Critical Cooling Rate

A study of the effect of the cooling rate on the solidification behavior of 201 and 202 stainless steels indicates that there is a critical cooling rate within the 100- 1000 °C /sec range, below or above which the solidification mode varies dramatically. This observation is demonstrated in figure 46, where solidification mode/ ferrite content is plotted versus cooling rate. This figure shows two straight lines, one for primary ferrite and the other one for primary austenite. The point where the extension of these lines meets roughly indicates the critical cooling rate. Below this critical cooling rate the mode of solidification of 201 and 202 stainless steels is primary ferrite, above it the mode changes to primary austenite.

The observation of a critical cooling rate in austenitic stainless steels, such as 201 and 202, is supported by previous work by

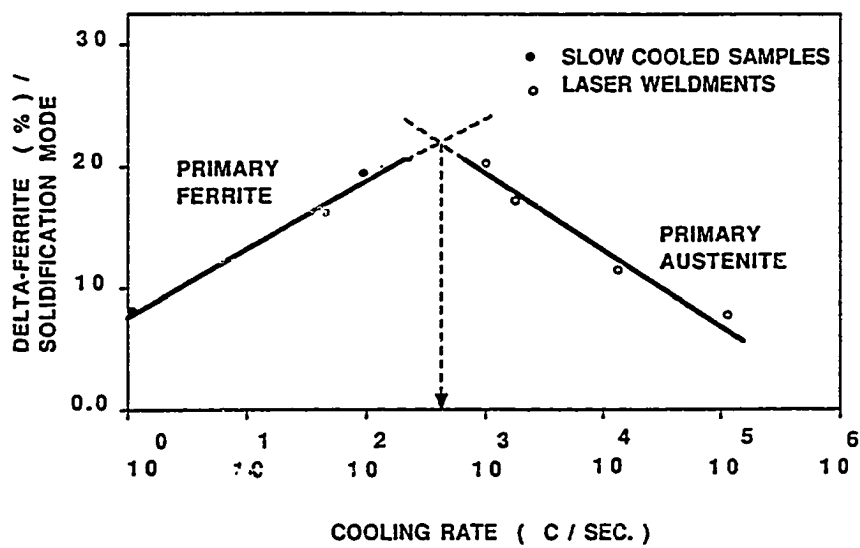


Figure (46): A plot indicating a critical cooling rate at which the solidification modes of 201 and 202 stainless steel laser weld metal vary dramatically.

Weatherly et al. (40). They studied the structure of 20-10 stainless steels by varying the cooling rates. At a low cooling rate of 20 °C/sec a duplex structure consisting of primary ferrite plus austenite is formed. At a cooling rate of 100 °C/Sec, the structure was finer than but similar to that formed at 20 °C/sec. At somewhat higher cooling rates than 100 °C/sec, the mode of solidification is changed to produce primary austenite. The structure consists of massive austenite grains bounded by rims of retained ferrite (figure 18).

4.3.2.3 Proposed Mechanism For Primary Austenite Solidification During Laser Welding

As mentioned in the literature review section, Lippold and Savage (39) observed a massive-structure of primary austenite formed during the solidification of some types of austenitic stainless steel welds. This massive structure consists of large blocky austenite grains surrounded by ferrite rims. Because the chemical compositions of the product structures were found to be similar to that of the parent metal, and because the structure has massive grains, they postulated a massive-transformation reaction as a mechanism. On the other hand, Savage (43) and Fredriksson (53) have related the change in solidification mode to the change in chemical composition of the welds from those of "ferritizers" to "austenitizers" such as Ni, Mn and N.

Comparing the structure of primary austenite solidification obtained by the laser welding of 200 stainless steels in this study to those obtained in the above mentioned investigations, the structure exhibits none of the blocky (massive) grains. Also, the laser weld structure exhibits none of the angular facets which usually would be expected with a massive transformation. The laser weld metal microstructure simply consists of fine dendrite columns with no angular facets. Moreover, results of chemical analyses showed a difference in composition between the product and the parent structure. Thus, the massive-transformation mechanism can not be a mechanism for the formation of the structures present in the 200 stainless steel laser welds.

The conclusion of Savage and Suutala that the enrichment of the weld metal by austenite stabilizers such as N, Mn and Ni is responsible for altering the solidification mode is also unlikely to apply to the present case. Microchemical analyses of these elements in the 201 and 202 stainless steel laser welds in this study and other studies (10, 11, 12) showed a significant reduction in concentrations of these elements, especially Mn, caused by evaporation during laser welding. In addition, the Mn and Si contents of the 200 stainless steels were such as to have nearly equal and opposite effects on the stabilities of ferrite and austenite, respectively, and so should not significantly influence the solidification behavior. According to Suutala (62), Mn in austenitic stainless steels at concentrations of 5 to 8 pct (such as in 200

stainless steels) behaves almost as a " ferritizer ", or at least its austenite-favoring effect on the solidification mode is insignificant. Also, according to Guiraldeng (63), Mn has a very low nickel equivalent effect when Ni is present in the alloy (Ni % in 200 stainless steel \approx 4-5 pct), whereas without Ni it has a real ferritic effect, which increases with temperature. Nitrogen and carbon are indisputable austenitizers, but their relative austenite-favoring effect increases with decreasing temperature. This can be taken as supporting the early finding of the solid-state transformation of $\delta \rightarrow \gamma$ at low temperatures in the slow cooled samples. The effect of N and C in altering the solidification mode in the laser weldments was not considered.

Therefore, another mechanism rather than massive-transformation or austenite stabilizers must be responsible for altering the solidification mode of 200 stainless steel laser welds.

THE UNDERCOOLING CONCEPT

According to theory, when a liquid is undercooled a large amount, other crystal phases may become thermodynamically viable. If the activation barrier for nucleation of these alternative crystallization phases becomes less than that of the primary crystallization phase, then the alternative phase may nucleate.

In the case of the 201 and 202 stainless steels the equilibrium mode of solidification is one of primary ferrite. However, with

sufficient undercooling on the order of 70°C , the liquid can be brought to the two-phase ferrite-plus-austenite region. While with a larger undercooling of about 200°C , the liquid can be brought to the single-phase austenite region. Such a level of undercooling can be readily attained by many rapid solidification processes such as splat quenching, vacuum and centrifugal atomization, differential thermal analysis (DTA) and laser and electron beam welding processes. Table 12 shows the degree of undercooling achieved in many alloys with various processes. The table shows that undercooling of up to 475°C can be attained in type 316 stainless steel using DTA. In the case of 200 stainless steels, if the liquid is brought to the single phase austenite region by sufficient undercooling, it will solidify as austenite with no alternative. But if it is brought to the two-phase region ($\delta + \gamma$), competition between austenite and ferrite solidification must exist. Kelly et al. (64) found that in the larger solidification volumes of large powder particles of 303 stainless steel, austenite solidification dominated, whereas in smaller sizes powders, ferrite solidification was found. Flemings et al. (65) mentioned that the same phenomenon has also been obtained in 316 austenitic stainless steel.

Thermodynamic calculations were performed by Flemings (65) on 316 steel and by Kelly (64) on 303 steel to find the free energies of liquid-to-FCC (austenite) transformation and the liquid-to-BCC (ferrite) transformation as a function of undercooling. Results of these calculations are plotted in figure 47. This indicates that if the

Table (12): Degree of undercooling achieved
in many alloys with various
processes.

ALLOY	ΔT	REFERENCES
Fe-25 Ni	200, 235,300	65
Fe-25 Ni-0.3 S	190,225	65
Ni-2 Ag	205	65
AISI 4330	165, 200	65
440C	150	65
316 Stainless	475	65

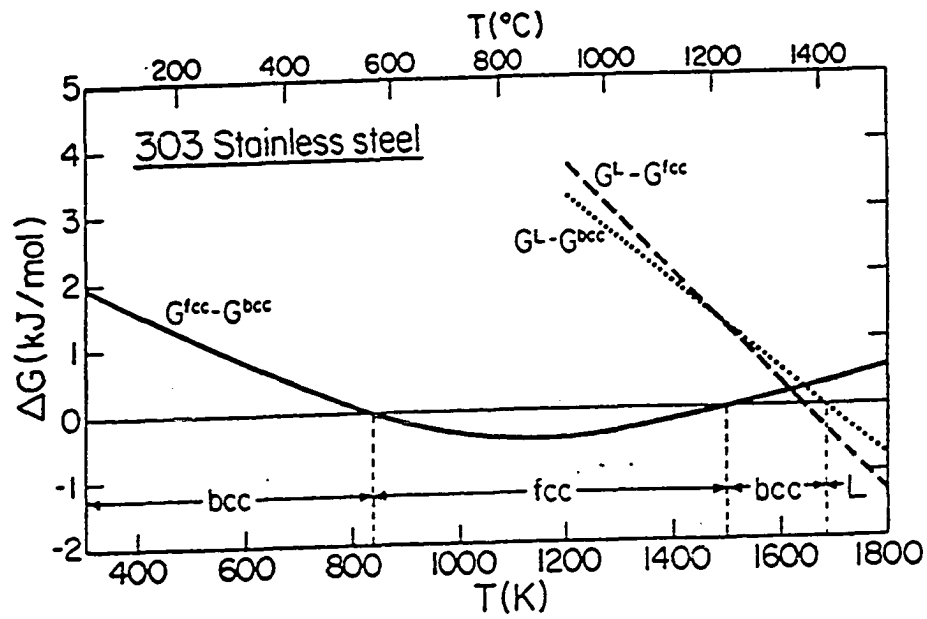


Figure (47): The relative thermal stabilities of the liquid, FCC, and BCC phases. The more stable phase, at a given temperature, is indicated (64).

liquid is undercooled up to 200°C it will solidify as FCC. This degree of undercooling can be easily achieved in many alloys by many of rapid solidification processes as shown in table 12. Since the laser welding process is one of the rapid solidification processes it is, therefore, possible to obtain this degree of undercooling. Although their analyses were for types 303 and 316 austenitic stainless steels, it is possible that the same conclusions may be applicable to austenitic stainless steels in general, and to 201 and 202 stainless steels in particular, since these types of steels are counterparts of 303 steels and have almost the same Cr/Ni equivalent ratios (≈ 1.6 for 303 and 1.5 for 201). Kelly et al. showed that austenite solidification is also favored kinetically over ferrite solidification. They found that in the presence of heterogeneous nucleation sites, such as in the larger volumes of large powder particles (≈ 10 gm of 303 steel), austenite solidification dominated whereas in very small isolated particles (≤ 70 μm diameter), ferrite solidification was found. The change in solidification mode was attributed to the preferred austenite formation at heterogeneous nucleation sites which were readily available in the larger volumes. In the present study, with the considerably larger solidification volumes of the laser weld pool, an abundant supply of heterogeneous nucleation sites can be expected to exist, resulting in preferred austenite solidification.

In summary, it is thought that undercooling before solidification adjusts the relative thermodynamic and kinetic factors involved in

the nucleation rates of the two phases, thus allowing for a competitive nucleation process. In the present study, the liquid of the 201 or 202 steel is sufficiently undercooled during laser welding to the point where austenite phase solidification is more favorable thermodynamically and kinetically than ferrite phase solidification.

Chapter 5

CONCLUSIONS

- 1) An equation relating the cooling rate of laser weld metal to secondary dendrite arm spacing has been empirically determined. Using this equation, the cooling rate of 201 and 202 stainless steel laser weld metal is estimated as 10^3 °C/sec. for low solidification rates and 10^5 °C/sec. for high cooling rates. The cooling rates estimated by this method were found to be consistent with those determined by the product of solidification growth rate and temperature gradient and the three-dimension Lancaster formula.

The following conclusions pertain to the results of the solidification studies of 200-series stainless steel:

- 2) The solidification phenomenon in laser welds does not correspond well with those in castings with respect to solidification mode and structural features.
 - a) At slow cooling rates, such as in casting experiments, the solidification mode is found to

be primary ferrite as is expected from the constituent diagram.

- b) At rapid cooling rates, such as experienced in laser welding, the mode of solidification is altered from primary ferrite to primary austenite.
- 3) The change in solidification mode was related to the excessive undercooling caused by rapid cooling during solidification of the weld metal. Moreover, it was shown that austenite solidification is more favorable thermodynamically and kinetically than ferrite solidification.
 - 4) A critical cooling rate was observed at which the solidification mode is abruptly changed. This critical cooling rate lies within the cooling range of 10^2 - 10^3 °C/sec., below which the alloy solidifies as primary ferrite, and above which it solidifies as primary austenite.
 - 5) It was observed that ferrite is present in different amounts and shapes depending on the degree of cooling and mode of solidification.
 - a) The results indicated that a solid-state transformation of delta to gamma occurs in slow cooled stainless steel samples. This transformation is diffusion controlled and

increases as cooling rate decreases. This leads to more delta ferrite being consumed by the austenite, resulting in smaller amounts of ferrite present in the structure.

b) The high-Cr ferrite formed at the grain boundaries during primary austenite solidification remains stable to room temperature and represents the retained delta-ferrite observed in the laser weld microstructure. The amounts of this retained delta-ferrite were found to be larger at lower cooling rates.

c) A lacy morphology of delta ferrite was observed in the very slow cooled sample, while a vermicular morphology was observed in samples having relatively higher cooling rates.

6) The following conclusions pertain to the influence of solidification growth rate, R , on the nature and features of the laser weld metal microstructure:

a) Austenite content increases as solidification rate increases.

b) Primary and secondary dendrite arm spacings decrease with increasing solidification rate.

- c) At constant welding power, an increasing in solidification rate decreases heat affected zone size, and depth and width of the welds.
- d) The degree of partitioning for Cr and Ni in the ferrite phase is reduced with increasing solidification growth rate.

REFERENCES

- 1) Kujanpaa, V. P., David S. A. and White, C. I., *Welding Res. Supp.*, p. 203-s, Aug. 1986,
- 2) Rutter, J. W. and Chalmers, B., *Canadian J. of Physics*, 31, p.15, 1953.
- 3) Tiiler, W. A. and Rutter, J. W., *Canadian J. of Physics*, 34, p.96, 1956.
- 4) Couthard, J. O. and Elliot, R., *J. of the Institute of Metals*, 95, January 1967.
- 5) Vitek, J. M. and David, S. A., Scanning Electron Microscopy, 1, p.169, 1981.
- 6) Katayama, S. and Matsunawa, S. A., *ICALEO*, 44, p. 60, 1984.
- 7) Brody, H. D., and Flemings, M.C. *Trans. AIME*, 236, p. 615, 1966.
- 8) Flemings, M. C. and Nereo, G. E., *Trans. AIME*, 239, p. 1449, 1966.
- 9) Fiemings, M. C. and Mehrabian, R., *Trans. AIME*, 242, p. 41, 1986.
- 10) Khan, P. A. and DebRoy, T., *Met. Trans.*, 15B, p. 641, 1984.
- 11) Khan, P. A. and DebRoy, T., *The Metallurgical Society of AIME*, PA. p. 71, 1985.
- 12) Khan, P. A. , *Ph.D. Thesis* , Penn. State Univ., 1987
- 13) Collur, M. M., and DebRoy, T., *Met. Trans-B*, 1987.
- 14) Robert, E. , Physical Metallurgy Principles , Second Ed., 1973.

- 15) Porter, D. A. and Easterling, K. E., Phase Transformations of Metals and Alloys, 1982.
- 16) Mehrabian, R., Kear, B. H. and Cohen, M. , Rapid Solidification Processing: Principles and Technologies, 1, 1977.
- 17) Idem, Rapid Solidification Processing: Principles and Technologies, 2, 1980.
- 18) Flinn, J. E., Rapid Solidification Technology for Reduced Consumption of Strategic Materials , 1985.
- 19) Vander Sande, J. B. and Kelly, J. F., Met. Trans., A, 1983.
- 20) Vitek, J. M., David, S. A. and Dasgupta, A., Met. Trans., V. 14A, p. 1833, Sep. 1983.
- 21) Minemura, T., Met. Trans., V. 11A, April 1980.
- 22) Ge, Y. L., 1983 Annual Meeting of the Materials Research Society, Nov. 1983, Boston, MA.
- 23) Fredriksson, H. , Met. Trans. V. 3(11), p. 2989, 1972.
- 24) Arata, Y. Matsuda, F. and Katayama, S., Japanese Welding Research Institute Transactions, V. 5(2), p. 35, 1976.
- 25) Suutala, N., Takalo, T. and Moisio, T., Met. Trans. 11A, V. 5, p.717, 1980.
- 26) Suutala, N., Takalo, T. and Moisio, T., Met. Trans. 10A (4), p. 512, 1979.
- 27) David, S., Goodwin, G. and Braski, D., Welding J., 58(11), p.330, 1979.
- 28) Matsuda, F., Katayama, S. and Arata, Y., Japanese Weld. Res. Inst. Trans., 5(2), p. 35, 1976.

- 29) Brooks, J., Williams, J. and Thompson, A., Trends in Welding Research in US, p. 331, 1982.
- 30) David, S., Weld. Res. Supp., p. 63-s, April 1981.
- 31) Moio, T., Takalo, T. and Suutala, N., Weld. J. Supp., V. 60, p. 92-s, May 1981.
- 32) Takalo, T., Suutala, N. and Moio, T., Met. Trans., V. 10 A, p. 512, April 1987.
- 33) Lippold, J., and Savage, W., Weld. J., 59(2), p.48-s, 1980.
- 34) Ibid, Reference 33, Weld. J., 58(12), p. 362-s, 1979.
- 35) Katayama, S. and Matsunawa, A., Proc. ICALEO, V.44, p.60, 1984.
- 36) Idem, Reference 35, Trans. of J. W. S., V.13, p.115,1982.
- 37) Vitek, J., Dadgupta, A., and David, S., Met. Trans., V. 14A, p.1833, 1983.
- 38) Vitek, J., and David, S., Trends in Welding Research in the US, p. 243, 1982.
- 39) Lippold, J., and Savage, W., Welding J., 59(12), p. 362-s, 1980.
- 40) Purdy, G., Weatherly, G., and Singh, J., Met. Trans., V.16A, p. 1363, Aug. 1985.
- 41) Alberry, P., and Haworth, C., Metal Science, V. 8, p. 407, 1974.
- 42) Savage, W., and Ritter, A., Met. Trans., V. 17A, p. 727, April 1980.
- 43) Ciesiak, M., Savage, W., and Ritter, A., Weld. Res. Supp., p. 1-s, January 1982.
- 44) Thompson, A., Williams, J., and Brooks, J., Weld. Res. Supp., p. 72-s, March 1984.

- 45) Savage, W., and Cieslak, M., Weld. Res. Supp., p. 136-s, May 1980.
- 46) Lippold, J., Weld. Res. Supp., p. 128-s, May 1985.
- 47) Schurmann, E., and Brauchmann, I., Erchive for Das Eisenhüttenwesen, V. 48, p. 3, 1979.
- 48) Nakogawa, H., Uehara, T. and Matuda, F., Japanese Weld. Res. inst. Trans., V. 8(1), p. 105, 1979.
- 49) Gill, T., Vijayalakshmi, M., Gnanmoorthy, J. and Padamanabhan, K., Weld. Res. Supp., p. 122-s, May 1986.
- 50) Idem, Reference 38, Weld. Res. Supp., p. 106-s, April 1986.
- 51) Barcik, J., Met. Trans., V. 14A, p. 635, April 1983.
- 52) ASM, Source Book on Stainless Steels, American Society for Metals, 1986.
- 53) Brower, W., E, Strachan, R, and Flemings, M., C., AFS Cast Metals Research Journal, p. 176, Dec. 1970.
- 54) Paul, A., "Role of Transport Processes During Laser Welding", Ph.D. Thesis, The Pennsylvania State University, 1987.
- 55) Lancaster, J., F., Metallurgy of Welding, Third Edition, 1980.
- 56) David, S., Dasgupta, A., and Vitek, J., M., Ibid, Reference 20.
- 57) DebRoy, T., Khan, P., and David, S., Weld. J. Res. Supp., January 1988.
- 58) Perkins, R., Padgett, R, and Tunali, N, Met. Trans., V 4, November 1973
- 59) Hirano, K, Cohen, M. , and Averbach, B. L., Acta Metal, V.9, May 1961.

- 60) Lippold, J., *Ibid*, Reference 46.
- 61) Arata, Y., *Ibid*, Reference 24.
- 62) Suutala, N., *Met. Trans.*, V. 13A, Dec. 1982.
- 63) Guiraldeng, P., Solid-solid Phase Transformations, ASM.
- 64) Kelly, T., Cohen, M., and Vander Sande, J., *Met. Trans.*, V. 15A, May 1987.
- 65) Flemings, M., Chu, M., Shiohara, Y., and MacIsaac, D., Grain Refinement in Castings and Welds, Edited by S. A. David and G. J. Abbaschian, 1983.

VITA

Saleh A. Abdulgader was born on March 16, 1952, of Libyan nationality. After completion of his higher school education from Missurata high school, he entered El-fatih University, Tripoli, Libya, from where in 1977 he received a Bachelor of Engineering degree in Metallurgical Engineering. From 1977 to 1978 he served as a graduate assistant in Metallurgical department at El-Fatih University.

In 1980 he joined the Metallurgy department of Colorado School of Mines to pursue graduate studies in Metallurgy, leading to a Master of Engineering degree in Metallurgy. He finished his M.S. in 1983; after that he joined the Metallurgy department of Pennsylvania State University to earn a Doctorate of Philosophy degree in Metals Science and Engineering. After his Ph.D, he will join the Metallurgy department at El-Fatih University as assistant professor.

He is married and has two boys. He is a member of American Welding Society and American Society for Metals.